Light Readout for a 1 ton Liquid Argon Dark Matter Detector

Dissertation

zur

Erlangung der naturwissenschaftlichen Doktorwürde (Dr. sc. nat.)

vorgelegt der

Mathematisch-naturwissenschaftlichen Fakultät

der

Universität Zürich

von

Boccone Vittorio

aus Italien

Promotionskomitee

Prof. Dr. Claude Amsler (Vorsitz)
Prof. Dr. Laura Baudis
Dr. Polina Otyugova
Dr. Christian Regenfus

Zürich, 2010

Contents

Zusammenfassung

Evidenz für die Existenz dunkler Materie (DM) wird von verschiedensten astronomischen Beobachtungen berichtet, wie zum Beispiel der des *Bullet Cluster's* (Ref. 1). Ein populärer Kandidat dafür sind schwach wechselwirkende massive Teilchen (WIMPs), speziell das Neutralino, das leichteste einer möglichen Erweiterung des Standardmodells mit supersymmetrischen Zuständen (MSSM).

Eine erhebliche Zahl von Forschungsgruppen in der Welt arbeitet an einem direkten Nachweis von dunkler Materie im Labor, der möglichen Streuung von einem WIMP an einem Atomkern. Ein Detektor dafür sollte eine grosse Masse und ein exzellentes Hintergrund-Unterdrückungsvermögen haben, wegen des sehr kleinen Wechselwirkungsquerschnitts eines solchen Prozesses ($\sigma_{WIMP-Kern} < 4 \cdot 10^{-8}\,\mathrm{pb}$). Momentan werden kondensierte Edelgase als eine der erfolgversprechendsten Materialien für grosse DM-Detektoren betrachtet, da sie kleine Anregungsenergien und grosse Isotopenreinheit besitzen und vor allem leicht in der Grösse hochskaliert werden können. Als gute Szintillatoren mit gleichzeitig langen Lebenszeiten für freie Elektronen werden sie als aktive Target-Materalien für einen direkten Nachweis von dunkler Materie benutzt.

Diese Doktorarbeit beschäftigt sich mit der Entwicklung eines grossen (1 Tonne) Flüssigargon-WIMP- Detektors (ArDM), der gleichzeitig Ladung und Licht, erzeugt durch Ionisation und Szintillation des flüssigen Argons, misst. Das vakuum-ultraviolette (VUV) Szintillationslicht des Argons muss mit wellenlängenschiebenden (WLS) Materialien, wie hier Tetra-Phenyl-Butadiene (TPB), umgewandelt werden, um es in Photovervielfachern mit Bialkaliphotokathoden messen zu können. Diese Doktorarbeit beschreibt Entwicklung und Aufbau eines effizienten VUV Detektorsystems mit niedriger Energieschwelle für einen grossen Flüssigargon Detektor.

Das Szintillationslicht von α-Teilchen in gasförmigen (GAr) und flüssigem Argon (LAr) wurde zur Entwicklung von WLS beschichteten Reflektoren benutzt. Verschiedene Aufdampfungstechniken wurden untersucht und optimiert. Die besten Resultate wurden für eine Bedampfung einer Teflonmembran (Tetratex) als Reflektormaterial mit einer WLS Oberflächendichte von 1 mg/cm^2 (TPB) erzielt. Das LAr Szintillationslicht wurde für verschiedene ionisierende Teilchen untersucht. Die relativen Intensitäten der Szintillationskomponenten wurden mit α-Teilchen, Elektronen und Muonen gemessen. Weiterhin wurden neutroneninduzierte Argon Kernrückstösse beobachtet. Eine grosse Aufdampfanlage wurde zur Beschichtung von grossen Oberflächen mit dem WLS konstruiert. Diese Entwicklungen waren vorbereitend für die Konstruktion der ArDM Lichtauslese, die hauptsächlich aus zwei Teilen besteht: dem seitlichen Reflektor und der Lichtauslese. Der seitliche Reflektor ist in einzelne Panele aufgeteilt, die mit der grossen Aufdampfanlage hergestellt wurden. Der Lichtdetektor besteht aus einer Matrix von 14×8" kryogenen Photonenvervielfachern (PMTs). Verschiedene kryogene PMTs wurden im Labor getestet. Ein Lichtauslesesystem mit seitlichem Reflektor und 8 PMT Modulen, mit verschiedenen Beschichtungen auf dem Eintrittsfenster, wurde Ende 2007 am CERN zusammengesetzt.

Ein Datenerfassungssystem (DAQ) wurde entwickelt und getestet. Die Güte der Lichtauslese wurde für GAr und LAr gemessen, dazu benutzte man eine bewegliche interne Am α-Quelle und eine externe radioaktive Gamma-Quelle in verschiedenen Konfigurationen. Eine Lichtempfindlichkeit von 0.50 ± 0.05 p.e./keV$_{ee}$ (Photoelektronen pro keV Elektronenäquivalent) wurde für 7 von 14 PMTs erreicht. Die Hamamatsu R5912-02MOD PMT wurde zur Konstruktion des 1 Tonnen LAr Detektors ausgewählt, dieser wurde Oktober 2008 zusammengesetzt und getestet.

Abstract

Evidence for dark matter (DM) has been reported using astronomical observations in systems such as the *Bullet cluster* (Ref. [1]). Weakly interactive massive particles (WIMPs), in particular the lightest neutralino, are the most popular DM candidates within the Minimal Supersymmetric Standard Model (MSSM).

Many groups in the world are focussing their attention on the direct detection of DM in the laboratory. The detectors should have large target masses and excellent noise rejection capabilities because of the small cross section between DM and ordinary matter ($\sigma_{WIMP-nucleon} < 4 \cdot 10^{-8}$ pb). Noble liquids are today considered to be one of the best options for large-size DM experiments, as they have a relatively low ionization energy, good scintillation properties and long electron lifetime. Moreover noble liquid detectors are easily scalable to large masses.

This thesis deals with the development of a large (1 ton) LAr WIMP detector (ArDM) which could measure simultaneously light and charge from the scintillation and the ionization of liquid argon. Argon vacuum ultra violet (VUV) scintillation light has to be converted with wavelength shifter (WLS) materials such as TetraPhenyl Butadiene (TPB) in order to be detected by photomultipliers with bialkali photocathodes. This thesis describes the research and developments performed to detect the 128 nm VUV light with high efficiency and low threshold.

The scintillation light from $\alpha-$particles in gaseous (GAr) and liquid argon (LAr) was used for the development of an optimal WLS coated reflector. Different coating techniques were investigated and optimized. The best results were achieved using the evaporation technique, a teflon membrane (Tetratex) as reflector material, and a WLS surface density of 1 mg/cm^2 (TPB). The LAr scintillation light was studied for different projectiles. The relative intensities of the scintillation components were measured for $\alpha-$particles, electrons and muons. Neutron induced argon nuclear recoils were also measured. An evaporator chamber was constructed for the evaporation of the WLS on large surfaces.

This research and development was preparatory for the construction of the ArDM light readout which is composed mainly of two parts: the side reflector and the light detector. The side reflector was segmented in panels which were coated using the large evaporator. The light detector is composed of an array of 14 $\times$ 8" cryogenic photomultipliers (PMTs). Different cryogenic PMTs were tested in the laboratory. A light readout system with the side reflector and 8 PMT modules with different coatings on the photocathodes, was assembled at CERN at the end of 2007.

The data acquisition (DAQ) system was developed and tested. The performances of the light readout were measured in GAr and LAr using a movable internal Am $\alpha-$source and external radioactive sources in different configurations. A light yield of 0.50 ± 0.05 p.e./keV$_{ee}$ (photoelectrons per keV electron-equivalent) was obtained for 7 out 14 PMTs. The Hamamatsu R5912-02 mod PMT was chosen for the construction of the 1 ton LAr detector which was assembled and tested in October 2009.

Chapter 1

Search for dark matter

In this chapter I briefly introduce the status of the dark matter searches and present the possible explanation in the framework of the Minimum Supersymmetric Standard Model (MSSM). The dark matter (DM) candidates are reviewed, as well as the detection techniques used by the experimentalist to detect the DM.

1.1 Astrophysical evidence

The first evidence of missing visible mass in the universe was discovered by the Swiss astronomer Fritz Zwicky in 1933 who applied the virial theorem to the Coma cluster obtaining a total mass which was bigger than what was expected from the observable luminosity. This was confirmed 40 years later when Vera Rubin performed more precise measurements of the velocity curve of spiral galaxies.

As can be seen from the example of galaxy rotation curve in Fig. 1.1 (NGC 6503, Ref. [2]) the ordinary matter disk and gas are not sufficient to explain alone the total rotation speed and justify the presence of a *dark* halo.

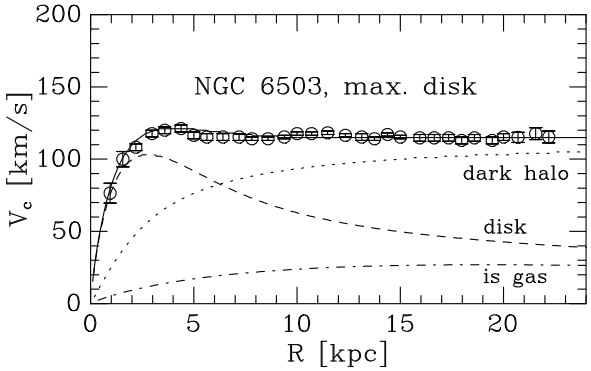

Figure 1.1: Rotation speed vs. radius for the NGC 6503 galaxy rotation curve (Ref. [2]). The *Dark Matter* halo contribution is needed to explain the observed rotation speed.

An alternative solution to the galaxy rotation problem, which does not invoke the presence of an unknown form of matter, is given by the modified newtonian dynamic theory (MOND, Ref. [3]) and relies on the alteration of the gravitational force laws on the galactic scale.

A confirmation to the existence of DM can come from direct detection or from the discovery of a system in which the visible and invisible matter are position dislocated as in the case of the observation of the *Bullet Cluster* (1E 0657-56) which is composed of two colliding galaxy clusters. The total mass distribution of the two clusters was reconstructed by weak lensing effects and the contours are shown in Fig. 1.2 (left) while the distribution of the gas was obtained by measuring the plasma in the X-ray emission. When the two distributions are overlapped Fig. 1.2 (right) it becomes clear how the center of the mass distribution is shifted from the center of the plasmas. This observation can be explained by a non visible massive halo of DM as the mass of plasma should be much larger than the visible mass.

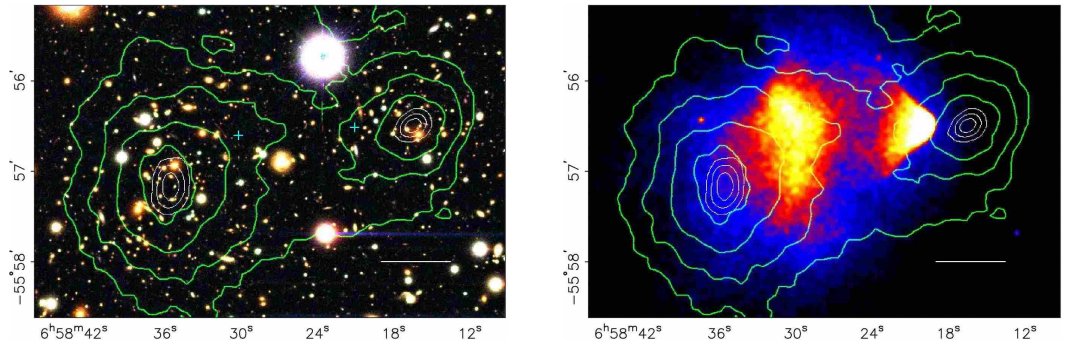

Figure 1.2: Left: Image of the Bullet Cluster, in green the weak lensing κ reconstruction contours of the mass distribution. **Right:** Reconstructed mass distribution contours overlapping with the plasma distribution from X-ray observations (Ref. [1]).

The Universe is mainly composed of dark energy (75%) [4]. DM represents 21% of the mass of the Universe while only 4% is composed by baryons.

1.2 Candidates for dark matter

The nature of DM is, for the moment, still a mystery. Dark matter particle particles must be electrically neutral, stable and weakly interacting, else they would have disappeared by interaction or decay since the birth of the universe. A review of potential DM candidates as a function of mass and cross section with nucleons is shown in Fig. 1.3.

The neutrino (red) was considered until recently an optimal candidate as *we know it exists*. However, neutrinos are too light and their predicted relic density is not sufficient to reach the critical density ($\Omega = 1$) as cosmic microwave background measurement (CMB) bound $\Omega_\nu h^2 \leq 0.0067$ (Ref. [6]).

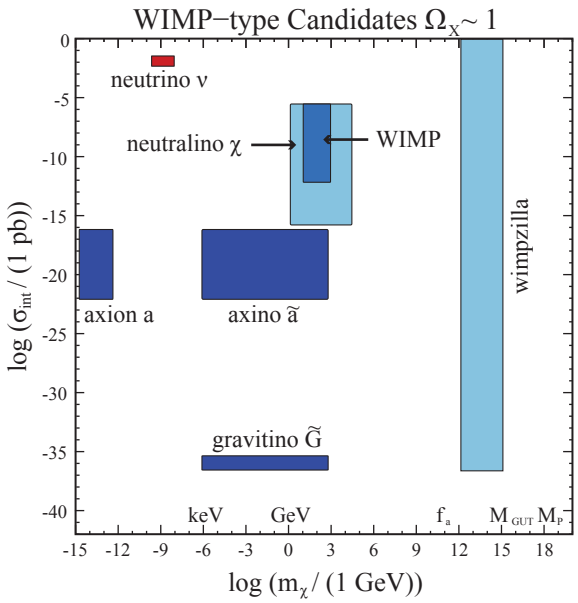

Figure 1.3: Cross section of different potential DM candidates with nucleons (Ref. [5]) as a function of mass. The predicted regions for different MSSM candidates which provide cold dark matter (CDM) candidates (blue) are shown in contrast to the SM neutrino (red), which is a hot dark matter candidate. The neutrino is the only candidate so far experimentally known.

Axions (a), which are introduced as an extension of the SM, are considered as possible DM candidates because they are weakly interacting with ordinary matter. However they must be very light and the calculation of their relic density is based on many assumptions on the production mechanism.

Supersymmetry (SUSY) offers different candidates:

- The neutralino $\tilde{\chi}_1^0$ (or simply χ) is a particle predicted by the minimum supersymmetric extension of standard model (MSSM) and is the lighest of the four QM mixing states of the Higgsinos ($\tilde{H}_1^0$, $\tilde{H}_2^0$) and gauginos ($\tilde{B}$, $\tilde{\gamma}$).
- The gravitino $\tilde{G}$ is the supersymmetric partner of the graviton;
- The axino ($\tilde{a}$) is the supersymmetric partner of the axion.

Weakly interactive massive particles (WIMPs) represent a particular group of DM candidates with a cross-section $10^{-16} < \sigma < 10^{-6}$ pb and a mass $1 < m_X < 10^4$ GeV and include candidates from the χ and the lightest Kaluza-Klein (KK) particle $B^{(1)}$ which is an excitation of the hypercharge gauge boson. WIMPs mass lower than 47 GeV were excluded by LEP (Ref. [4]). The *Wimpzilla* scenario predicts DM candidates to have a mass many orders of magnitude larger than the weak scale.

Among the different possibilities WIMPs and in particular the lightest neutralino χ are the most popular DM candidates as they have the natural properties of being massive, neutral, weakly interacting and stable.

1.3 Indirect searches

The techniques for indirect detection of DM are based on the detection of the radiation produced by the annihilation of DM. The flux of radiation is proportional to the rate and to the square of the DM density, therefore experiments aiming to detect DM signals look at dense regions of the universe such as the galactic center, dwarf galaxies and - closer to us - the sun.

In the case of the neutralino χ the most important diagram is annihilation into fermions (Ref. [6]) as shown by the Feynman diagrams in Fig. 1.4 where A is the pseudoscalar Higgs boson. Clear signals are expected from higher order diagrams such as $\chi\chi \to \gamma\gamma$ and $\chi\chi \to \gamma Z$.

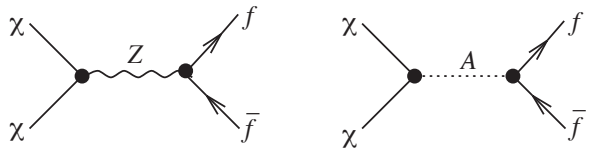

Figure 1.4: Examples of χ annihilation diagrams into two fermions.

Indirect DM searches has been performed by:

- EGRET [7] and FERMI [8], two general purpose γ-ray space telescopes which can detect $\gamma-$rays from 30 MeV to 30 GeV (EGRET) and 30 MeV to 300 GeV (FERMI);
- MAGIC [9] and HESS [10], two general purpose imaging atmospheric Čerenkov telescope arrays installed in *La Palma* island and *Namibia* respectively. MAGIC has a lower trigger threshold of about 50 GeV while HESS is sensitive from 100 GeV;
- PAMELA [11], a space mission dedicated to DM experiments, which includes detectors for particle identification. DM annihilation would result in an observed anomalous antiproton flux at energies above 10 GeV and an excess of positrons;
- ANTARES [12] and IceCube [13], neutrino telescopes which use sea water and ice, respectively, as detection media. DM could accumulate at the center of the earth or the sun producing an enhanced neutrino flux from its annihilation.

The sky surveys observed a slight excess of positrons but unfortunately no excess of antiprotons (Ref. [7, 14]) in particular PAMELA (Ref. [15]).

1.4 Direct searches

Direct DM searches are based on the assumption that the earth is flying through a DM halo stationary in the galactic reference frame at a relative speed of about 230 km/s (Ref. [16]). The earth is rotating in the solar system therefore the apparent speed of the DM flux would be modulated by $\pm$15 km/s.

As DM is neutral only the secondary products of the interaction can be detected (i.e. recoiling nuclei). The response depends on the physical properties of the detecting media. For these velocities DM collision with ordinary matter are in the regime of elastic scattering. For WIMPs masses in the range 10 GeV to 10 TeV the typical nuclear recoil energies are of order of 1 to 100 keV (Ref. [4]). Inelastic scattering would leave the target nuclei in an excited nuclear state.

Energy can be transferred to phonons (heat) in lattices and crystalline structures, or can produce free electrons in material with a low ionization potential and excite molecular levels of organic materials (or simple molecules) which decay producing light (scintillation).

Depending on the detecting material one or more of these quantities can be measured at the same time. Materials like Ge and Si have natural crystalline structure, therefore they are good candidates for the construction of bolometers. At the same time they have very low ionization potential and good charge drifting properties. Noble liquids such as argon or xenon are nowadays two of the best options for large-size dark matter experiments as the intrinsic purity of the detecting media allows the measurement of the scintillation light and the ionization charges. An overview of these methods is shown in Fig. 1.5.

Briefly some of the DM searches that cover all the different detection techniques are:

- **Ionization**: Drift-II [17], is a time projection chamber (TPC) where 167 g of CS_2 are used as an active target for directional DM search.
- **Ionization and heat**: CDMS [18] and Edelweiss-II [19], two experiments which simultaneously detect heat and ionization. CDMS has Ge and Si detectors while Edelweiss-II uses only Ge;
- **Heat**: CUORE [20] (Cryogenic Underground Observatory for Rare Events) uses a pure bolometric approach with its $\sim$ 1000 $\times$ 1 kg TeO_2 crystals which are cooled down to 10 mK and are able to resolve energies of the order of 0.02 eV;

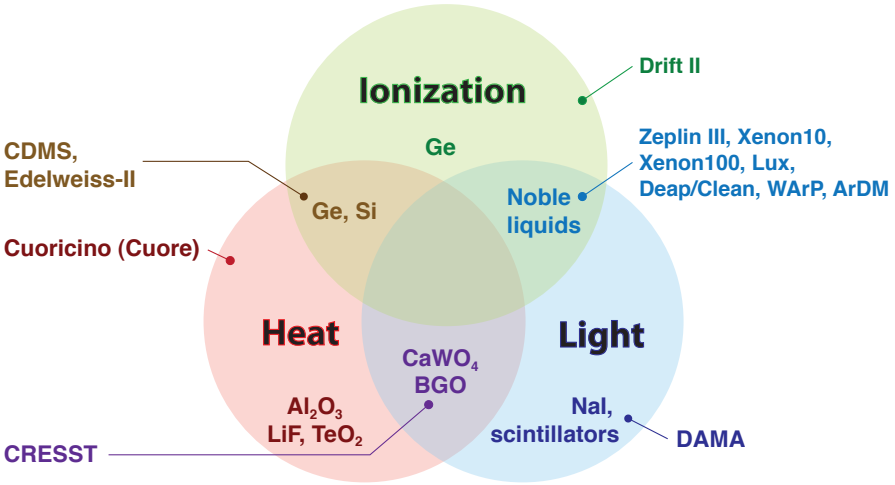

Figure 1.5: Different techniques for direct DM searches.

- **Heat and light**: CRESST [21], uses $CaWO_4$ crystals which have good scintillation properties (light sensitive bolometers);
- **Light**: DAMA/LIBRA [22] measures the scintillation light from pure NaI(Tl) crystals;
- **Light and ionization**: charges and light can be measured using gas (or condensed gases). Xenon was used by the Zeplin-III [23] and XENON10 [24] (and the follow-up XENON100 [25]) experiments while argon has been chosen from the ArDM [26], WArP [27] and DEAP/CLEAN [28] experiments.

1.5 Present experimental limits

Direct DM searches have placed in the last years very strong limits on spin-dependent and independent scattering cross sections. The DAMA experiment claimed an annual modulation of the event rate (Ref. [22]) but the allowed region of cross section and mass were soon excluded by other experiments as CMDS and EDELWEISS, which explored the parameter space measured by DAMA without finding any evidence of DM (Ref. [18, 19]). Possible effects of channeling on the cross section in crystals (Ref. [29]) were later considered and taken into account in the (re)analysis of new DAMA data (Ref. [30]). The new parameter space is not yet completely excluded by the experiments with the - present - best sensitivity (CDMS and XENON10). CDMS has reported the detection of 2 events in the nuclear recoil region while expecting $0.8 \pm 0.2(\text{stat}) \pm 0.1(\text{sys})$ from background (Ref. [31]), but the signal was not sufficient to claim a discovery nor to reject the signal. Recently the XENON100 experiment reported the results of 11.17 live days of non-blind data (Ref. [25]) where no events were observed. The present upper limits of spin independent direct searches as a function of the WIMP mass are shown in Fig. 1.6.

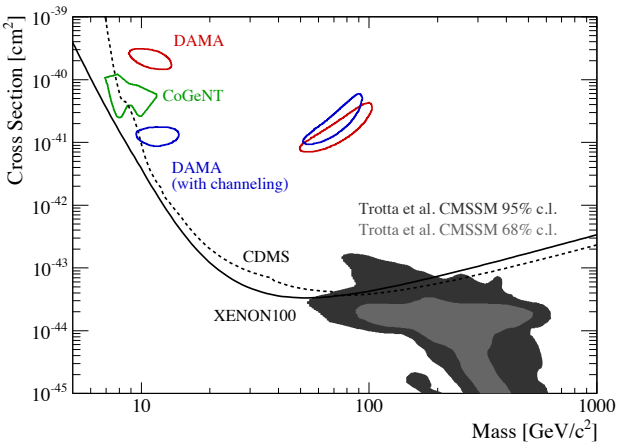

Figure 1.6: Present upper limits of spin independent direct searches (90% C.L., Ref. [25]).

Chapter 2

Scintillation and ionization in gaseous and liquid argon

As shown in Chapter 1 the interaction of DM with ordinary matter is an elusive process because the nuclear-WIMP interaction cross section is small. Moreover the nuclear recoils produced by elastic collision of WIMPs have energies below 100 keV. To overcome those limitations a DM experiment should feature a large target mass, an efficient way to extract the signal and an excellent rejection of radioactive background.

Liquid nobles have high scintillation yields and are also suitable for charge detection because of their relatively low ionization potentials. Both ionization and scintillation can be detected (Ref. [26, 32]). Argon (^{40}Ar) is less expensive than xenon and is therefore competitive for large volumes, in spite of its contamination by the ^{39}Ar $\beta-$emitter isotope, as already pointed out in 1993 by the ICARUS collaboration (Ref. [33]). In addition different ionization and excitation yields for light and heavy projectiles confer an intrinsic capability to reject the electron and the γ background.

In this chapter I review the processes of scintillation and ionization in gaseous and liquid argon. I explain the light and charge quenching effects caused by impurities, electric field, nuclear effects and ionization density of the impinging particle.

2.1 Argon properties

Argon is a noble gas and therefore chemically inert. It has a boiling temperature (T_{boil}) of 87.28 K at atmospheric pressure. Argon is the third most common gas on earth and therefore can be obtained in large quantities by cryogenic fractional distillation of air. The main properties of argon are summarized in Tab. 2.1.

Natural argon is made of 4 isotopes: ^{40}Ar ($> 99.6\%$), ^{36}Ar ($\sim 0.33\%$), ^{38}Ar ($\sim 0.06\%$) and traces of the $\beta-$radioactive isotope ^{39}Ar (Ref. [34]) which is generated by the interaction of cosmic rays with ^{40}Ar (see Section 3.3.1 for more details). Apart from ^{39}Ar, the 3 main isotopes composing the natural argon have spin 0^+, as shown in Tab. 2.2. For this reason argon cannot be used for spin-dependent dark matter searches.

Parameter	Symbol	Value
ionization energy	E_i	15.7596 eV
boiling temp.	T_{boil}	87.28 K
melting temp.	T_{melt}	83.80 K
density LAr	ρ_{LAr}	1.396 g/cm^3
density GAr (NTP)	ρ_{GAr}	1.782 g/ℓ
refractive index (LAr)	n_r	1.22

Table 2.1: Argon properties.

isotope	spin	abundance	comments
^{36}Ar	0^+	0.003336(4)	stable
^{38}Ar	0^+	0.000629(1)	stable
^{39}Ar	$7/2^-$	traces (Ref. [34])	$\beta^- \rightarrow ^{39}$K, $Q =$ 565 keV, 269(4) y
^{40}Ar	0^+	0.996035(4)	stable

Table 2.2: Argon natural isotopes abundance and their decays.

2.2 Scintillation mechanism

The passage of ionizing particles in noble gases or liquids produces ionization and excitation of the atoms. In the case of a generic noble gas X, the excitons (excited atoms) and the ions mainly form the excited molecular states X_2^* and X_2^+ respectively. The X_2^* excimer (excited dimer) decays radiatively:

$$X^* + X \rightarrow X_2^* \rightarrow 2\,X + \gamma_{VUV}, \tag{2.1}$$

while the X_2^+ state eventually recombines with an electron then falling into the X^* excited state:

$$\begin{aligned} X^+ + X \quad &\rightarrow \quad X_2^+ \\ & \quad\; X_2^+ + e^- \rightarrow X^{**} + X \rightarrow X_2^{**} \rightarrow X^* + X + \text{heat}, \end{aligned} \tag{2.2}$$

which decays radiatively. Both processes are strongly pressure and density dependent. Recombination is also sensitive to external electric fields. For gaseous argon at room temperature and normal pressure excitation dominates as shown in Ref. [35, 36]. Recombination luminescence becomes important at high pressures or in the condensed state.

2.2.1 Radiative decays

The lowest radiative allowed decays from the molecular excited states are the transition from the singlet $^1\Sigma_u^+$ state or the triplet $^3\Sigma_u^+$ state to the ground state (Ref. [37, 38]) which results in two independent atoms and the emitted photon at 128 ± 10 nm (Ref. [39]). This emission, which is in the vacuum ultra violet (VUV) region of the spectrum, is often called *second continuum*.

The existence of other radiative decays at higher wavelengths ($\lambda > 170$ nm) [40] has been associated by Langhoff (Ref. [41]) to the decay of the double ionized dimer to two single ionized atoms ($Ar_2^{2+} \rightarrow Ar^+Ar^+$). This emission was observed in gaseous argon (Ref. [42]) and is known as *third continuum*.

In liquid only the two lower excited molecular levels are considered responsible for the VUV light production: $^1\Sigma_u^+$ (singlet) and $^3\Sigma_u^+$ (triplet) states with two characteristic decay times τ_1 and τ_2. The singlet state decay is strongly allowed and has a fast decay time ($\tau_1 \sim$ ns) while the triplet state decay is due to strong spin-orbit couplings in Ar_2 and has a longer decay time ($\tau_2 \sim \mu$s). Reabsorption cannot occur because the energies of the lowest atomic excited states are too high. Only high level impurities such as water, N_2 and CO_2 can reabsorb VUV light and in addition quench the radiative decay of the triplet excimer state (see Section 2.3).

The decay time of the triplet state depends on purity. For this reason the results depend on the cleanness of argon and the contamination of the measurement setup. For gas at NTP with an air contamination level lower than 10 ppb $\tau_2 = 3.140 \pm 0.067$ μs (this thesis and Ref. [43]) and for liquid 1.6 ± 0.1 μs (Ref. [44]). The most important measurements of τ_2 in GAr and LAr are shown in Tab. 2.3 and Tab. 2.4.

The populations of the singlet (Σ_s) and triplet (Σ_t) states depend on the different ionization density properties in LAr. The ratio between Σ_s and Σ_t has been measured for $\alpha-$particle, e^- from $\beta-$decays, $\gamma-$rays and fission fragments (FF). As shown in Tab. 2.4 the singlet state is dominant for heavy projectiles such as $\alpha-$particle and FF, while the situation is inverted for light projectiles. This *feature* of the argon scintillation light is very

measurement	τ_2 [μs]
Keto *et al.* [45]	3.2 ± 0.3
Millet *et al.* [46]	2.86
Oka *et al.* [47]	2.83 ± 0.08
Amsler *et al.* [43] (this thesis)	3.140 ± 0.067

Table 2.3: Decay time of the slow component of GAr.

particle	τ_1 [ns]	τ_2 [μs]	Σ_s/Σ_t	Reference
e^-	4.6	1.54	0.26	[35]
e^-	7.0 ± 1.0	1.6 ± 0.1	0.3	[44]
γ	4.9 ± 0.2	1.26 ± 0.03	0.25	[48]
α	4.4	1.1	3.3	[35]
α	7.1 ± 1.0	1.66 ± 0.10	1.3	[44]
fission fragments	6.8 ± 1.0	1.55 ± 0.10	3	[44]

Table 2.4: Decay time of the fast and slow component of LAr and ratio of singlet (Σ_s) to triplet (Σ_t) light.

important for particle type discrimination and background rejection (see Section 2.4).

Evidence for an *intermediate* state with a decay time of $\tau_{\text{int}} \simeq 100$ ns has been reported in Ref. [44, 48] and has been also investigated in this thesis (see Chapter 4 and following).

2.2.2 Energy per e-ion pair and scintillation photon

The average number of electron-hole pairs N_i produced by the absorption of a determined quantity of energy E in argon is given by:

$$N_i = \frac{E}{W} \qquad \text{where} \qquad W = \begin{cases} 23.6^{+0.5}_{-0.3} \text{ eV} & \text{for LAr (from Ref. [49])} \\ 26.4 \text{ eV} & \text{for GAr (from Ref. [50])} \end{cases} \tag{2.3}$$

where W is the ionization energy. The ratio between N_i and the number of excitons N_{ex} produced in the process has been measured in LAr for different relativistic ions and electrons (Ref. [51, 52]) and is $N_{ex}/N_i = 0.21$. Therefore it is possible to calculate the average energy expended per scintillation photons W_s in LAr as:

$$W_s = W \left(1 + \frac{N_{ex}}{N_i}\right)^{-1} = 19.5 \text{ eV} \qquad \text{(from Ref. [52])}. \tag{2.4}$$

This value is the intrinsic light yield of liquid argon which does not take in account the detection efficiency and the quenching phenomena and correspond to yield of about 50 p.e./keV.

2.3 Luminescence quenching in LAr

Different effects may lead to the quenching of the luminescence in LAr (or other liquid noble gases). The luminescence of low energy nuclear recoils or $\alpha-$particles is significantly reduced compared to electronic recoils as observed in Ref. [44, 53, 54]. A possible explanation of this reduction is that the energy lost by nuclear collision does not participate to the production of scintillation light. This effect is also called *nuclear quenching*.

Lindhard's model alone is unfortunately not sufficient to explain the reduction of scintillation yield for low energy nuclear recoils in xenon and argon (Ref. [27, 55]). Also other processes can lead to a quenching of the luminescence:

- *Bi-excitonic quenching*: Hitachi and Doke (Ref. [56]) proposed a mechanism of quenching based on the process:

$$\text{Ar}^* + \text{Ar}^* \rightarrow \text{Ar} + \text{Ar}^+ + e(\text{kinetic energy}) \tag{2.5}$$

  where two excitons Ar^* are involved in the process before self-trapping in the excited molecular state (excimer) Ar_2^* whose decay gives VUV light. This process (called *bi-excitonic* quenching) becomes important at high ionization densities (i.e. when the excitation density near the interaction trajectory is very high).

- *Collisions between two excimers* to form one excited state and one ground state (Ref. [57], Penning process):

$$\mathrm{Ar}_2^* + \mathrm{Ar}_2^* \rightarrow 2\mathrm{Ar} + \mathrm{Ar}_2^+ + e^-; \tag{2.6}$$

- *Recombination effects*: a non complete recombination of the electron-ion pairs leads to a reduction of the scintillation yield. This happens for example in the presence of an electric field which drift apart the electron-ion pairs;

- *Purity effects*: two body collisions of argon excimers with the impurities can produce a luminescence quenching by the process:

$$\mathrm{Ar}_2^* + \mathrm{X} \rightarrow 2\mathrm{Ar} + \mathrm{X} + \text{kinetic energy}; \tag{2.7}$$

- $^1\Sigma_u^+/^3\Sigma_u^+$ *mixing*: the two molecular states $^1\Sigma_u^+$ and $^3\Sigma_u^+$ can mix with the following reaction:

$$\mathrm{Ar}_2^*(^3\Sigma_u^+) + \mathrm{Ar}(^1\mathrm{S}_0) \rightleftharpoons_k^{k_i} \mathrm{Ar}_2^*(^1\Sigma_u^+) + \mathrm{Ar}(^1\mathrm{S}_0), \tag{2.8}$$

  where the constants k and k_i are poorly measured but preferentially lead to the disappearance of the $^1\Sigma_u^+$ state as described in Ref. [47, 57, 58].

2.3.1 Nuclear quenching

The total energy lost by a projectile, in case of recoiling nuclei, can be expressed in terms of the losses due to the electronic (η) and nuclear (ν) stopping power as proposed by Lindhard (Ref. [59, 60, 61]):

$$E_R = \eta(E_R) + \nu(E_R). \tag{2.9}$$

Only the fraction of energy lost in the electronic excitation (or ionization) f_n contributes to the creation of excitons and electron-hole pairs. For this reason $f_n(E_R)$, which is defined as:

$$f_n(E_R) \equiv \frac{\eta(E_R)}{E_R} = \frac{\eta(E_R)}{\eta(E_R) + \nu(E_R)}, \tag{2.10}$$

represents an ionization energy reduction factor. The total stopping power, represented by:

$$\left(\frac{\mathrm{d}E}{\mathrm{d}x}\right)_{\mathrm{tot}} = \left(\frac{\mathrm{d}E}{\mathrm{d}x}\right)_{\mathrm{elec}} + \left(\frac{\mathrm{d}E}{\mathrm{d}x}\right)_{\mathrm{nucl}}, \tag{2.11}$$

allows to represent f_n as the ratio of the two integrals:

$$f_n(E_R) = \frac{\int_0^{E_R} (\mathrm{d}E/\mathrm{d}x)_{\mathrm{elec}}\, \mathrm{d}E}{\int_0^{E_R} (\mathrm{d}E/\mathrm{d}x)_{\mathrm{tot}}\, \mathrm{d}E}, \tag{2.12}$$

which have to be evaluated for all the possible recoil energies, as the projectile lose energy while traveling in the media. Lindhard approximates f_n with:

$$f_n = \frac{k \cdot g(\varepsilon)}{1 + k \cdot g(\varepsilon)} \qquad \text{with} \qquad k \simeq 0.133\ Z^{2/3} A^{-1/2}, \tag{2.13}$$

where Z and A are the atomic and mass number respectively while $g(\varepsilon)$ is well fitted (Ref. [16]) with:

$$g(\varepsilon) \simeq 3\ \varepsilon^{0.15} + 0.7\ \varepsilon^{0.6} + \varepsilon, \tag{2.14}$$

where $\varepsilon = 11.5\ E_R(\text{keV})\ Z^{-7/3}$. The value of k in Eq. 2.13 is an approximation for projectiles of the same type of the target (i.e. Ar recoils in LAr). The Lindhard quenching factors for nuclear recoils in Ar, Xe and Ne were calculated with Eq. 2.13, and are plotted in Fig. 2.1 as a function of the recoil energy. For other projectile types, such as $\alpha-$particles $f_n(E_R)$ must be calculated with Eq. 2.12.

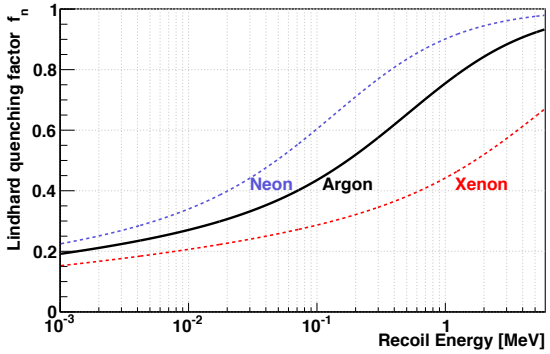

Figure 2.1: Lindhard's quenching factor f_n for Ar (black), Xe (red) and Ne (blue) as a function of the recoil energy calculated with Eq. 2.13 (the Lindhard model).

2.3.2 Luminescence quenching at high ionization densities

Following Hitachi and Doke's approach (Ref. [56]), the ionization tracks can be considered composed of a *core*, which is a zone of relative high energy deposition density along the track of the projectile, and a *penumbra* which is an outer region surrounding the core with a lower ionization density. The bi-excitonic quenching and Penning processes are more likely to occur in the core where the excitons and excimers density is higher.

The relative scintillation response of a scintillator for an ionizing particle is described by Birk's law (Ref. [62]):

$$f_l = \frac{1}{1 + k_B \left(\frac{\mathrm{d}E}{\mathrm{d}x}\right)_{\text{elec}}} \tag{2.15}$$

where k_B is the Birk's coefficient, which represent the overall collision probability in the core of the track, while the electronic energy loss $(\mathrm{d}E/\mathrm{d}x)_{\text{elec}}$ is proportional to the number of excitons and electron-hole pairs as shown in Ref. [49, 63]. The k_B constant can be determined experimentally ($k_B \simeq 7.4 \cdot 10^{-4}$ MeV^{-1} gcm^{-2} for LAr and $k_B \simeq 2.0 \cdot 10^{-4}$ MeV^{-1} gcm^{-2} for LXe (Ref. [64]).

Birk's law, which originally developed for organic scintillators, provides a simple and convenient method to describe the luminescence quenching at high ionization densities without incorporating the details of the single contributions of the different quenching mechanisms.

2.3.3 Comparison of the model predictions with data

The combination of Lindhard's model together with Birk's saturation law was used by Mei *et al.* in Ref. [64] to explain the luminescence quenching in LAr and LXe for nuclear recoils at low energies. The total quenching factor was defined as:

$$q_f = f_n \cdot f_l \ , \tag{2.16}$$

where f_n is the nuclear quenching factor defined in Eq. 2.13 and f_l is the high ionization quenching factor defined in Eq. 2.15. The comparison of the different quenching curves models with data for argon and xenon is shown in Fig. 2.2. The model predicts a quenching factor for nuclear recoils of $q_{n.r.} \simeq 0.27$ for recoiling energy greater than 50 keV.

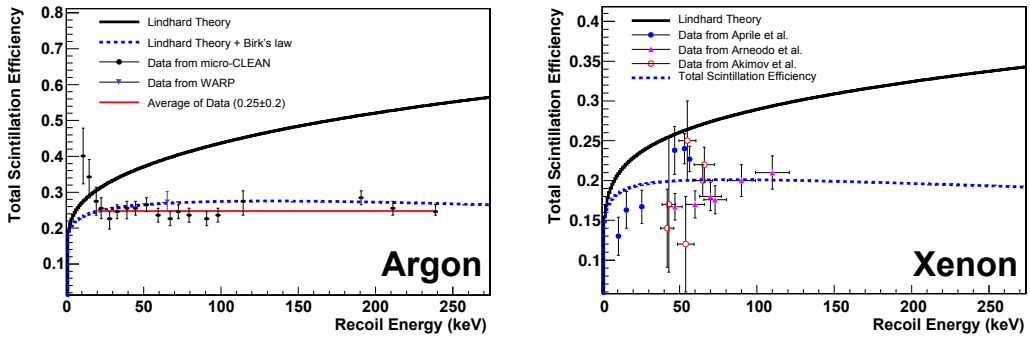

Figure 2.2: Total scintillation efficiencies (blue curves) calculated by Eq. 2.16 for the LAr (left) and LXe (right). The model is compared with the experimental data from different experiments (Ref. [64, 65]). The black curve represent only the Lindhard's nuclear quenching factor f_n.

This approach can be applied also to other particles types such electrons, $\gamma-$rays and $\alpha-$particles. For light projectiles the energy is lost almost completely in electronic collisions. The stopping power $\mathrm{d}E/\mathrm{d}x$ of $\alpha-$particles in LAr is shown in Fig. 2.3 together with electronic and nuclear contributions (obtained with ASTAR [66]). For $\alpha-$particles the nuclear stopping power is very small compared to the total. Therefore the nuclear

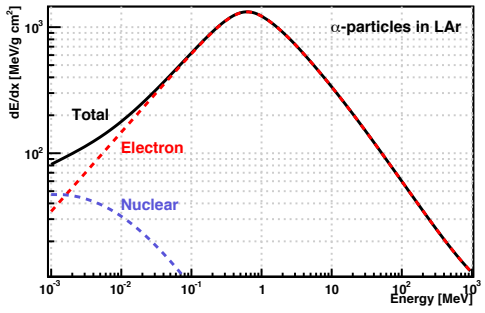

Figure 2.3: Stopping power of $\alpha-$particles in LAr (black) obtained with ASTAR [66]. The contributions of the electronic (red) and nuclear (blue) stopping powers are also shown.

quenching plays only a minor role in the determination of the total quenching coefficient q_f for $\alpha-$particles with energies above 100 keV. In the case of 5.3 MeV $\alpha-$particle $f_n = 0.98$ and $f_l = 0.724$ leading to $q_f = 0.71$. The model agrees with the results ($f_l = 0.72$) obtained by Hitachi in Ref. [56].

The response to electron and γ-rays, which is usually assumed to be linear, might also be affected by significant quenching effects below an electronic recoil energy of 20 keV because of the large stopping power (>10 MeV cm^2/g).

2.3.4 Effect of electric field on scintillation and ionization

The products of ionization can be read-out by applying an electric field drifting the charges (Ref. [67]). In LAr this reduces the effect of recombination and therefore the scintillation light. The intensity of the fields required to collect about 90% of the charge depends on the recombination time and the noble gas. A typical field of 4 - 5 kV/cm is sufficient for LAr. The effect of the charge collection on the quenching of the scintillation light are visible in Fig. 2.4.

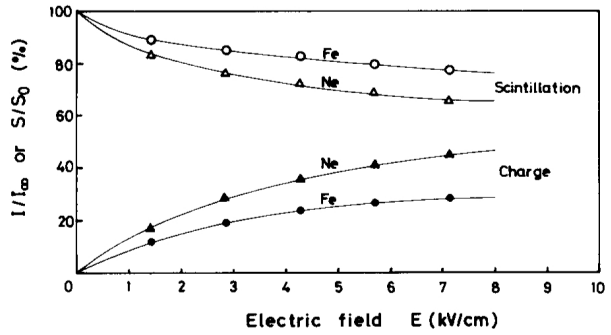

Figure 2.4: Variation of scintillation light and ionization for Ne and Fe ions as a function of the applied electric field (Ref. [67]).

2.3.5 Effects of the impurities

The effects of impurities on the scintillation light and the capture of electrons have been deeply investigated in the last years. The quenching of the triplet excimer state by air traces in GAr was studied in Ref. [43, 68]). This measurement, described in this thesis in Section 4.1, evidences also a linear relation between the measured scintillation light and the decay time of the slow component. In addition it was confirmed that the fast component in GAr has a wavelength $\lambda_{\text{fast}}^{GAr} > 170$ nm, as described in Section 2.2.1, and cannot be interpreted as the decay of the $^1\Sigma_u^+$ state.

Quenching of the scintillation light in LAr by O_2 and N_2 contamination was studied in details in Ref. [69, 70] and the results are are summarized in Ref. [48]. The effect of N_2 contamination on the relative amplitude of the scintillation light and on the decay times of the scintillation components are shown in Fig. 2.5. In LAr, as in GAr, the decay of

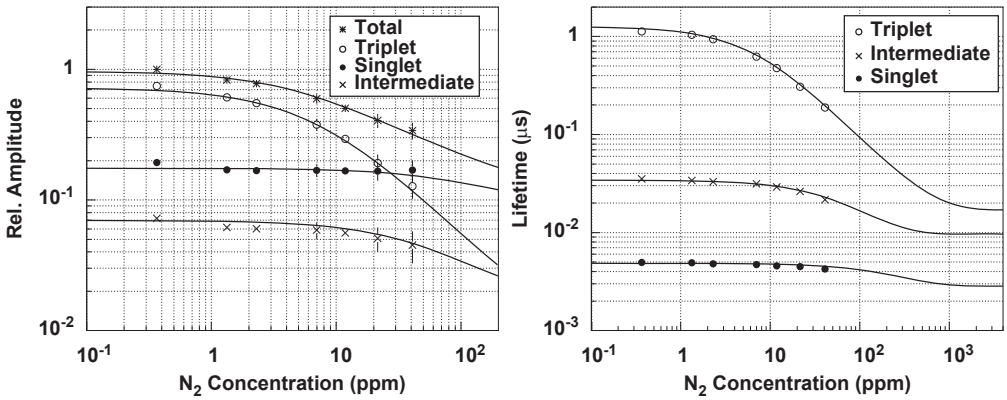

Figure 2.5: Effects of the N_2 contamination in LAr on the relative amplitude of the scintillation light (left) and on the decay time (right) of the singlet, triplet and intermediate components (Ref. [48]).

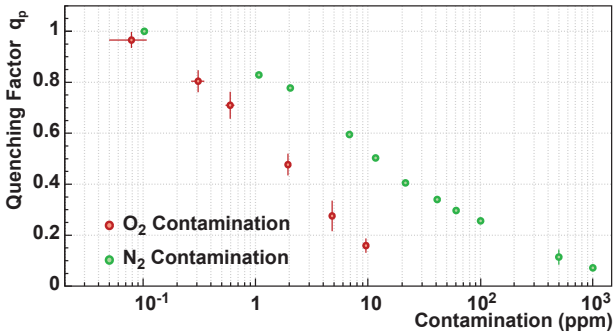

Figure 2.6: Quenching factor q_p as a function of the O_2 (red) and N_2 (green) contamination levels in LAr (Ref. [48]).

the triplet state is strongly affected by the impurity contamination levels. The purity quenching factor of LAr q_p is shown in Fig. 2.6 as a function of the O_2 (red) and N_2 (green) contamination levels.

The contamination levels of LAr (and the contaminants) are often difficult to measure. Therefore it is important to present the purity quenching factor also as a function of a measurable quantities such as the decay times of the scintillation components. The purity quenching factor q_p can be written as the ratio $q_p = L/L_{\max}$ between the measured scintillation light L and the *asymptotic* light $L_{\max}$ (at the maximum purity).

Assuming a linear relation between the light and the decay time, as in GAr (see Section 4.1.4), the *asymptotic* light can represented as the sum of the different components of the measured scintillation light L_i weighted for the ratio between the asymptotic $\tau_i^{\max}$ and the measured τ_i decay times:

$$L_{\max} = L_1 \frac{\tau_1^{\max}}{\tau_1} + L_2 \frac{\tau_2^{\max}}{\tau_2} + L_3 \frac{\tau_3^{\max}}{\tau_3}, \tag{2.17}$$

where $L = L_1 + L_2 + L_3$.

The purity quenching factor q_p assumes then the form:

$$q_p = \frac{L}{L_1 \frac{\tau_1^{\max}}{\tau_1} + L_2 \frac{\tau_2^{\max}}{\tau_2} + L_3 \frac{\tau_3^{\max}}{\tau_3}}. \tag{2.18}$$

2.4 Particle identification in LAr

The ratio between the collected charge and the light output depends on the particle type and for e^-, γ and light projectiles is higher than for nuclear recoils. Neutron and nuclear recoil events produce very intense track cores where the charges are quickly recombined and the ratio charge/light is very small as illustrated in Fig. 2.7.

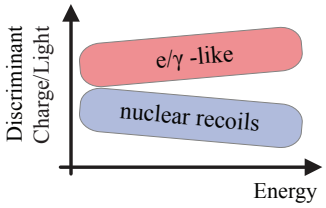

Figure 2.7: Charge to light ratio as a function of energy for the e/γ−like and nuclear recoils.

In LAr the signal produced from electrons is different from the one produced by the nuclear recoils. The ratio between the population of the singlet and triplet state is about 1/3 for light projectiles and 3 for nuclear recoils or alpha particles as described in Section 2.2.1. A sketch of the scintillation time structure for e^-/γ and nuclear recoil-like events is shown in Fig. 2.8 (a) and (b). A discriminant variable F defined as the fraction of prompt (fast) light over the total light can be used to identify the particle species as shown in Fig. 2.8(c).

This method of particle identification is well established (Ref. [71]) and is also called pulse shape discrimination (PSD). PSD techniques will be discussed in details in Section 5.3.

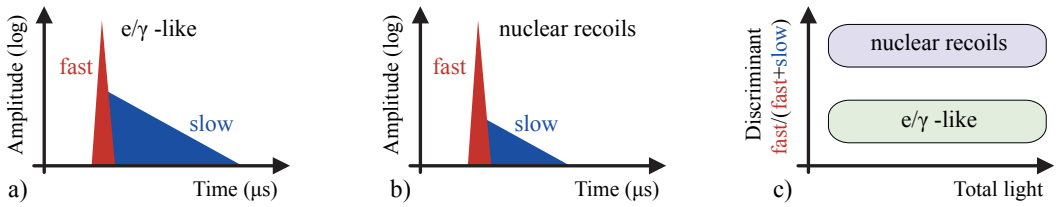

Figure 2.8: Sketch of the scintillation time structure of e^-/γ (a) and nuclear recoil-like (b) events. A discriminator defined as the ratio of the prompt (fast) light over the total light can be used to identify the particle types (c).

Chapter 3

The ArDM experiment

The conceptual layout of the ArDM experiment (Ref. [26]) is shown in Fig. 3.1. WIMPs interact with LAr producing recoiling argon nuclei which are detected by measuring the electrons and the scintillation light as explained in Chapter 2. A 500 kV *Greinacher* multiplication chain (Ref. [72]) provides the electric field necessary to drift the electrons towards the gas phase on the top of the detector. The electrons are extracted from the liquid to the gas phase (E_{extr} ~3 kV/cm) and drifted towards a double stage large electron multiplier (LEM, Ref. [73]) detector where they are multiplied and detected by instrumented anode strips. Position resolution is obtained by the segmentation of the anodes. The detection of the light is performed by an array of 14, 8" diameter, cryogenic photomultipliers (PMTs) placed about 20 cm under the cathode grid.

The goal is to achieve a recoil energy threshold of approximately 30 keV with a combined light and charge analysis. To fulfill this requirements it is necessary to have a very high LAr purity and an excellent background rejection level. A good purity is obtained by

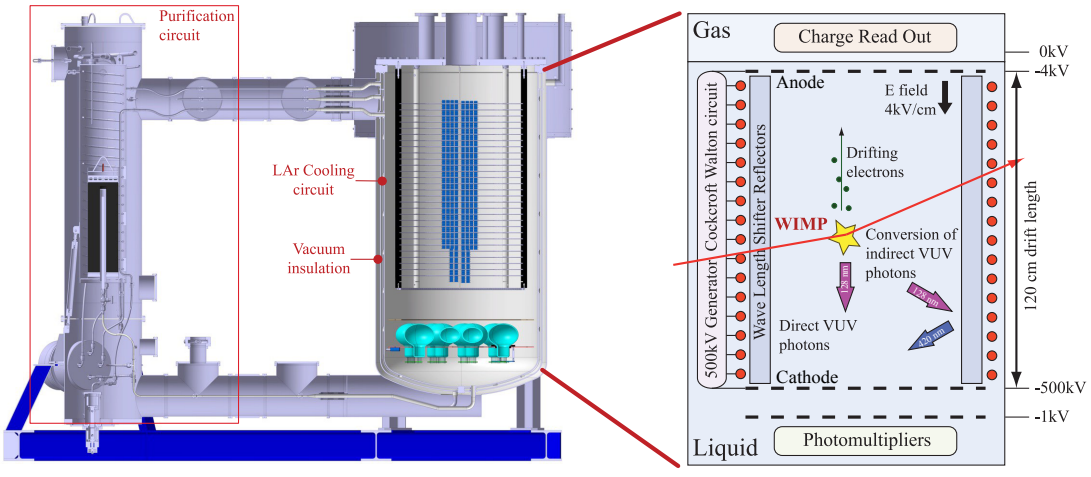

Figure 3.1: Section of the 3D model (left) and conceptual layout (right) of the ArDM experiment.

recirculating the LAr through an active copper filter (purification circuit) by means of a specially developed cryogenic pump. Argon quality is monitored using two independent purity monitoring systems, which measure the electron drift length and the decay time of slow component (τ_2). The main vessel and the purification circuit are surrounded by a vacuum insulation. The detector walls can be pre-cooled with LAr or pressurized LN_2. ArDM benefits from the simultaneous measurement of scintillation light and charge. Three dimensional track reconstruction is obtained by detecting the drifting charges using a time projection chamber method (TPC).

3.1 Charge readout system

The LEM is a large and thicker version of the Gaseous Electron Multiplier (GEM) detector (Ref. [74, 75, 76]). ArDM employs a double stage LEM system composed of two LEM planes and a segmented anode plane. Each LEM plane consists of a 1.5 mm thick dual layer printed circuit board (PCB). The LEM holes have a diameter of 0.5 mm with a pitch of 0.8 mm and are drilled on the PCB by precise machining (standard PCB technology). Holes in the last plane are grouped in strips similarly to the anode plane in order to provide a 2D segmented readout. The third dimension along the detector volume is obtained by measuring the drift time. A granularity of few millimeters grants a sufficient vertex resolution for the rejection of background (e.g. multiple scattered neutrons).

The sub-detector is still in the R&D phase. Stable operations (Ref. [77, 78]) in gaseous argon have been already achieved with a dual stage LEM system, extracting electron from the liquid to gaseous phase with a small 10x10 cm^2 prototype in a dedicated setup (Fig. 3.2).

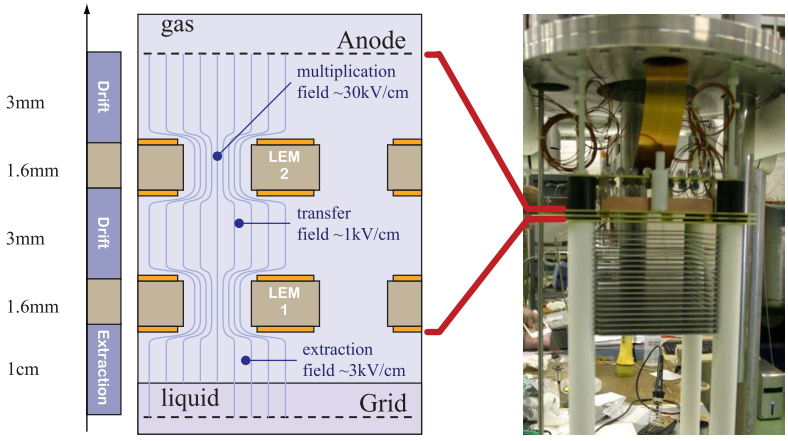

Figure 3.2: Left: Schematic of the 10×10 cm^2 dual-stage large electron multiplier prototype detector. **Right**: Picture of the small R&D dual LEM.

3.2 Light readout system

The light readout system must be able to detect and identify signals in a range from a single to a thousand photons. It is composed mainly of two parts, the reflectors and the light detector, which have been subject of dedicated R&D projects (this thesis and Ref. [43, 79, 80]).

PMTs with MgF_2 windows and CsI (or CsTe) photocathode are detectors able to count photons in the VUV region. However, because of their cost and small dimensions, they are not suitable to cover large surfaces. In addition most of the scintillation light is directed to the side of the detector. Standard PMTs with bialkali photocathode were chosen. The QE peak absorption wavelength for bialkali photocathode is $\lambda_{peak} \approx 420$ nm (at room temperature). For this reason the VUV light must be shifted into longer wavelengths by suitable materials, called Wave Length Shifters (WLS), which were used to coat the side reflectors and the PMT surfaces.

The electrons emitted by the photocathode are not quickly restored at LAr temperature because the bialkali material becomes insulant at cryogenic temperature. A platinum underlay below the photocathode is therefore required to avoid the accumulation of charges.

The Hamamatsu R5912-02 mod Low Background was chosen among few candidates after the preliminary test of the light readout in gaseous and liquid argon (see Chapter 7 and Ref. 8). A low activity glass is desired to reduce the amount of self background. Each PMT is mounted on a 3 mm thick cryogenic PCB base which provides voltage supply, signal extraction and mechanical support. Polyethylene collars positioned on the steel support frame keep the PMTs in the horizontal position at the right distance from the others. The PMTs are shielded from the potential of the cathode (-500 kV) by a grid placed at the same potential as the PMT photocathodes. The assembled light detector, illuminated by UV light (254 nm) is shown in Fig. 3.3.

We selected Tetraphenyl butadiene[1] (TPB) as the best WLS because of its high light conversion efficiency and its diffusive reflection properties. TPB absorbs 128 nm light

[1]IUPAC name: 1,1,4,4-tetraphenyl-1,3-butadiene

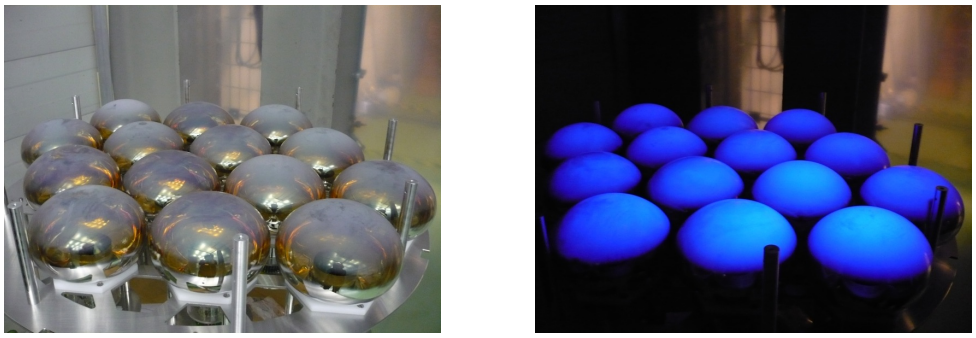

Figure 3.3: Final light detector assembled on the support illuminated by daylight (left) and 254 nm UV light (right).

and reemits at 420 nm (Ref. [81]) which corresponds to the maximum quantum efficiency of bialkali photocathodes. The WLS surface density was optimized on different reflector materials in a small 1 ℓ liquid argon setup in GAr and LAr (Chapter 4 and 5).

The side reflector is segmented into 15 panels (120 $\times$ 25 cm^2) made of 254 μm thick Tetratex[2] membranes mounted on 3M ESR[3] foils which provide mechanical support and shielding from the light coming from the non-active regions near the walls of the detector. TPB was evaporated on each panel with a surface density of 1 mg/cm^2 (Section 4.3 and Ref. [82]).

3.3 Background sources

A dark matter experiment must efficiently reduce the background from natural radioactivity as WIMP interactions are very rare events.

The detector components and the surrounding environment contain radioactive isotopes such as uranium (U) and thorium (Th) in quantities of the order of a part per billion (ppb). The decay chains of those isotopes produce α, β^- and $\gamma-$ray background. Neutrons can be produced by the $\alpha-$capture process (Section 3.3.3) or from spallation in the collision of cosmic rays with atoms. Cosmic rays are also responsible for the production of the unstable long living ^{39}Ar β^- emitter (Section 3.3.1).

ArDM background studies are described in detail in Ref. [83, 84]. The DM event rate in LAr, given a WIMP-nucleon cross section of 10^{-8} pb, is of about 1 WIMP/day ton. At sea level the cosmic muons flux is about 70 m^2 s^{-1} sr^{-1} which corresponds to 10^4 muons/m^2 per minute above 1 GeV (14 M events per day over the ArDM detector). Installing and running the experiment in an underground laboratory provides the necessary shielding for dark matter searches. A depth of 2-3 km water equivalent (km w.e.) provides a reduction of the muon flux of about 5 orders of magnitude, as shown in Fig. 3.4, which should be sufficient to achieve sensitivities of about 10^{-8} pb.

3.3.1 ^{39}Ar background

^{39}Ar is a radioactive isotope which decays to the stable ^{39}K ($T_{1/2}$ = 269 years):

$$^{39}\mathrm{Ar} \rightarrow\ ^{39}\mathrm{K} + e^- + \bar{\nu}_e. \tag{3.1}$$

The spectrum of the emitted electrons has a mean energy of 218 keV and a Q-value of 565 keV. The atmospheric ^{39}Ar is produced by the interaction of cosmic rays with the stable ^{40}Ar isotope. The two main processes are the (n,2n) and (γ,n) reactions:

$$^{40}\mathrm{Ar} + n \rightarrow\ ^{39}\mathrm{Ar} + 2n \qquad \text{and} \qquad ^{40}\mathrm{Ar} + \gamma \rightarrow\ ^{39}\mathrm{Ar} + n, \tag{3.2}$$

which lead at the surface of earth to production rate of 5'000 and 70 isotopes per day per kg, respectively (Ref. [85]). Atmospheric argon contains a small fraction of the ^{39}Ar

[2]High performance ePTFE membrane.
[3]3M Vikuiti^{TM}Enhances Specular Reflection.

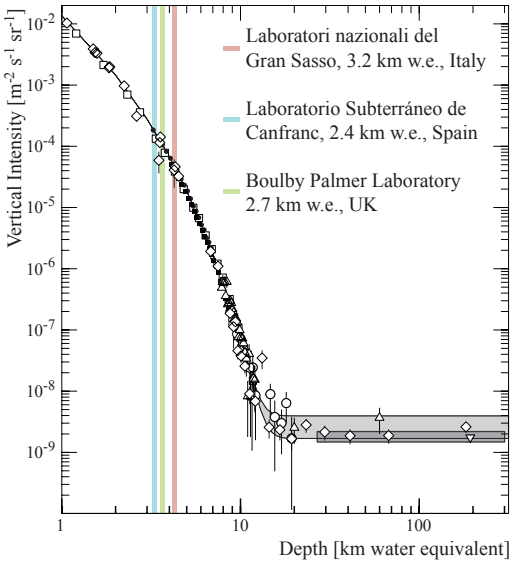

Figure 3.4: Vertical muon intensity vs depth (1km.w.e.= 105 g/cm^{-2} of standard rock) measured for different experiment (from PDG [4]). The experimental data are from: (◊) Crouch, (□) Baksan, (○) LVD, (●) MACRO, (■) Frejus, and (△) SNO, while the shaded area at large depths represents neutrino-induced muons of energy above 2 GeV. The upper line is for horizontal neutrino-induced muons, the lower one for vertically upward muons.

isotope $(7.9 \pm 0.3) \cdot 10^{-16}$ [86]. LAr obtained from the liquefaction of air contains this isotope in a non negligible fraction: the WARP collaboration has recently reported an activity of 1 Bq/kg (Ref. [34]) which makes ^{39}Ar one of the most problematic source of background for liquid argon detectors.

3.3.2 γ background from detector components

The γ background from the detector components, caused by U and Th contamination was investigated in Ref. [83] using the database of natural radioactivity in materials from Ref. [87]. The evaluated U and Th contaminations of the main ArDM detector components are listed in Tab. 3.1 together with the expected $\gamma-$ray rates in ArDM.

Component	Material	U [ppb]	Th [ppb]	Mass [kg]	Rate [γ/s]	% in fid. volume
LEM (low Bkg.)	Vespel polymer (Dupont)	< 2	< 2	4	< 1	39.9
Dewar	Stainless Steel 304L	0.6	0.7	1000	25	8.7
PMTs (×14) (low Bkg.)	metals, glass, bialkali	30	30	10	11	7.5
Pillars/ PMT supports	Polyethylene	20	20	12	10	23

Table 3.1: Contribution to γ background from U and Th contamination of the detector components (Ref. [83]).

The impact of the radioactive contamination of the components on the detector performances depends also on the energy of the $\gamma-$rays and on the position of the contaminated components. The energy spectrum of the $\gamma-$rays from U and Th varies from few tens of keV to about 3 MeV. For photon energies below 100 keV the main contribution to the cross section is represented by the photoelectric absorption while above this value Compton scattering becomes dominant. Pair production in nuclear and electron field start to contribute significantly only above a few MeV.

A Monte-Carlo simulation was performed to study the position of the γ background interactions and their energy deposits. Most of the $\gamma-$rays come from the pillars contamination and are concentrated near the component surfaces. The interaction position in the detector (only Compton scattering and photoelectric effect) for the γ-rays from the dewar and from the pillars are shown in Fig. 3.5.

The total rate of γ background interactions in the active volume is lower than 10 Hz. However only a small fraction of this background leads to an energy deposit in the WIMP range (5 - 100 keV) as it is shown in Tab. 3.2. This background rate is smaller compared to the ^{39}Ar background rate (about 1 kHz).

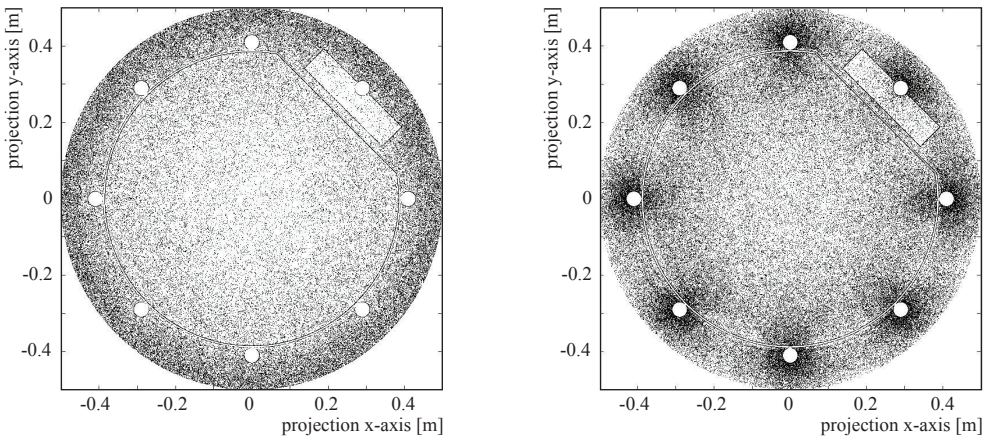

Figure 3.5: Interaction points in the detector volume (top view) for the $\gamma-$rays originating from the dewar (left) and from the pillar (right) (Ref. [83]).

Component	WIMP-like energy deposit	
	Rate [Hz]	% (in fid. volume)
LEM (Vespel low bkg.)	< 0.03	3.9
Dewar	0.28	1.1
PMTs ($\times$14)	0.13	3.1
Pillars/ PMT supports	0.32	1.1

Table 3.2: Rate of events with a WIMP-like energy deposit in the 5 - 100 keV range.

3.3.3 Neutron background

The decay chains of ^{238}U and ^{232}Th contains several α decays with energies between 3 and 11 MeV. Neutrons are emitted following the capture of the $\alpha-$particles by nuclei via the (α,n) and (α,2n) processes with cross sections that depend on the α energy and on the atomic number. Typical capture yields are of the order of 10^{-8} - 10^{-5} per each $\alpha-$decay. The emitted neutrons have energies of few MeVs. Neutrons might also come from spontaneous fission which for Th is negligible while for U the branching ratio is $5.5 \cdot 10^{-5}$ % (Ref. [88]). Each fission produces on average 2 neutrons. The neutron contribution from U spontaneous fission has the same order of magnitude as the $\alpha-$capture processes in the case of the detector components.

The neutron rate originated by radioactive contamination of the detector component was evaluated with a Monte Carlo simulation (Ref. [83]). We expect in total less than 2300 n/year.

3.3.4 Fake WIMP-like events rejection from neutron scattering

Problems might arise from the fact that WIMPs and neutrons lead to similar event topologies since they both produce a recoiling argon nucleus; however the energy spectra and the scattering multiplicities are different (Ref. [83]). More than 56% of the neutrons scatter more than once, as shown in Fig. 3.6, therefore can be rejected. Only 10% of the single-scattered neutrons will then produce a recoiling argon nucleus in the WIMP expected energy range (30-100 keV).

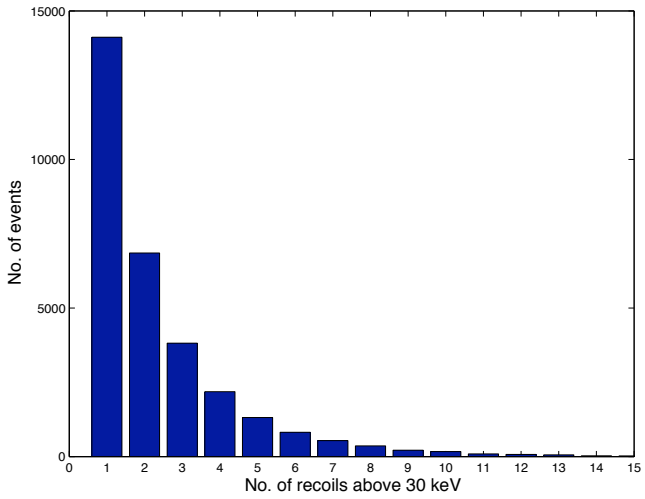

Figure 3.6: Distribution of the number of neutron scatterings in the 1 ton detector (from Ref. [83]). Only neutrons produced in U and Th chains were considered.

Chapter 4

Light collection studies in gaseous argon

The most intense peaks of liquid and gaseous argon emission spectra are in the Vacuum Ultra Violet region (see Chapter 2). As discussed in Section 3.2 we had chosen to employ standard PMTs with bialkali photocathode and to shift the VUV scintillation light into longer wavelengths by wave length shifters (WLS) materials, matching the quantum efficiency peak of the PMT.

WLS are composed of complex molecules (organic chains) which absorb photons of certain specific wavelengths (λ_{abs}) and reemit them at a higher wavelengths (λ_{emis}). The absorption and reemission process is generally very fast ($\simeq$ 100 ps). In our case TetraPhenyl Butadiene (TPB) was chosen as WLS because its emission spectrum overlaps nicely with the LAPMT sensitivity spectrum and its excitation with the emission spectrum of gaseous (and liquid) argon.

The scintillation light from $\alpha-$particles in gaseous argon (GAr) was used as standard VUV light source for the development of an optimal WLS coated reflector. First, the dependence of the scintillation light on impurities was studied (Section 4.1). Different coating techniques were then investigated using the VUV component of the GAr scintillation light. The light yields of different reflectors and WLS configurations were measured and compared (Section 4.2). Then we constructed an evaporator to manufacture the WLS coated reflectors with an uniform and reproducible thickness. The WLS thickness was optimized in GAr using the evaporation technique on two different materials (Section 4.3). These are the subjects covered in the next sections.

4.1 Effects of impurities on gaseous argon.

4.1.1 Experimental setup (Cell '05)

An overview of the Cell '05 experimental setup is shown in Fig. 4.1. The measurements (Ref.[89]) were performed with a Hamamatsu R580 PMT (⌀ 34 mm) with a bialkali photocathode operated at a gain of about 10^6. An acrylic glass light guide was glued on the photocathode, so that the PMT could be left in the gaseous phase for later tests with LAr. In fact standard bialkali photocathodes cannot be operated at liquid argon (LAr) temperature (88 K). At this temperature bialkali layer become insulant and the emitted electrons are not restored leading to a gradual charge accumulation on the photocathode.

The light detector was installed in a 6 ℓ cylindrical stainless steel vessel (internal vessel) with an inner diameter of 15 cm. The side walls of the internal vessel were covered with a Tetratex[1] foil (a fully diffusive light reflector) sprayed with TPB wavelength shifter. The vessel was evacuated down to 10^{-5} mbar using a dry pump followed by turbo molecular pump with a pumping speed of 60 ℓ/s. Baking was not performed. The pumping was stopped at the required air partial pressure (P_{air}) and then filled up to $P = (1100 \pm 10)$ mbar with relatively pure GAr (Ar60[2]). The total concentration of impurities was $\sim$ 1 ppm in total. The levels of the different impurities are shown in Tab. 4.1. In addition the GAr was flown through an *oxisorb*[3] copper-oxide (CuO) filter.

$2O \leq$ 0.5 ppm $H_2 \leq$ 0.1 ppm	$C_nH_m \leq$ 0.1 ppm $N_2 \leq$ 0.3 ppm	$O_2 \leq$ 0.1 ppm	$CO \leq$ 0.1 ppm	$CO_2 \leq$ 0.1 ppm

Table 4.1: Impurity levels for argon gas quality Ar60 from AlphaGaz2 (France).

[1]High performance ePTFE membrane, described later in Chapter 4.2.1.
[2]Argon class 60, AlphaGaz2 (France)
[3]Sorbal 250, AlphaGaz2 (France)

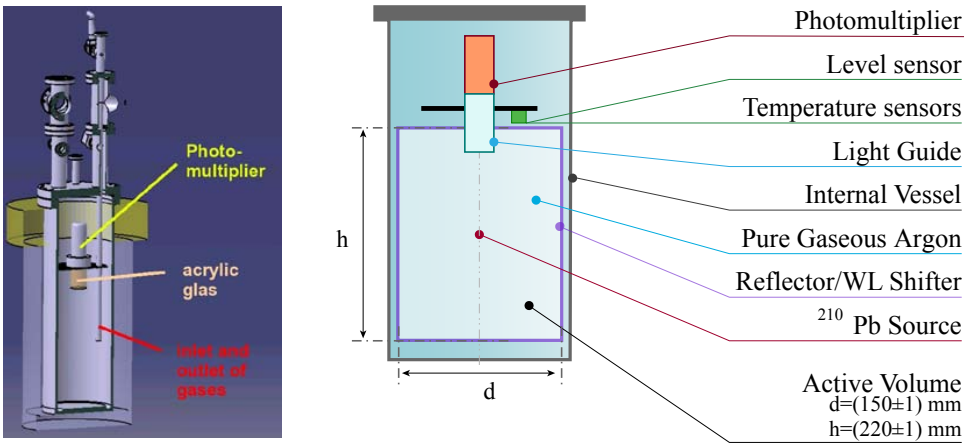

Figure 4.1: Schema of the Cell '05 setup.

The output signal of the PMT was amplified by a factor of 10 with a fast NIM amplifier (CAEN N979) and then digitized by a 8bit 1GS/s fast-ADC channel of a LeCroy WP7100 digital oscilloscope. The data were structured event-wise in several files containing 1000 events with an acquisition time window of 20 μs (20 kSamples).

A 50 Bq $^{210}_{82}$Pb source emitting 5.3 MeV αs and βs with a Q-value of 1.16 MeV was mounted in the center of the detector (Fig. 4.1). The decay chain of $^{210}_{82}$Pb is the following:

$$^{210}_{82}\mathrm{Pb} \xrightarrow[0.017\ \mathrm{Mev}]{[22.2\ y]\ \beta} {}^{210}_{83}\mathrm{Bi} \xrightarrow[1.16\ \mathrm{Mev}]{[5\ d]\ \beta} {}^{210}_{84}\mathrm{Po} \xrightarrow[5.304\ \mathrm{Mev}]{[138\ d]\ \alpha} {}^{206}_{82}\mathrm{Pb} \qquad \text{(from Ref.[90])}. \tag{4.1}$$

All the data sets were collected at room temperature except for the last set which was taken at $T = -20°$ C ($P_{air} = 2 \cdot 10^{-6}$ mbar).

4.1.2 Measurement techniques

A typical signal from the scintillation light induced by an $\alpha-$particle in GAr is shown in Fig. 4.2 (left). The digitized signal can be affected by an offset or low frequency noise. In this case the distribution of the values sampled before the light is detected might not be centered around 0. This effect can be corrected by digitizing the signal few μs before the trigger occurs (pedestal region) to calculate the average shift v_{off} which is subtracted from all the sampled values. If only white noise is present the histogram of the pedestal values can be fitted with a gaussian curve, as shown in Fig. 4.2 (right).

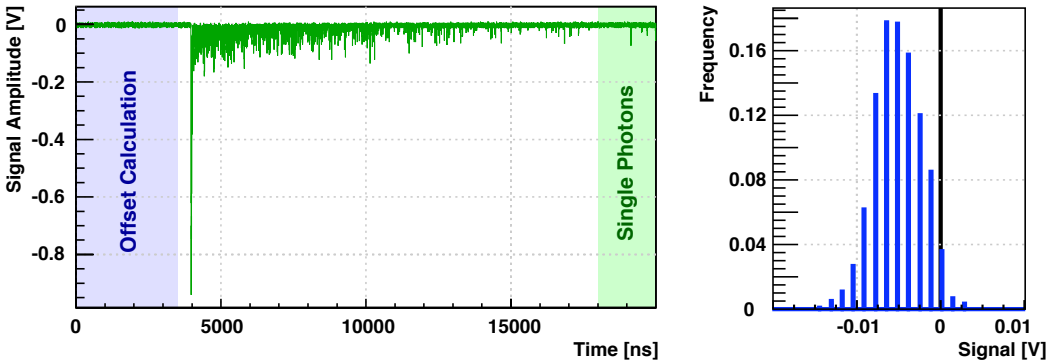

Figure 4.2: Left: Typical scintillation light signal induced by $\alpha-$particle in GAr (see text). **Right:** Pedestal distribution.

4.1.2.1 Average Pulse Shape

The average pulse shape (APS) for the selected $\alpha-$subsamples (with N_α events) was calculated. For each time t (bin size = 1 ns) the average signal $\overline{v}[t]$ and standard deviation

$\sigma_v[t]$ were calculated as follows:

$$\overline{v}[t] = \frac{1}{N_\alpha}\sum_{j=0}^{N_\alpha} v_j[t] \qquad \text{and} \qquad \sigma_v[t] = \sqrt{\frac{1}{N_\alpha - 1}\sum_{j=0}^{N_\alpha}(v_j[t] - \overline{v}[t])^2}. \tag{4.2}$$

The time dependence of the average signal for $\alpha-$particle for a pressure of $P_{air} = 2 \cdot 10^{-6}$ mbar is shown in Fig. 4.3. The black band corresponds to the average signal while the green band represents the $\sigma_v[t]$ distribution, with $\sigma_v[t]$ defined in Eq. 4.2. The two exponential decay times are emphasized by the semi-logarithmic representation. The decay times of the two components (τ_1, τ_2) and their intensities (A and B) have been obtained by fitting the distributions with the function:

$$f_{2C}(t) = G(t-t_0,\sigma) \otimes \left[H(t-t_0)\left(\frac{A}{\tau_1}e^{-\frac{t-t_0}{\tau_1}} + \frac{B}{\tau_2}e^{-\frac{t-t_0}{\tau_2}}\right)\right] = \tag{4.3}$$

$$= \frac{A}{\sqrt{2\pi}\sigma}e^{\left(\frac{\sigma^2}{2\tau_1^2} - \frac{(t-t_0)}{\tau_1}\right)}\left[1 - Erf\left(\frac{\sigma^2 - \tau_1\,(t-t_0)}{\sqrt{2}\;\sigma\;\tau_1}\right)\right] + \tag{4.4}$$

$$+ \frac{B}{\sqrt{2\pi}\sigma}e^{\left(\frac{\sigma^2}{2\tau_2^2} - \frac{(t-t_0)}{\tau_2}\right)}\left[1 - Erf\left(\frac{\sigma^2 - \tau_2\,(t-t_0)}{\sqrt{2}\;\sigma\;\tau_2}\right)\right],$$

where $G(t-t_0,\sigma)$ is a gaussian function normalized to 1 with σ representing the PMT resolution effects (transit time spread and ADC sampling). The fitted function agrees well with data except for the region between 50 - 150 ns from the peak. The slight excess of data, visible in Fig. 4.3 (inset), can be interpreted as an additional radiative process. This effect is modeled with an additional decaying exponential term added to Eq. 4.4.

$$f_{3C}(t) = f_{2C}(t) + \frac{C}{\sqrt{2\pi}\sigma}e^{\left(\frac{\sigma^2}{2\tau_3^2} - \frac{(t-t_0)}{\tau_3}\right)}\left[1 - Erf\left(\frac{\sigma^2 - \tau_3\,(t-t_0)}{\sqrt{2}\;\sigma\;\tau_3}\right)\right]. \tag{4.5}$$

Evidences for the decay of this *intermediate* state have also been reported in Ref. [44, 48] but might instead be related to photomultiplier afterglow effects.

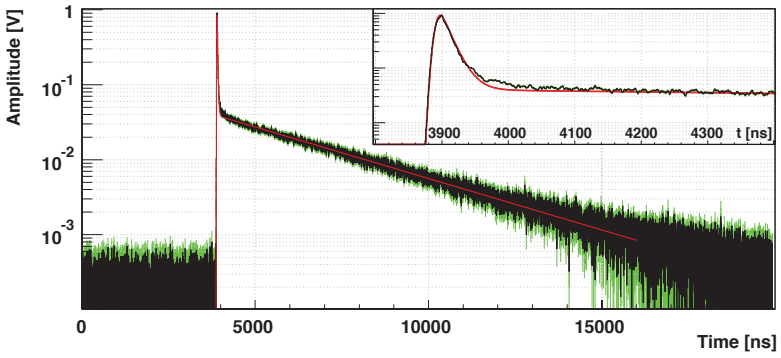

Figure 4.3: Distribution of the average pulse shape (APS) for $P_{air} = 2 \cdot 10^{-6}$ mbar (black), noise distributions (green) and fit with Eq. 4.4 (red).

4.1.2.2 Integrated Pulse Height

The integral of the digitized signal or *Integrated Pulse Height* (IPH) can be defined event by event as:

$$\mathrm{IPH} = \sum_{t_0}^{t_1} v[t]\Delta t, \tag{4.6}$$

where t_0 and t_1 define the integration interval and Δt is the sampling time ($\Delta t = 1$ ns for a sampling speed of 1 GSamples/sec). Typically the integration time interval extends for $3 \cdot \tau_2$ (decay time of the slowest component of the scintillation light) and is defined with respect to the peak time of the signal t_{peak} such that $t_0 = t_{peak} - 20$ ns and $t_1 = t_{peak} + 3 \cdot \tau_2$.

The amount of scintillation light detected is proportional to the charge collected on the anode (Q_{anode}). The current generated by the flowing charges is transformed into a voltage v across the internal resistance of the ADC channel ($\mathrm{R}_L = 50\ \Omega$). The number N of photoelectrons (p.e.) is defined as:

$$\begin{aligned} N_{p.e.} &= \frac{Q_{anode}}{k} = \frac{1}{k} \cdot \int_{t_0}^{t_1} I_{anode}\ dt = \frac{1}{k} \cdot \int_{t_0}^{t_1} \frac{v(t)}{R_L}\ dt = \\ &= \frac{1}{kR_L} \cdot \int_{t_0}^{t_1} v(t)\ dt = \frac{\sum_{t_0}^{t_1} v[t]\Delta t}{kR_L} = \frac{\mathrm{IPH}}{kR_L} \end{aligned} \tag{4.7}$$

where k is the mean charge collected on the anode for single photon pulses (1 photoelectron) and R_L is the input resistance of the digital oscilloscope.

The calibration of the photomultiplier can be performed using the scintillation light from the tail of the distribution for $\alpha-$particles which is composed of isolated single photons, as can be seen from the GAr event in Fig. 4.2 (left). A region of 2 μs for $(t - t_{trigger}) > 14$ μs (green area) is searched with a peak finding algorithm and the charge of the identified peaks is calculated. The distribution of this values corresponds to the charge distribution of the single photons. The measured calibration constant k used for the following analysis is (0.147 ± 0.005) nVs/p.e. which corresponds to a gain of $(1.8 \pm 0.1) \times 10^6$, for which the typical height of a single photoelectron pulse is roughly 3.5 mV (35 mV after $10\times$ amplification).

4.1.3 Data analysis

Nine data sets were collected with different air partial pressures ranging from 1 mbar to 2×10^{-6} mbar. In the IPH distributions two peaks can be identified, as shown in Fig. 4.4 (left) for $P_{air} = 2 \cdot 10^{-6}$ mbar. The first at 30 - 50 photoelectrons (p.e.) due to the low energy electrons from the $\beta-$decay and the second at about 1000 p.e. due to scintillation of $\alpha-$particles. The $\alpha-$peaks were fitted with a gaussian distribution and events within $\pm\ 3\sigma$ of the peak value were selected. For the IPH shown in Fig. 4.4 (left) 321 events were selected from the total sample of 528 events. The light yield of $\alpha-$particles is shown in Fig. 4.4 (right) for all the data sets as a function of partial air pressure.

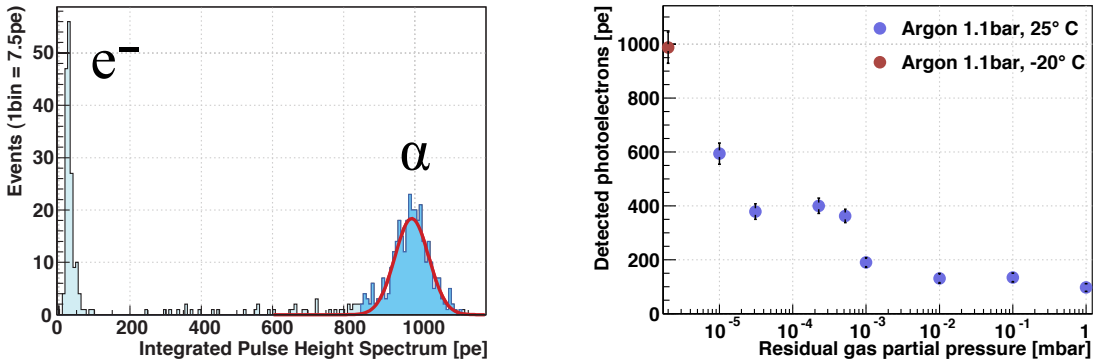

Figure 4.4: Left: IPH distribution for $P_{air} = 2 \cdot 10^{-6}$ mbar. **Right:** Light yield of α particles as a function of partial air pressure.

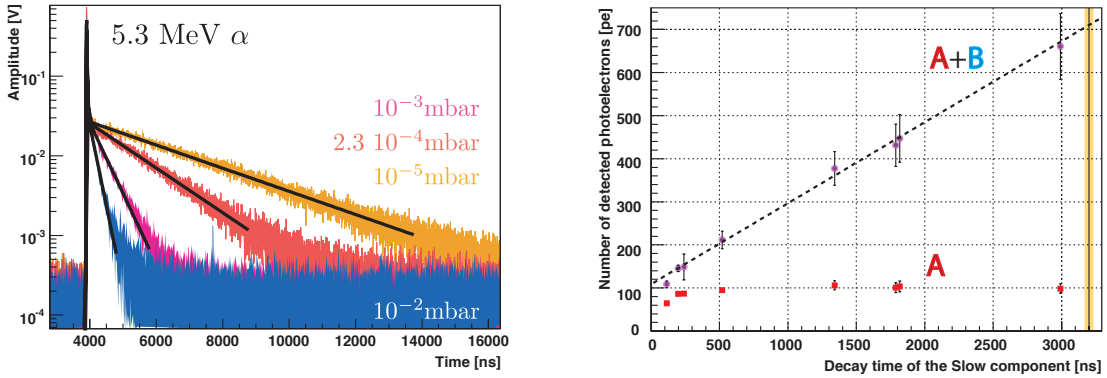

Figure 4.5: Left: Comparison of time distributions for different partial air pressures; $P_{air} = 10^{-2}$ mbar (blue), $P_{air} = 10^{-3}$ mbar (violet), $P_{air} = 2.3 \cdot 10^{-4}$ mbar (red) and $P_{air} = 2.3 \cdot 10^{-4}$ mbar (orange). **Right:** Parameters A and A+B from the two decay exponential model, plotted as a function of the decay time of the triplet state (τ_2).

The number of detected photoelectrons clearly depends on the purity of the argon even below 10^{-5} mbar where the contribution of the surface outgassing is dominant. The last measurement is determined by the minimum pressure that could be obtained in the vessel ($2 \cdot 10^{-6}$ mbar). This was achieved by cooling the external walls of the dewar with liquid nitrogen (LN_2), while the internal temperature of the gas was below water freezing point (T=−20°C).

For low purity condition ($P_{air} > 5 \cdot 10^{-4}$ mbar, $\tau_2 < 1300$ ns) the intermediate and the slow component were not correctly reconstructed by the fit with Eq. 4.5. For this reason the fit with the two exponential decays model (Eq. 4.4) ignoring the intermediate region was preferred to the three exponential decays model (Eq. 4.5). The APS distributions for various air partial pressures (10^{-2}, 10^{-3}, $2.3 \cdot 10^{-4}$ and 10^{-5} mbar) are shown in Fig. 4.5 (left) with the corresponding fits using Eq. 4.4.

4.1.4 Results

The decay time of the fast component (third continuum) is constant for partial air pressures below 10^{-1} mbar and the average value $\overline{\tau}_1$ is 11.3 ± 2.8 ns. This is compatible with the values measured in Ref. [42, 45], except for the points measured at very low purity conditions. The maximum measured values of τ_2 are $\tau_2 = (3140 \pm 67)$ ns and $\tau_2 = (3207 \pm 14)$ ns determined respectively with the 2 and 3 exponential decay models for an partial air pressure $P_{air} = 2 \cdot 10^{-6}$ mbar. Both are in good agreement with the measurement performed in Ref. [45].

The presence of water might be responsible for the non radiative destruction of the triplet state as the best purity could only be achieved by cooling down the detector below the water freezing point (T=−20 C). This result is supported also by the fact that the presence of nitrogen does not cause any strong suppression of the VUV light (Ref. [91]).

In first approximation the parameters A and τ_1 of Eq. 4.3 do not depend on gas purity. In contrast the correlation between the integral of the slow component B and its lifetime (τ_2) is remarkable. The relation is illustrated in Fig. 4.5 (right) where the prompt (A) and the total light ($L = A + B$) are plotted as a function of τ_2. Assuming a linear relation between B and τ_2:

$$L(\tau_2) = \varepsilon_{\text{fast}} \cdot \Sigma_{\text{fast}} + \varepsilon_t \cdot \Sigma_t(\tau_2) = A + B(\tau_2) = A + b \cdot \tau_2, \tag{4.8}$$

where Σ_{fast} and $\varepsilon_{\text{fast}}$ are respectively the population and the conversion/detection efficiency of the fast decaying state while Σ_t and ε_t are the corresponding quantities for the triplet state. $B(\tau_2)$ reaches its maximum ($B_{\max}$) for $\tau_2 = \tau_2^{\max} \sim 3.2\mu$s (see Section 2.2.1).

The ratio R between the population of the fast and slow decaying states is calculated by:

$$R = \frac{B_{\max}}{A} = \frac{B(\tau_2)}{A} \frac{\tau_2^{\max}}{\tau_2^{\text{meas}}}, \tag{4.9}$$

extrapolating B to the maximum purity ($\tau_2^{\max}$) with Eq. 4.8 as can be seen in Fig. 4.5 (right). For 5.3 MeV αs in clean gas at 1.1 bar $R = 5.5 \pm 0.6$ (using $\tau_2^{\text{meas}} = 3.14$ μs from the measurement at $P_{air} = 2 \cdot 10^{-6}$ mbar fitted with Eq. 4.4).

The relative intensities of the components (p_{fast}, p_{slow} and p_{int}), which are defined as the ratio of the different components (A, $B_{\max}$ and C) to the total light extrapolated to the maximum light yield (L_{tot}), can be calculated as follows:

$$\begin{aligned} L_{tot} &= A + B(\tau_2)\frac{\tau_2^{\max}}{\tau_2^{\text{meas}}} + C, \\ p_{\text{fast}} &= \frac{A}{L_{tot}}, \qquad p_{\text{slow}} = \frac{B_{\max}}{L_{tot}} = \frac{B(\tau_2)}{L_{tot}} \cdot \frac{\tau_2^{\max}}{\tau_2^{\text{meas}}} \quad \text{and} \quad p_{\text{int}} = \frac{C}{L_{tot}}, \end{aligned} \tag{4.10}$$

where $p_{\text{int}} = 0$ for the two-exponential decays model. Fitting the average pulse with the two-exponential decays model 84.1% of the light is attributed to the fast component and 15.9% to the slow component. In the case of the three-exponential decays model the light attributed to the fast component is 83% while the rest is divided between the fast and the intermediate (14.3% and 2.7% respectively) as shown in Fig. 4.2.

model	p_{fast}	p_{slow}	p_{int}
2 components	0.159 ± 0.014	0.841 ± 0.014	–
3 components	0.143 ± 0.002	0.830 ± 0.002	0.027 ± 0.001

Table 4.2: Relative intensities of the components in GAr for the two fitting models.

4.2 Optimization of the wavelength shifter

4.2.1 Experimental setup (Cell '06)

The measurements were performed with the apparatus illustrated in Fig. 4.6 which is similar to the one described in Chapter 4.1 (Fig. 4.1.1). In preparation for the LAr measurement the PMT was substituted with a Hamamatsu R6237-1mod (76×76 mm^2) PMT. The standard bialkali photocathode had a platinum (Pt) underlay which allows charge restoration at cryogenic temperature when bialkali becomes insulant. The PMT was rather slow and had a rise time of 6 ns (t_{rise}) while the time transit spread was not specified. The PMT was mounted on the top of an aluminum support, while the shifting reflector foil under test was mounted on the side walls, as shown in Fig. 4.6 (left). A 50 Bq ^{210}Pb source (Eq. 4.1) was inserted in the center of the detector. The vessel was then evacuated to about $2 \cdot 10^{-6}$ mbar and filled directly with pure GAr (Ar60). The output signal of the PMT was sampled in the same way as in Chapter 4.1 and analyzed off-line.

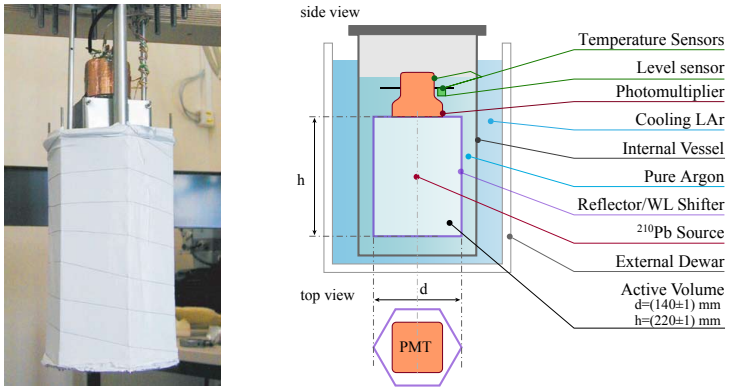

Figure 4.6: Schema of the *Cell '06* setup.

ArDM requires a strong electric field to drift the electrons to the charge detector. The WLS reflectors will have to be installed in a high electric field region directly on the field shaping electrodes. Therefore the search of the optimal reflector material was focussed mainly on two metal-free non conductive materials. These materials were chosen as reflector for the tests:

- **3M ESR Vikuiti** foils (Enhanced Specular Reflector) are metal free multi-layer polymeric films with 98.5% reflectance over the entire visible spectrum which absorb

wavelengths below 200 nm. These films were used for configurations **a**, **b** and **c** (described below);

- **Tetratex** Poly-Tetra-Fluoro-Ethylene(PTFE) membranes are permeable to gasses, chemically inert and have very good diffusive reflection properties for wavelengths above 200 nm (Ref. [79]), they were used for configurations **d** and **e**;

- **MgF_2-Al** coated foils (Braem's foils). MgF_2 and Al were evaporated on 125 μm Mylar foil (thicknesses: $MgF_2 \approx 25$ nm, Al ≈ 85 nm). They have 90 - 95% total reflectance in the range between 190 nm and 600 nm. The reflectors were prepared by the *Thin Film and Glass Laboratory*[4] at CERN. However the reflectance in the VUV range below 180 nm is not known. It was used for configuration **f**.

The Tetratex and the 3M foil reflectors were coated with sprayed TPB dissolved in acetone (≈ 0.2 mg/cm^2) while the MgF_2 reflector (Tab. 4.3 f), which is a VUV reflector, was left uncoated. The same 3M foil reflector was used in the configurations **a**, **b** and **c** with different coatings on the PMT photocathode. In the first case (**a**) the PMT was dipped in a solution of TPB and PolyStyrene dissolved in chloroform (Ratio TPB : PolyStyrene = 1 : 1). A solution of 24 mg of TPB dissolved in acetone was sprayed on the PMT photocathode for the configuration **b** while for the configuration **c** the coating was removed from the photocathode. The Tetratex reflector was in the configurations **e** and **d** together with the PMT whose photocathode was airbrushed respectively with < 10 mg and 24 mg of TPB dissolved in acetone. The coated PMT used in the configuration **d** was used also for the configuration **f** together with an uncoated MgF_2 reflector. A summary of the 6 different coating configurations is shown in Tab. 4.3. Pictures of the PMT photocathodes coated with TPB-PS, airbrushed with TPB dissolved in acetone and the uncoated are shown in Fig. 4.7.

4.2.2 PMT calibration with LED

To achieve a better PMT calibration a blue LED ($\lambda_{peak} = 400$ nm) was installed in the dewar and connected to a Lecroy 9210 pulse generator. Single photons signals on the PMT were obtained by pulsing the LED with a short signal ($V_{peak} \sim 1.7$ V and a width of 20 ns). The data acquisition was triggered by the pulser. The anodic signal of the PMT was amplified by a factor of 10 with a fast NIM amplifier (CAEN N979). For each calibration measurement 10 - 20 k events were acquired sampling a time window of 200 ns as the typical pulse width of the single photon signal is about 10 ns. The IPH of the events was calculated and fitted with:

$$f_{cal}(x) = M_0 \, e^{-\frac{1}{2}(\frac{x-\mu_0}{\sigma_0})^2} + M_1 \, e^{-\frac{1}{2}(\frac{x-\mu_1}{\sigma_1})^2}, \tag{4.11}$$

which is the sum of 2 gaussian functions where:

- μ_0 and σ_0 are the pedestal mean value and its standard deviation in unit of nVs;

[4]Courtesy of A. Braem, CERN PH - Detector Technologies

	PMT		Reflector		
	Coating	Thickness [mg/cm^2]	Material	Coating	Thickness [mg/cm^2]
a	Dipped in TPB/PS	–	3M foil	Sprayed	0.20 ± 0.01
b	Sprayed	≈ 0.4	3M foil	Sprayed	0.20 ± 0.01
c	none	–	3M foil	Sprayed	0.20 ± 0.01
d	Sprayed	≈ 0.4	Tetratex	Sprayed	0.19 ± 0.01
e	Sprayed	$\ll 0.2$	Tetratex	Sprayed	0.19 ± 0.01
f	Sprayed	≈ 0.4	MgF_2	none	–

Table 4.3: Reflector and PMT coating configurations.

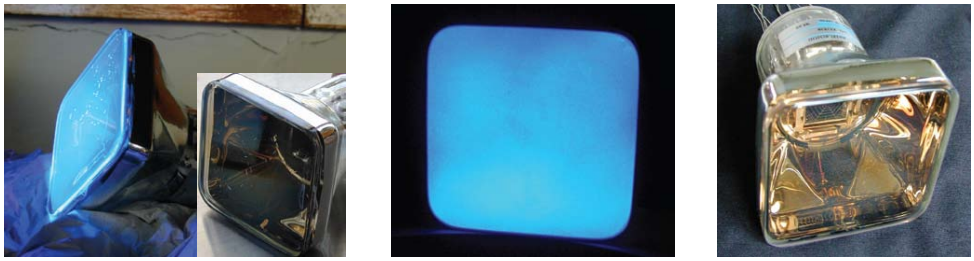

photo-cathode dipped in TPB-PS | photo-cathode sprayed with TPB | clean photo-cathode

Figure 4.7: Different PMT coatings.

- μ_1 and σ_1 are the calibration constant (the IPH value for one photoelectron), and its standard deviation, respectively, in unit of nVs;

With this method a 5 % precision on the calibration constant μ_1 was obtained.

4.2.3 Measurement techniques

The preparation of every measurement requires the installation of a new reflector or the modification of the PMT coating, and it is difficult to reproduce the same gas purity condition in successive measurements. Therefore it was decided to measure the scintillation light yield from $\alpha-$particles extrapolated to the maximum purity condition in gaseous argon ($\tau_2^{\max} = 3.2\mu$s) as explained in Section 4.1.

This setup was not optimized for measurement with high GAr purity and the GAr was not flown through the *oxisorb* purification cartridge. After pumping the detector to about $2 \cdot 10^{-6}$ mbar and filling it with 1.2 bar of pure GAr, typical values of $\tau_2 = 1300$ - 1800 ns were obtained.

A single measurement is in principle sufficient to determine the population of the fast and slow states and the decay time of the slow component, but the extrapolation error to $\tau_2^{\max}$ is fairly large. Therefore the scintillation light was measured at different gas purities and the light yield determined by fitting the dependence of B from τ_2, as explained in Section 4.1.

In the commissioning of ionization chambers or other gaseous detectors where evacuation is not possible, the active volume is simply flushed for hours or days with very pure gas mixtures before operation starts. Measurements with increasing lifetime of the slow component were taken by flushing the internal vessel with pure GAr. This effect can be seen in Fig. 4.8 (left) for which the lifetime of the slow component and light yield from 5.3 MeV $\alpha-$particles are plotted as a function of time. The data shown in the plot correspond to the MgF_2 reflector (Tab. 4.3f) where a modest purity value was reached in approximately 60 minutes.

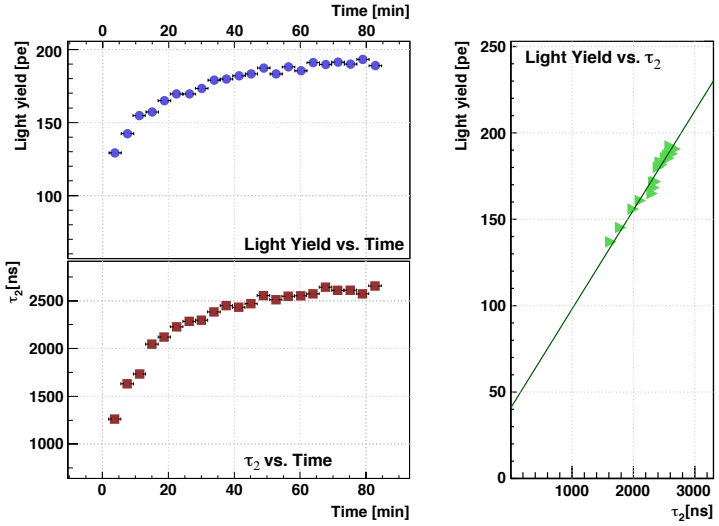

Figure 4.8: Left: Light yield and decay time measured as a function of time while flushing the cell with pure Ar, for the MgF_2 reflector (Tab. 4.3f). **Right:** Light yield in photoelectrons as a function of τ_2.

4.2.4 Data analysis

The 5.3 MeV $\alpha-$particles were selected as described in Section 4.1 and time distributions of each point were calculated with Eq. 4.2 and fitted with Eq. 4.3 to determine the lifetimes of the slow component τ_2. The light yield for $\alpha-$particles was determined by the fit of the IPH spectrum with a gaussian function. All the data sets were analyzed following this procedure. The plot of the mean value of the fitted gaussian is shown in Fig. 4.9 as a function of τ_2 for the six configurations.

The light yield for a given set of data i can be written as the sum of the light generated by the fast and the slow components (Σ_{fast} and Σ_{slow}) scaled with the proper detection/conversion efficiencies ($\varepsilon_i^{\text{fast}}$ and $\varepsilon_i^{\text{slow}}$). The amount of light produced by the slow component Σ_t depends linearly on its decay time (as described in Eq. 4.8) and can be rewritten as $\sigma_t \cdot \tau_2$, where σ_t is the quenching factor of the triplet state (slow component).

The detected light is then given by:

$$L_i(\tau_2) = \varepsilon_i^{\text{fast}} \cdot \Sigma_{\text{fast}} + \varepsilon_i^{\text{slow}} \cdot \Sigma_{\text{slow}}(\tau_2) = \varepsilon_i^{\text{fast}} \cdot \Sigma_{\text{fast}} + \varepsilon_i^{\text{slow}} \cdot \sigma_t \cdot \tau_2 = A_i + b_i \cdot \tau_2, \quad (4.12)$$

where b_i is the slope of the light yield vs. τ_2 (see Fig. 4.8 (right)). I now define the τ_{X} as the ratio of A_i/b_i:

$$\tau_{\text{X}} = \frac{A_i}{b_i} = \frac{\Sigma_{\text{fast}}}{\sigma_t} \frac{\varepsilon_i^{\text{fast}}}{\varepsilon_i^{\text{slow}}} \quad (4.13)$$

where the ratio $\Sigma_{\text{fast}}/\sigma_t$ is constant, since it depends only on gas properties. The ratio $\varepsilon^{\text{fast}}/\varepsilon^{\text{slow}}$ can also be assumed constant because it depends only on the properties of the WLS material which was the same for all the measurements. Therefore τ_{X} is constant and does not depend on the data set. Thus Eq. 4.12 can be written as:

$$L_i(\tau_2) = b_i \cdot (\tau_{\text{X}} + \tau_2), \quad (4.14)$$

which is a sheaf of lines with slopes b_i crossing the τ_2-axis at the common point $-\tau_X$, independently on the light yield.

The data points of the measurement with different reflectors were fitted with Eq. 4.14 as illustrated in Fig. 4.9 leaving τ_{X} and the b_i as free parameters. The result of the fit give $\tau_{\text{X}} = -485^{+100}_{-150}$ ns; the ratio $R = B/A$ can then be derived directly from:

$$R = \frac{b_i \cdot \tau_2^{\max}}{A_i} = \frac{\tau_2^{\max}}{\tau_{\text{X}}} = 6.6^{+2.1}_{-1.5}, \quad (4.15)$$

which is compatible with the value given in Chapter 4.1 but less precise. The errors on the data points (light yield and τ_2) are very big for low values of purity because the data are taken while the light yield and τ_2 are changing. In addition this model is based on the assumption that the ratio between the two detection efficiencies, $\varepsilon_i^{\text{fast}}/\varepsilon_i^{\text{slow}}$ is constant for different setups.

4.2.5 Results

The best light yield was obtained with the 3M foil reflector and the PMT coated with sprayed TPB where 777 ± 7 photoelectrons were measured for the 5.3 MeV $\alpha-$particles, corresponding to about 0.15 p.e./keV$_\alpha$ ($\alpha-$recoils).

4.3 Optimization of the WLS thickness on reflectors

The measurements described in the previous section showed that the TPB sprayed on a 3M foil reflector was the best among the tested configurations. However it was found that the spraying method did not allow to obtain uniform and precise thickness of the coating.

A professional way to deposit thin layers or films of material, without the use of solvents, is evaporation. A comparison of evaporated and sprayed 3M foil samples illuminated with UV light (254 nm) is shown in Fig. 4.10 (right). The coating done by evaporation of TPB

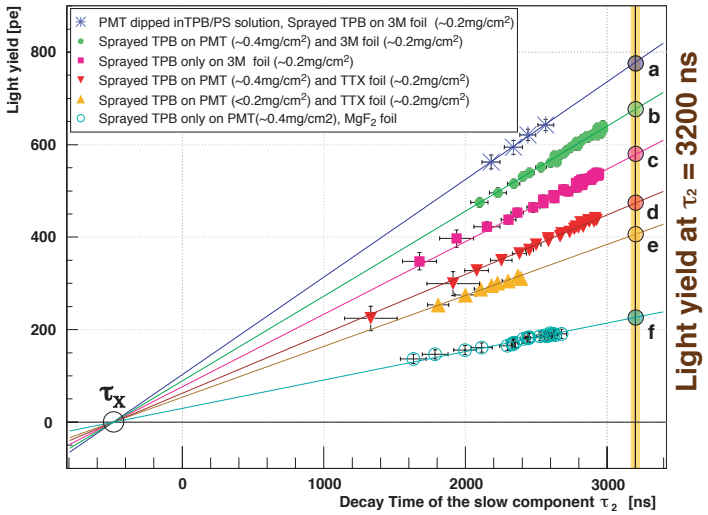

Figure 4.9: Light yield of the different configurations **a** to **f** plotted as a function of the decay time of the slow component τ_2. The distributions are fitted with the sheaf of straight lines described by Eq. 4.14. The light-yield is extrapolated to the maximum known purity $\tau_2^{\max} = 3.2\ \mu$s.

is uniform in contrast to the air-brush method which is characterized by the formation of small crystals as can be observed in the picture. The *brightness*, and consequently the light yield of the detector, are reduced by the presence of dark spots where no TPB is deposited and the formation of micro-crystals where the light can be trapped in.

A measurement setup and small a evaporation chamber were built to investigate, validate and optimize the evaporation method. In addition to the samples produced with our evaporator, several WLS coated reflectors were provided by *University of Sheffield*[5]. The measurement techniques were the same as the ones used in Chapter 4.2.3.

An inspection under the microscope showed that the evaporated samples appeared brighter than the ones obtained by the air-brush method. In fact the evaporation method avoids the formation of crystals where light could be trapped in. The measurement with one of the evaporated samples was compared to the results described in Section 4.2 and as can be seen from Fig. 4.10 (left). The light yield obtained with the evaporated reflector is about twice larger than the best configuration obtained by air-brushing.

4.3.1 Evaporator chamber

The evaporator chamber was built by refurbishing a 20 cm *Vacuum Desiccator*[6]. A picture of the evaporator with its vacuum system is shown in Fig. 4.11 (left).

TPB was placed in a ceramic crucible[7] installed in the bottom of the desiccator. To

[5]Courtesy of Dr. P.Lightfoot

[6]Thick glass vessel which can be evacuated. It is normally used to desiccate and remove the water from materials.

[7]Alumina (aluminium oxide) container.

perform evaporation the crucible was heated by flowing a current in a tungsten filament wrapped around the entire height of the crucible. The reflector was installed on a support $\sim$ 12 cm from the crucible. The system was then evacuated to 10^{-4} - 10^{-5} mbar using a primary dry pump and a turbo-molecular pump. When the evaporation condition were reached the heater was supplied with a constant current of 10 A for approximately 2 hours depending on the amount of WLS in the crucible. The final surface density of the TPB was measured by weighting the reflector before and after evaporation. The Sheffield reflectors were prepared with a commercially available evaporation chamber (Edwards E308) using a similar procedure. Fig. 4.11 (right) shows six reflectors with increasing TPB surface density illuminated by UV light (254 nm).

Many tests were performed before producing the reflector series, using different heating currents and with different starting pressure to optimize the evaporation procedure. In total 30 reflectors were prepared and tested, 22 of which were produced in our laboratory.

4.3.2 Experimental setup

The experimental setup consisted of a cylindrical 3"(78 mm) photomultiplier (ETL D750 UKFLB with 12 CsSb dynodes) inserted in an light tight aluminum tube, as shown in Fig. 4.12. The reflector was a 70 mm diameter disk with a 1 cm diameter hole in the center to allow the passage of the 5.5 MeV α-particles from the ^{241}Am source underneath. The source was mounted on movable stainless steel stick. The PMT was operated at room temperature with a gain of 10^7 ($V = -1350$ V). The output signal was digitized as described in Section 4.1.1.

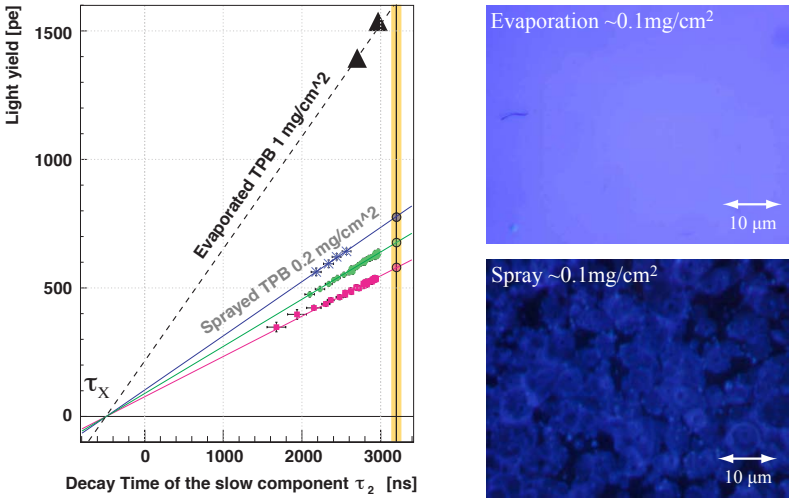

Figure 4.10: Left: Comparison between the light yield obtained by an evaporated reflector with the three best ones obtained by spraying method. **Right:** Microscope photographs of the surface structure of evaporated (top) and sprayed (bottom) TPB on 3M foil under UV light illumination (254 nm).

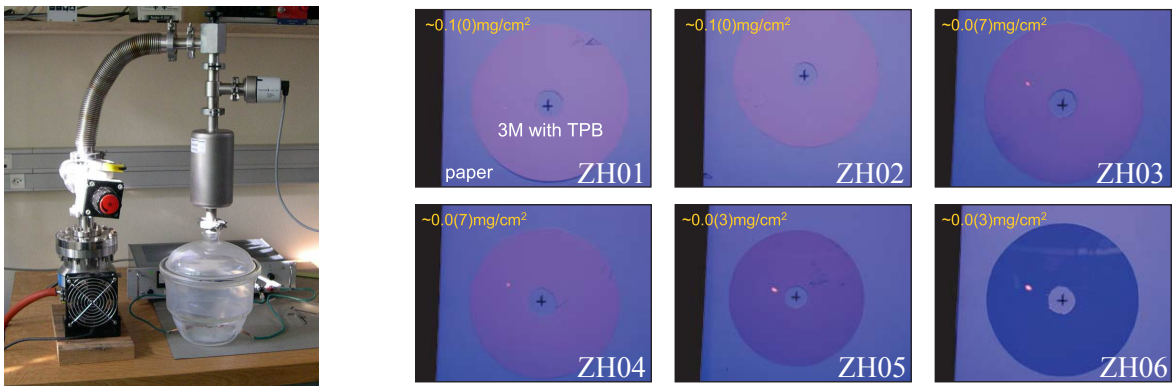

Figure 4.11: Left: Evaporator system used for the sample production at CERN. **Right:** Different reflectors illuminated with UV light (254 nm) and photographed with the same exposition time.

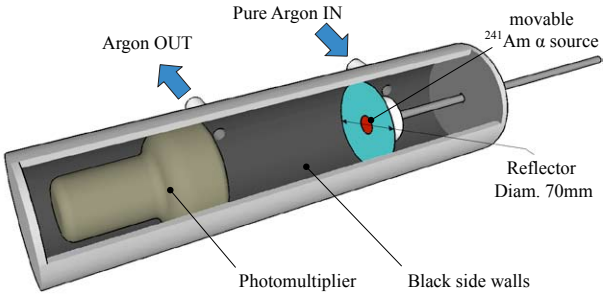

Figure 4.12: Experimental setup

4.3.3 Light yields

The effect of the TPB layer thickness on the conversion efficiencies can be already seen in Fig. 4.11 (right) where different reflectors were illuminated with UV light (254 nm) and photographed with the same exposure time.

Data were analyzed in Ref. [82] as shown in Section 4.2.4 and the data points were fitted with:

$$L_i^P = L_i + L_{offset} = b_i \cdot (\tau_X + \tau_2) + L_{offset} \tag{4.16}$$

where L_i is the sheaf of lines defined in Eq. 4.14 and L_{offset} is an offset parameter which takes into account the light detected when no TPB was evaporated on the disk. This offset is particularly important for low light yields as it represent a non negligible fraction of light. Data points (only 3M ESR reflector) and fit with Eq. 4.16 are shown in Fig. 4.13 (left).

The light yields were extrapolated to the maximum purity (red line) and plotted as a function of the TPB thicknesses in Fig. 4.13 (right). The result is consistent with a saturation of VUV conversion efficiency above 1 mg/cm^2 (the dashed line is meant to guide the eye). Errors on the plot are coming from the line fits. A very similar result is achieved by non constraining the lines to a common intersection point but produces larger

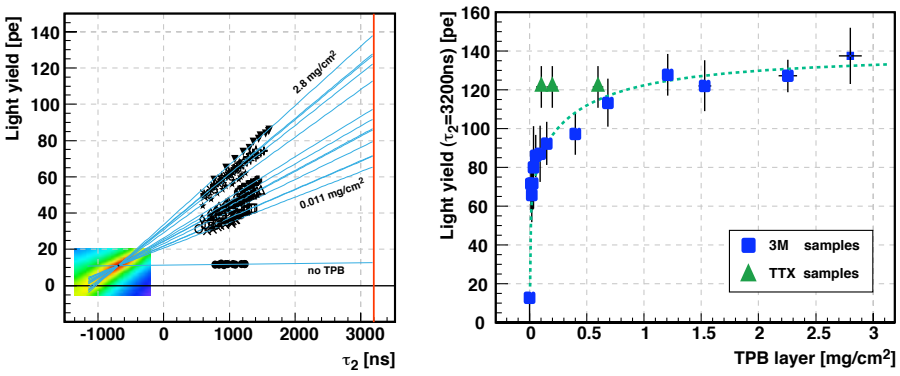

Figure 4.13: Left: Light yield in photoelectrons vs lifetime of the slow scintillation component for various thicknesses of TPB coatings on 3M foil [82]. **Right:** Conversion efficiency (expressed as absolute yield in photoelectrons for an effective slow component of 3.2 μs) for the various thicknesses on 3M foil compared to a few measurements of TTX foils.

fluctuations. The measurements were repeated on three TTX samples (green triangles) showing generally good performance and a surprisingly weak dependance on the TPB layer thickness.

Conclusions

This chapter was dedicated to the preliminary measurements performed in GAr. Several important results were obtained.

The light yield for 5.3 MeV αs was measured in GAr for various residual air partial pressures. The effect of the impurities on the slow component of the scintillation light was investigated. The quenching of the triplet excimer state was attributed to the presence of water vapors. Two different fitting methods were compared for the determination of the relative intensity of the light components. The relative intensity of the scintillation components were determined with both models.

The longest decay time constant for the triplet state is $\tau_2 = 3207 \pm 14$ ns for the purest argon, obtained with the three exponential decays model. The relative intensity of the component was measured with the two and three-exponential decays models. In the case of two exp. decays model $p_{\text{fast}} = 84.1\%$ and $p_{\text{slow}} = 15.9\%$ while for three exp. decays model $p_{\text{fast}} = 83\%$ while the rest is divided between the fast and the intermediate ($p_{\text{slow}} = 14.3\%$ and $p_{\text{int}} = 2.7\%$ respectively).

I investigated the properties of several reflector materials coated with WLS using different deposition methods. The best light yield was obtained using 3M foil reflector and a transparent coating on the PMT. The evaporation technique gave the best result in terms of light yield, reflector production process and reliability. The coating of the light reflectors were optimized in GAr.

Chapter 5

Light collection studies in liquid argon

In this chapter I describe the construction of a LAr detector and the light yield measurements for different TPB coated reflectors in LAr. The Cell'06 detector (described in Section 4.2) was equipped with a second PMT and the active volume reduced to about 1 ℓ. The support cage was replaced with a stainless steel structure which allowed the achievement of a better purity and an easier substitution of the reflectors. The optimization of the reflectors with the VUV scintillation light in GAr was performed in LAr before preparing the final side reflectors for ArDM.

A large evaporator chamber was build for the ArDM reflector production. Four series of reflectors with different TPB coating thicknesses were produced with this evaporator and tested with the Cell'07 detector with which the relative wavelength-shifting efficiencies of the reflectors were measured and compared using the scintillation light produced from $\alpha-$particles in LAr.

The *pulse shape discrimination* (PSD) techniques were introduced in the analysis algorithms to identify the different ionizing particles (α, β) from the internal ^{210}Pb source.

5.1 Experimental setup (Cell '07)

As mentioned before the apparatus described in Chapter 4.1 and 4.2 was modified to contain 2 cryogenic Hamamatsu R6237-1mod PMTs. To achieve a high light yield the active volume was reduced to 1 ℓ and the PMTs were mounted face to face at a distance of 102 ± 2 mm on a stainless steel support. The wavelength-shifting reflectors (10×10 cm^2) were mounted on the four sides of the cell, as shown in Fig. 5.1. A ^{210}Pb radioactive source with an activity of 50 Bq was mounted in the center of the detector.

After the installation of the reflectors the vessel was evacuated to $\approx 5 \cdot 10^{-6}$ mbar, flushed with pure GAr (Ar60) and then evacuated again to ≈ 2 - $8 \cdot 10^{-7}$ mbar. The vacuum and the gas pressures were monitored with different *Pirani* and other capacitive gauges[1]. The

[1] PCR260 Active Pirani capacitive gauge.

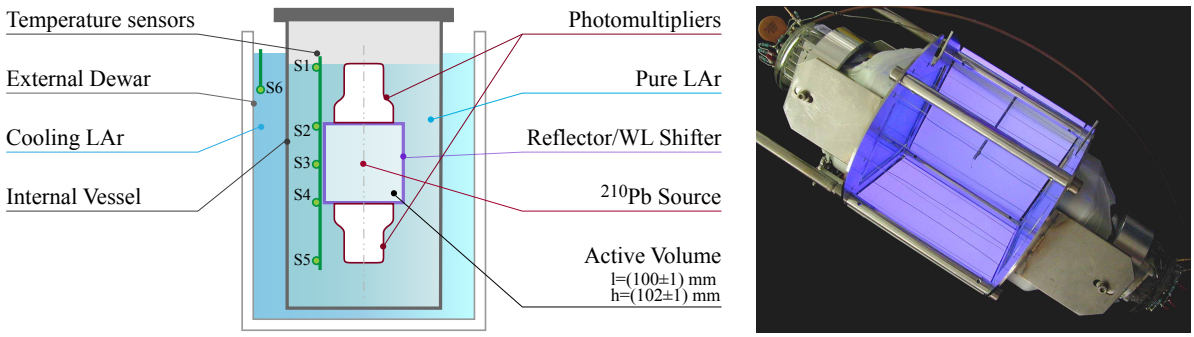

Figure 5.1: Left: Sketch of the *Cell '07* setup. **Right**: The light detector illuminated by UV light (254 nm) during the installation of the WLS reflectors.

temperature and the LAr level were monitored with six temperature sensors[2] mounted outside the active volume as shown in Fig. 5.1. Five of the temperatures sensors (S1 - 5) were distributed along the detector side while the last one (S6) was used to monitor the temperature of the cooling bath (*External Dewar*). The resistances of the Pt sensors were read out through a *National Instruments* acquisition card[3]. A *slow control* program was developed to collect the measurements of the different sensors every 5 - 120 s, depending on the status of the setup. The sampling was more frequent while cooling and liquifying argon gas, less frequently when the setup was in a stable condition.

Preliminary measurements were done using bulk LAr[4] from an external 200 ℓ dewar. The purity of this LAr ($\tau_2 < 800$ ns) was not sufficient to reach reasonable measuring conditions. The source of these impurities was traced to water and oxygen which were contaminating the argon in the refilling process of the dewar. To fill the *Internal Vessel* pure gaseous argon was liquified using a bath of bulk LAr. The thermodynamic status of the detector was monitored with the *slow control* system.

The PMTs were supplied with a voltage of -1400 V and operated at a gain of about $2 \cdot 10^6$. Higher gains could not be achieved due to the sparking of the voltage divider of the upper PMT because it remained in GAr. Calibrations of the PMT were performed with an LED as described in Section 4.2.2.

In total 5 sets of reflectors were tested in the Cell '07 detector. The coating on the first reflector set was made using the small evaporator chamber. Following the results of Section 4.3 the first set of four 10×10 cm^2 Tetratex foils was coated with a TPB surface density of 1.0 ± 0.1 mg/cm^2. The remaining 4 sets were coated using a large evaporator chamber which was build for the production of the ArDM reflectors (ArDM requires about 4 m^2 of TPB coated reflector).

[2]Pt1000 and Pt2000 Platinum Resistors.
[3]NI USB-6001
[4]Supplied by AirLiquid (France).

5.1.1 Large evaporator chamber

Following the experience gained with the different TPB deposition techniques described in Chapter 4, we built a stainless steel vacuum chamber large enough to house a single 25×125 cm^2 reflector sheet for the ArDM detector. The apparatus (shown in Fig. 5.2) consists mainly of two parts:

- an array of 13 crucibles - shown in Fig. 5.2 (left);
- a vacuum vessel.

The crucibles were electrically connected in series. The power dissipated from the heater on each crucible was about 3 Watts.

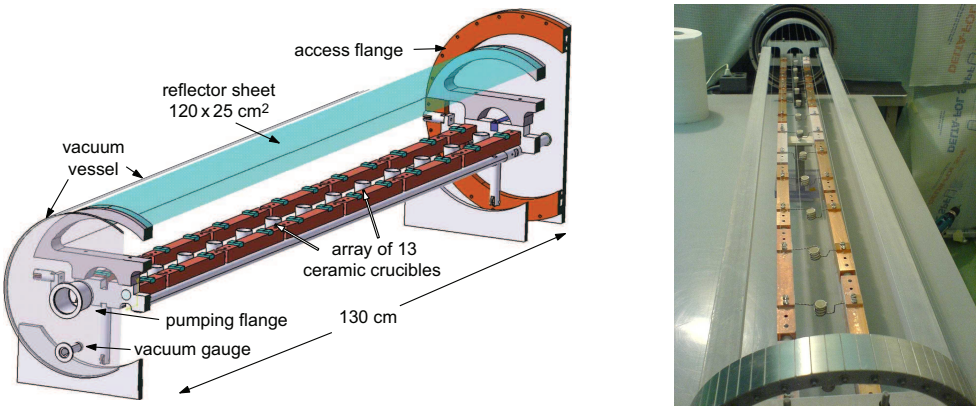

Figure 5.2: Left: Sketch of the large evaporator chamber. **Right:** Picture of the slide-in array.

The reflector sheets were supported by 100 μm thick wires. An evaporation cycle was started by filling the crucibles with TPB powder and positioning the reflector sheet on its support. The reflector sheet surface was gently wiped with a grounded antistatic brush before the apparatus was closed and pumped. After reaching a typical pressure of 10^{-5} mbar the heating current was switched on and left running for about 3 - 5 hours. The end of TPB evaporation was signaled by sudden decrease in the monitored vacuum pressure.

5.1.2 Preparation of the reflectors

Using the large evaporator described in Section 5.1.1 4 sets of reflectors were produced out of a 24×124 cm^2 Tetratex foil in a single evaporation procedure. Each reflector set corresponds to a 20×22 cm^2 area on the large Tetratex foil which was identified and marked prior to evaporation. The crucibles corresponding to each reflector set were filled with the desired quantities of TPB (0.1, 0.2, 0.3 and 0.4 g) while the ones in between sets contained intermediate quantities (0.15, 0.25 and 0.35 g) as shown in Fig. 5.3. The

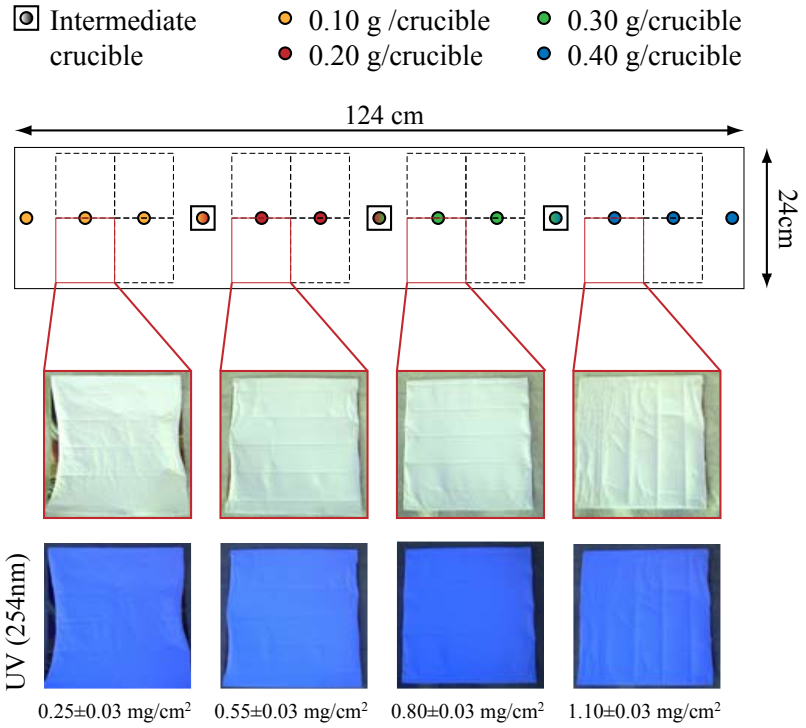

Figure 5.3: Preparation of the 4 reflector sets with the large evaporator chamber. The reflectors were made out a single 24×124 cm^2 Tetratex foil where TPB was evaporated with different densities. The pictures show the different reflectors illuminated by daylight and UV light (254 nm).

surface density of the coating layer was measured by weighting the reflector before and after the evaporation.

5.2 Measurement techniques

Each time a new set of reflectors was installed the *internal vessel* was evacuated to about $5 \cdot 10^{-6}$ mbar, flushed with pure GAr for about 30 min and then pumped again for about a week to about $2 \cdot 10^{-6}$ mbar. The *external dewar* was pre-cooled with a mixture or liquid N_2 and bulk LAr in such a way that the final temperature was greater than 85 K, which is the argon freezing point. The *internal vessel* was filled with pure GAr which started condensing on its cold walls. The GAr condensation flux was of about $10-20$ ℓ/min. The condensation was stopped when the uppermost temperature sensor (S1) was immersed in LAr. The temperature sensors showed a clear drop when immersed in LAr providing a reliable method to monitor the level of the LAr in the filling phase. The temporal evolution of the temperatures measured at different points of the detector is shown in Fig. 5.4.

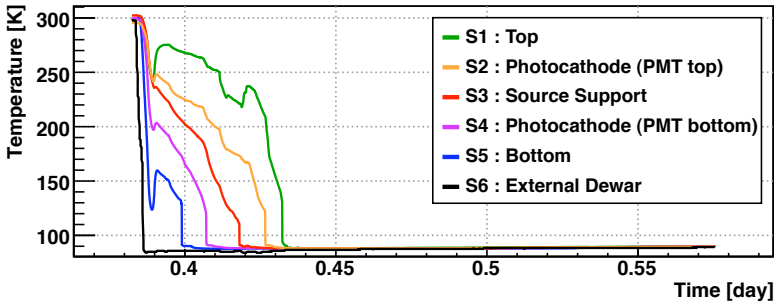

Figure 5.4: Temperature evolution for various sensors as a function of time when filling with LAr. The condensation of gas was stopped when the uppermost sensor (S1) was in LAr.

After the end of the condensation process the PMTs were supplied with a voltage of $V_{HV} = -1400$ V which corresponds to a gain of about 10^6. The voltage divider of the upper photomultiplier was operated in cold GAr and was sparking at voltages below $V_{HV} \simeq -1410$ V. For this reason higher gains could not be achieved. Few hours were required to let the photomultiplier thermalize and reach stable gain conditions.

The calibration constant was determined measuring the IPH distribution of the single photons as described in Section 4.2.2. The oscilloscope allows to set different thresholds for the two photomultipliers and to trigger the acquisition on the logic *OR* of the two channels. The trigger thresholds were set at about 500 photoelectrons on each channel and were low enough not to cut the $\alpha-$distributions ($V_{th} >> 50$mV).

5.3 Analysis techniques

The techniques developed to analyze the data collected in GAr are not sufficient for the analysis of the LAr scintillation light. As described in Chapter 2 the emission spectrum of LAr differs from the one of GAr. The fast and the slow components are now due to the radiative decays of the singlet and triplet states of the argon excimer (Ar_2^*) to the dissociative ground state (Ref. [39]) and in both cases the radiation has similar wavelength (128 ± 10 nm).

The ratio between the population of the singlet and the triplet states ($R = \Sigma_s/\Sigma_t$) depends on the ionization properties of the projectile. For nuclear, heavy ions and $\alpha-$particles interactions an additional quenching factor has to be taken into account because of the high excitation densities along the track core (bi-excitonic quenching, for more details see Section 2.3).

Each trace can be fitted with the proper function (Eq. 4.4), on the other hand this procedure might take very long time and requires the single photons in the tail of the distribution to be above the noise level.

5.3.1 Drift of the PMT gain in liquid argon

The gain of a photomultiplier depends on the potential difference between the dynodes and is sensitive to the fluctuations of the high voltage coming from the power-supply. As described in Ref. [92] the gain G is the product of the multiplication factors δ_i of the dynode chain:

$$\delta_i = a \cdot U_i^k \quad \rightarrow \quad G = \prod_{i=1}^{\text{N dynodes}} a \cdot U_i^k = a^N \cdot U^{N \cdot k} \quad \text{if } U_i \text{ is constant,} \tag{5.1}$$

where $U_i = V_i - V_{i-1}$ is the potential difference across the $i-$th dynode and the two parameters a and k are related to the material and the shape of the dynodes.

The parameters a and k have a small temperature dependence, but the δ_i have approximately the same values because the voltage divider is made of resistors of the same type with equal temperature coefficients. In stable thermodynamic conditions a or k are considered constant but in our case the PMT is undergoing a thermal shock of more than 200° C in less than an hour. Taking into account a generic temperature dependence of a and k the gain fluctuation can be described with the following equation:

$$G = a^N(T) \cdot U^{N \cdot k(T)} \quad \rightarrow \quad \frac{\Delta G}{G} = N \left(\frac{\Delta a(T)}{a(T)} + \Delta k(T) \cdot ln\ U \right) \tag{5.2}$$

The gain fluctuation is proportional to the number of stages, therefore small fluctuations of a or k have a large impact on the gain of PMTs with many dynodes if the thermodynamic conditions are not stable. Those parameters are normally not known but can be estimated experimentally. The maximum gain fluctuation during a measurement session was about 30 % for a PMT with 12 dynodes (Chapter 6) with a typical $U = 120$ V. Assuming a $\Delta a(T)/a(T) \sim 0.01$ and a $\Delta k(T) = 0$ the gain variation is 12 %.

The gain drifts consistently immediately after the cool-down, approaching an asymptotic value in a few hours. For this reason it is necessary to monitor the gain frequently during long measurement periods. Using a Lecroy WP7200 digital oscilloscope the calibration constants can be measured easily with single photons if the gain of the PMT is above than $5 \cdot 10^6$. For low gain the resolution of the oscilloscope is not sufficient to resolve the single photons and an analog amplifier must be inserted between the PMT and the digitizer.

A alternative strategy was used to avoid the disconnection and the reconnection of the PMT cables during the measurement. The drift of the peak of the $\alpha-$particles was monitored and the calibration of the photomultipliers with the LED were performed when the peak reached an asymptotic value.

5.3.2 Combining the signal of different PMTs

The output signal of several photomultipliers can be combined into a unique channel. Because of the different calibration factors the single signals are digitized and summed

off-line. I called *Virtual Channel* the sum of the signal of all the PMTs. To represent the virtual channel as a voltage a reference calibration (k_{ref}) was introduced. The total signal v_{tot} at the time t can be described as:

$$v_{tot}[t] = \frac{k_{ref}}{k_1}\, v_1[t] + \frac{k_{ref}}{k_2}\, v_2[t] \qquad \text{for 2 PMTs,} \tag{5.3}$$

where $v_1[t]$ and $v_2[t]$ are the signals of the two PMTs, k_1 and k_2 are their calibration constants and k_{ref} is the reference calibration.

For PMT of different types or for different cable lengths fixed delays d_m are introduced between the signals of the PMTs. These delays can be determined by pulsing all the PMTs with a synchronous LED signal and measuring the peak of the arrival time distributions. Eq. 5.3 can be generalized including the delays d_m and an arbitrary number of PMTs N:

$$v_{tot}[t] = \sum_{m=1}^{N} \frac{k_{ref}}{k_m}\, v_m[t + d_m] \qquad \text{for } N \text{ PMTs,} \tag{5.4}$$

where k_m is the calibration constant of the m-th photomultiplier.

5.3.3 Off-line particle selection - the Component Ratio

The distribution of the total collected light (IPH) is not sufficient to distinguish between different types of particle. In the case of the measurements with the ^{210}Po source for example, the $\beta-$spectrum of the ^{210}Bi decay (Eq. 4.1) partially overlaps with the 5.3 MeV $\alpha-$spectrum, as can be seen from the IPH distribution in Fig. 5.5 (first reflector tested).

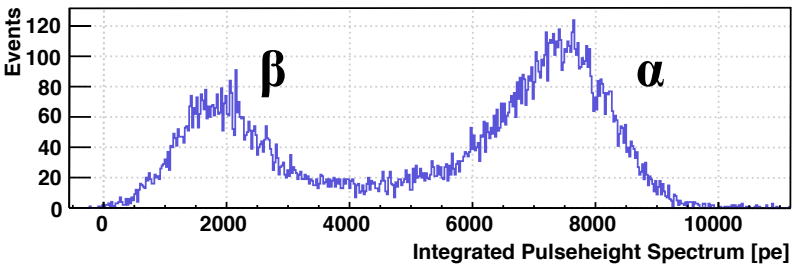

Figure 5.5: IPH of the scintillation light for the ^{210}Pb source in units of [p.e.].

As was discussed in Chapter 2 the relative populations of triplet and singlet states depend on the ionization density of the projectile. This property of the LAr scintillation can be used to unfold the two distributions event by event.

I called component ratio (CR) the relative contribution of the singlet state decays to the total scintillation light, which is calculated as the ratio between fast to total light:

$$\mathrm{CR} = \frac{\text{singlet}}{\text{singlet} + \text{triplet}} = \frac{\Sigma_{\text{fast}}}{\Sigma_{\text{fast}} + \Sigma_{\text{slow}}} = \frac{A}{A + B}, \tag{5.5}$$

where A and B are the singlet and triplet components in the notation of Eq. 4.4. The quantity $A+B$ corresponds also to the total integral of the signal (IPH) while the quantity A can only be determined by the fit.

In the measurements described in this chapter the gain of the PMTs and the resolution of the ADCs were (8 bits) were not sufficient to resolve the single photons in the tail of the light distribution. This affects the precision of the fit. A possible solution can be found by calculating the *prompt light* as the partial integral of the first 50 ns of the signal after the peak (about 3 τ_1) as:

$$\mathrm{IPH}_{\mathrm{Prompt}} = \sum_{t=t_1}^{t_2} v[t]\Delta t \simeq A = \Sigma_{\mathrm{fast}}, \tag{5.6}$$

where $t_1 = t_{peak} - 20$ ns and $t_2 = t_{peak} + 50$ ns. This quantity is a good approximation of the light of the singlet state decay because the decay time of the slow component is much longer than the decay time of the fast one. The CR is then approximated as the ratio between IPH(50 ns) and IPH, two quantities which are very easily calculated event-wise:

$$\mathrm{CR} = \frac{\Sigma_{\mathrm{fast}}}{\Sigma_{\mathrm{fast}} + \Sigma_{\mathrm{slow}}} \simeq \frac{\mathrm{IPH}_{\mathrm{Prompt}}}{\mathrm{IPH}}. \tag{5.7}$$

The CR does not dependent on the gain of the PMT however, it strongly depends on the integration error. Similar procedures are very common in *Pulse Shape Discrimination* (PSD) techniques (Ref. [71]) and have been widely used to unfold particle distributions.

The relation of the IPH with the CR is shown in Fig. 5.6 for the two different approaches. In Fig. 5.6 (left) the CR was obtained with Eq. 5.7 (approximated formula) while in Fig. 5.6 (right) was calculated with Eq. 5.5. In the second case the fit process was increasing significantly the computation time and the complexity of the analysis. In addition seed parameters had to be determined with a preliminary analysis step. In both cases the particles can be clearly identified.

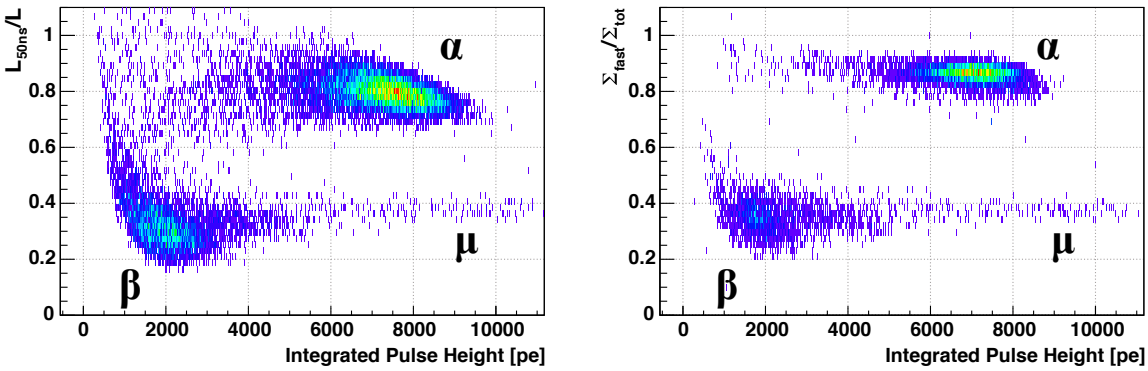

Figure 5.6: Comparison of different methods for CR calculation plotted as a function on the total light (IPH). On the left plot the CR was calculated with Eq. 5.7 while on the right one with Eq. 5.5.

The CR can be estimated also using the ratio between the population of the singlet and triplet states $R = \Sigma_s/\Sigma_t$:

$$\mathrm{CR} = \frac{\Sigma_s}{\Sigma_s + \Sigma_t} = \frac{R}{R+1} = \begin{cases} \alpha - \text{particles:} & R_\alpha = 3.3 & \rightarrow \mathrm{CR} \simeq 0.8, \\ \text{electrons} & R_e = 0.26 & \rightarrow \mathrm{CR} \simeq 0.2, \end{cases} \tag{5.8}$$

where R_α and R_e are the values measured in Ref. [35] for $\alpha-$particles and electrons respectively (described in Section 2.2.1).

The event-wise fit is the best option. On the other hand the approximated method was sufficient to remove the background or to select different particle topologies for the measurement presented in the following chapters. The fitting method has still some margin of improvement. Once the particle topologies are defined by measuring the relative population of the different components, it is possible to fix few parameters increasing the fitting performances.

5.3.4 Off-line particle selection - the Peak Time

The signal reaches its peak value a few ns after the trigger is generated, with a rise time which is typically 6 ns for a single photon. The trigger time is constant and the peak time (PT) can be easily calculated as the highest local maximum after the trigger. Low amplitude signals (above the trigger threshold) reach the peak value earlier than the large amplitude signals. For this reason the time difference between the trigger and the signal peak increases with signal amplitude. A typical peak time distribution for the ^{210}Pb source in LAr is shown in Fig. 5.7 (left). The inset shows a detailed view of the trigger region (1010 ns $< t <$ 1050 ns).

The peak time distribution appears to be the superimposition of two distributions, one of which is characterized by a narrow peak of 6 ns width at $t = 1037$ ns. The broader distribution corresponds the electron-recoil band while the narrower corresponds to the $\alpha-$particles. This interpretation was verified by introducing the CR variable (as defined in Section 5.3.3). The distribution of the CR as a function of the peak time shown in Fig. 5.7 (right) reveals that the narrow peak corresponds to CR $\simeq 0.8$ (typical of $\alpha-$particles) while the broader distribution corresponds to CR $\simeq 0.35$ (typical of electrons recoils).

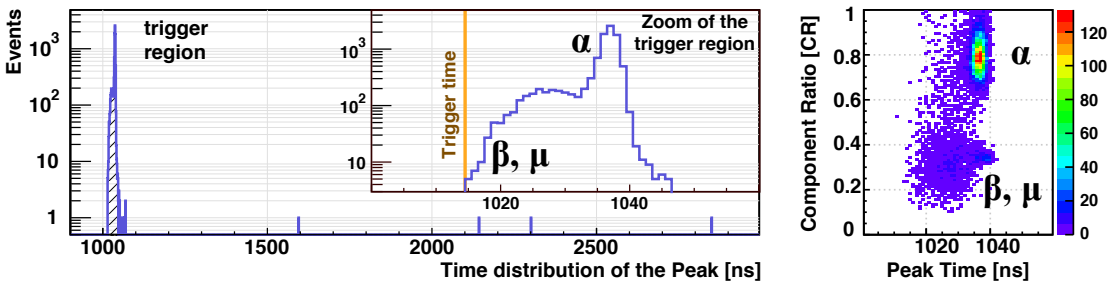

Figure 5.7: Left: Time distribution of the signal. The inset shows a zoom into trigger region (1010 ns $< t <$ 1050 ns). **Right:** Component ratio as a function of the peak time.

Some events (typically 0.05% for the Cell'07 detector) have the peak outside of the trigger region. Those events are affected by pile-up and are rejected by the analysis. The cut on the PT is very important in the case of the ArDM detector because the pile-up has a serious impact on the analysis results.

5.3.5 Off-line particle selection - the Pulse Height distribution

The *Pulse Height* (PH) is defined as the peak value of the digitized signal. The PH is strongly correlated with prompt light (defined in Eq. 5.6) as can be seen in Fig. 5.8. The slope of the distribution is used to convert the values of the trigger thresholds, which are normally defined in units of mV, to photoelectrons. In the case of Fig. 5.8 the slope is $s = 3.3 \pm 0.1$ p.e./mV.

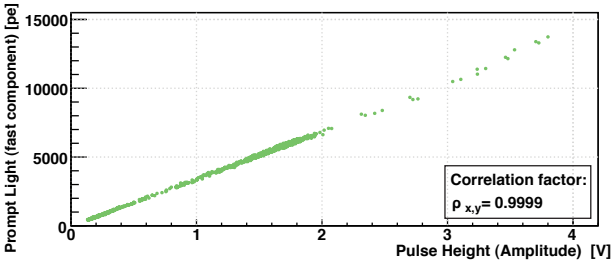

Figure 5.8: Correlation between the prompt light and the Pulse Height (PH) of the signal.

The correlation of the PH with the IPH is also very strong even if it depends on the type of ionizing particle as shown in Fig. 5.9. It is possible to identify two bands which merge together at lower values of IPH and PH. The long continuous band is associated with cosmic muons and β emission from the radioactive source while the almost isolated island with the $\alpha-$particles. The logarithmic scale emphasize the lower edges of the IPH distribution which appears to be strongly biased by the triggering conditions of the DAQ. However the biasing level depends on the particle type.

The signals which exceed the ADC ranges saturate the electronics ($V_{sat} \sim 4$ V). Part of the signal is lost and the total light will not be computed correctly. For this reason those events are normally rejected in the analysis process.

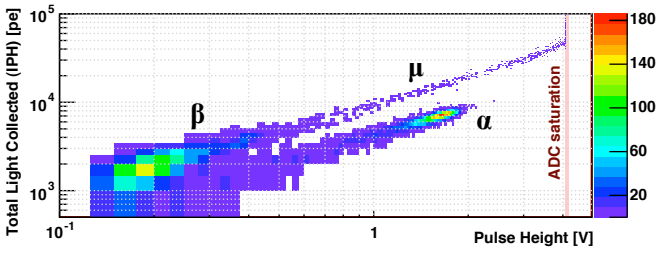

Figure 5.9: Distribution of the pulse height (IPH) as a function of the pulse height (PH) for $\alpha-$particles, electrons from the $\beta-$decays and muons.

5.4 Relative intensities of the scintillation components

The relative intensity of the components were measured for 3 different particle types:

- $\alpha-$particles from the ^{210}Po decay of the ^{210}Pb chain;
- electron from the Q=1.17 MeV $\beta-$decay of the ^{210}Pb chain;
- muons from cosmic rays.

The selection of different event topologies was performed using the following variables which were defined in Section 5.3: *Component Ratio* (CR), *Peak Time* (PT), *Integrated Pulse Height* (IPH) and *Pulse Height* (PH). The three particle categories were selected using CR and IPH as follows:

$$\alpha \;:\; 0.6 < \mathrm{CR} < 1.0 \quad \mathrm{AND} \quad 2500 \text{ p.e.} < \mathrm{IPH} < 10000 \text{ p.e.} \tag{5.9}$$

$$\beta \;:\; 0.1 < \mathrm{CR} < 0.5 \quad \mathrm{AND} \quad 1000 \text{ p.e.} < \mathrm{IPH} < 2500 \text{ p.e.} \tag{5.10}$$

$$\mu \;:\; 0.1 < \mathrm{CR} < 0.5 \quad \mathrm{AND} \quad 6000 \text{ p.e.} < \mathrm{IPH} < 11000 \text{ p.e.} \tag{5.11}$$

The IPH and CR selection criteria are shown in Fig. 5.10. In addition, the PT and the PH were used to reject the pile-up and the saturated events from the distributions by imposing:

- 1010 ns $<$ PT $<$ 1050 ns (peak in the allowed region)
- PH $<$ 4 V (no ADC saturation)

The different particle subsamples were selected from a single data set and the corresponding average pulse shapes were calculated and fitted with Eq. 4.5 to extract the scintillation light parameters. The fit parameters and their statistical errors are shown in Tab. 5.1. The two decaying exponential model was not considered for this analysis because it disagrees for 100 ns $< (t - t_{trig}) <$ 300 ns (intermediate range).

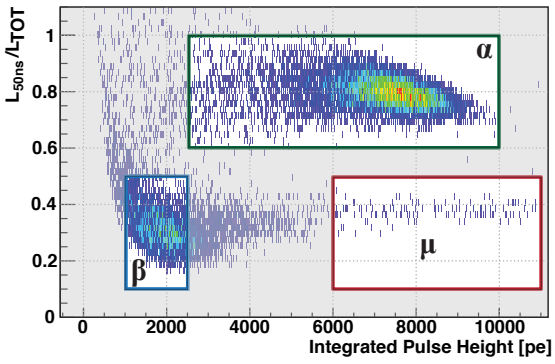

Figure 5.10: Selected events for the different topologies.

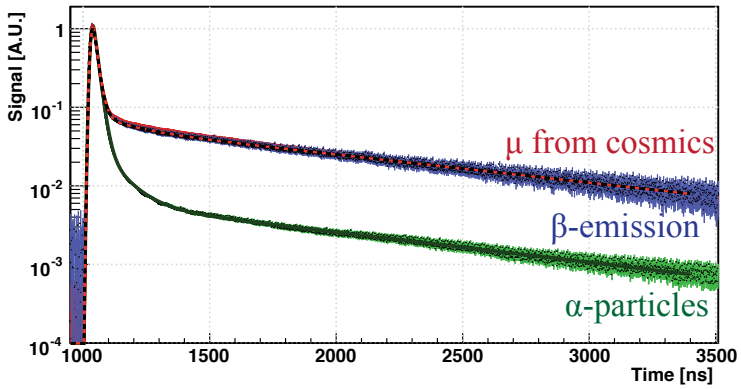

Figure 5.11: Average pulse shapes for different particle topologies normalized on the pulse height of the fast component; the distributions are fitted with Eq. 4.5 (3 exp. decays) and the result parameters are shown in the table below.

	Fit Parameters						Extrapolated
	Singlet	Triplet	Intermediate	Decay times			Triplet
Type	A [nVs]	B [nVs]	C [nVs]	τ_1 [ns]	τ_2 [ns]	τ_3 [ns]	B·(τ_2^{max}/τ_2) [nVs]
α	51.0 ± 0.1	10.4 ± 0.1	4.8 ± 0.1	16.0 ± 0.1	1133 ± 4	84.6 ± 0.5	14.8 ± 0.3
μ	66.6 ± 0.8	144.4 ± 0.7	7.9 ± 0.6	15.7 ± 0.3	1132 ± 8	180 ± 20	204 ± 2
β	6.9 ± 0.1	15.9 ± 0.1	0.9 ± 0.1	14.7 ± 0.2	1214 ± 8	133 ± 8	20.9 ± 0.4

Table 5.1: Result parameters of fit of the average pulses above with Eq. 4.5 (3 decay exponential).

The time distribution of the average pulses for the different topologies fitted with Eq. 4.5 are shown in Fig. 5.11. The distributions were superimposed and normalized to a unitary peak value in order to emphasize the different topologies. The average pulse distributions of electrons and cosmic muons are overlapped while the $\alpha-$particles distribution is characterized by the lower fraction of light coming from the slow component.

The relative intensities of the components can be calculated as defined in Eq. 4.10. For $\alpha-$particles (green) the light from the triplet state decay represents only 21% of the total scintillation light while the prompt light is dominant (72%); the remaining 7% is identified and modeled as the intermediate component. The situation is opposite for muons and electrons (red and blue) were the fast and slow component represent respectively 24% and 73% of the total light; the influence of the intermediate component on the total light is now only 3%. The relative instensity coefficients will therefore be:

$$p^{\alpha}_{\text{fast}} = 0.72, \quad p^{\alpha}_{\text{slow}} = 0.21 \quad \text{and} \quad p^{\alpha}_{\text{int}} = 0.07 \quad \text{for } \alpha-\text{particles;} \tag{5.12}$$

$$p^{e^-}_{\text{fast}} = 0.24, \quad p^{e^-}_{\text{slow}} = 0.73 \quad \text{and} \quad p^{e^-}_{\text{int}} = 0.04 \quad \text{for } e^- \text{ and muons.} \tag{5.13}$$

5.5 Calibration with ^{210}Po $\alpha-$particle spectrum

The light yield of the detector is calculated as the ratio of the collected light to the deposited energy in the detector. The $f_l = 0.724$ and $f_n = 0.98$ coefficients defined in Section 2.3 have been taken in account. The radioactive source has been made by dipping a small tin ball, which was deposited on a 200 μm diameter stainless steel wire, in a ^{210}Pb radioactive solution. The tin ball had a diameter of $\simeq 500 \pm 100$ μm, for this reason the $\alpha-$particles emitted under the surface have lower energies producing an exponential tail in the $\alpha-$spectrum.

5.5.1 Effects of the source dimensions

A possible approach to include the effects of the tail of the α-particle distribution is to fit the IPH with a gaussian convoluted with a truncated exponential function (as suggested in [93]):

$$\begin{aligned} f(L) &= e^{-\frac{(L-L_\alpha)^2}{2\sigma^2}} \otimes \left[H\left(L_\alpha - L\right) \cdot \left(\frac{K}{a} \cdot e^{-\frac{L_\alpha - L}{a}} \right) \right] = \\ &= \frac{K}{2a} \cdot e^{\frac{\sigma^2}{2a^2}} \cdot e^{\frac{L-L_\alpha}{a}} \left[1 - \mathrm{Erf}\left(\frac{\sqrt{2}}{2} \left(\frac{L - L_\alpha}{\sigma} + \frac{\sigma}{a} \right) \right) \right], \end{aligned} \tag{5.14}$$

where L_α is the light for the nominal $\alpha-$particle energy, $H(L_\alpha - L)$ is a step function which truncates the exponential for $(L > L_\alpha)$, σ is the width of the gaussian, a is the attenuation length of the exponential tail and K is a normalization constant.

The most probable value of the distribution does not correspond to the light generated by the 5.3 MeV $\alpha-$particles because the convolution with the exponential function shifts it to lower values with respect to L_α. An $\alpha-$particle sub-sample (selected as in Section 5.4) can be used directly for energy calibration of the detector. The IPH spectrum of the selected sub-sample is shown in Fig. 5.12 (green) together with the IPH of the uncut data set (black line). The IPH spectrum was fitted with Eq. 5.14 in a range between 3000 to 10000

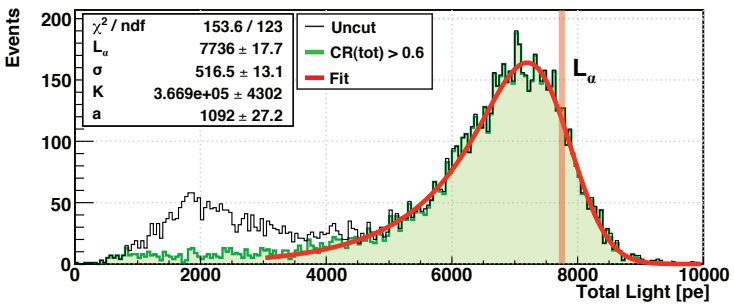

Figure 5.12: The IPH spectrum of the selected $\alpha-$particle sub-sample fitted with Eq. 5.14 (redline). The black line represents the uncut data set.

photoelectrons. The lower threshold was determined by the trigger level ($\approx$ 500 p.e.). A light of $L_\alpha = 7736 \pm 18$ (*stat*) p.e. was measured for 5.304 MeV $\alpha-$particles from ^{210}Pb.

In addition the mean path of the 5.3 MeV $\alpha-$particles in LAr is $\simeq 60$ μm (Ref. [66]) and it is smaller than the radius of the source. A non negligible fraction of the VUV light hits the source itself from where is only partially reflected (Ref. [94]). This effect leads to (30 ± 10) % reduction of the detected VUV light which has to be taken into account introducing an absorption quenching coefficient $q_{abs} = 0.70 \pm 0.15$. The error is very large but it takes into account different factors as the non-sphericity of the source and the presence of additional oxidation layer on the source surface which could reduce systematically the energy of the emitted particles.

5.5.2 Purity quenching factor

The purity quenching factor q_p is related to the decay times of the scintillation components, as described in Section 2.3.5. The effect of the impurity level on the fast and intermediate component decay times (τ_1 and τ_3) is not significant below 10 ppm while the slow component τ_2 is still far from the asymptotic value.

The purity quenching coefficient q_p, defined in Eq. 2.18 as the ratio between the measured and the asymptotic light (at maximum purity), takes the form:

$$q_p \simeq \frac{A + B + C}{A + \frac{\tau_2^{\max}}{\tau_2} B + C} \quad \text{for impurities } < \text{ 10 ppm}, \tag{5.15}$$

where the parameters A, B and C are determined by the fit of the average pulse shape with Eq. 4.5 (3 exponential decays), τ_2 is the decay time of the slow component and $\tau_2^{\max}$ is the nominal decay time for pure LAr ($\tau_2^{\max} = 1.6 \pm 0.1$ μs). The extrapolation of the total light to the maximum purity is performed as described in Section 4.1.4 by Eq. 4.10. This method is valid only for an impurity level below 10 ppm ($\tau_2 > 0.6$ μs).

Eq. 5.15 can be simplified introducing the relative intensities defined in Eq. 4.10:

$$q_p(\tau_2) = p_{\text{fast}} + p_{\text{slow}} \frac{\tau_2}{\tau_2^{\max}} + p_{\text{int}} \tag{5.16}$$

The relative intensities p_{fast}, p_{slow} and p_{int} do not depend on the measured luminescence but only on the impinging particle type. It is therefore convenient to calculate two empirical q_p formulas can be defined using the measurements described in Section 5.4:

$$q_p(\tau_2) = \begin{cases} 0.79 + (1.31 \cdot 10^{-4})\tau_2 & \text{for } \alpha-\text{particle and nuclear recoils;} \\ 0.27 + (4.56 \cdot 10^{-4})\tau_2 & \text{for } e^-,\ \gamma\text{s and } \mu\text{s.} \end{cases} \tag{5.17}$$

5.5.3 Results

The measured light yield of the setup can be finally obtained by a simple equation which takes into account the different quenching coefficients:

$$LY = \frac{L_\alpha}{E_\alpha \cdot q_f \cdot q_p(\tau_2)} = 3.11 \pm 0.10 \text{ (stat)} \pm 0.67 \text{ (syst) p.e./keV}_{\text{ee}} \tag{5.18}$$

The luminescence quenching coefficient for $\alpha-$particles $q_f = 0.71$ has been calculated in Section 2.3 which the purity coefficient $q_p(\tau_2)$ has been taken from Eq. 5.17.

5.6 Comparison of the different reflectors

The TTX reflectors coated with different TPB surface densities described in Section 5.1.2 were tested in LAr. When the photomultipliers were cooled down their gain started to decrease until the dynodes reached a thermal equilibrium with the LAr as explained in Section 5.2. The maximum gain which could be achieved with the setup was not sufficient to perform the single photon calibration without using an additional signal amplifier (x10). The amplifier on the other hand was not needed for the measurement of the signal of $\alpha-$particles. The charge corresponding to the $\alpha-$particle peak of both PMTs was monitored as a function of time and the PMTs were calibrated after few hours when the asymptotic values were reached. This approach allows the simultaneous measurement of the purity of the LAr and of the drift of the gain.

As can be seen from Fig. 5.13 (left) the curves reach an asymptotic values after about 2 hours from the moment of powering of the PMTs (3 hours from the filling start). Before and after the last measurement session (iii) the two calibration constants of the photomultipliers were measured using the LED. Tab. 5.2 shows the results of this analysis

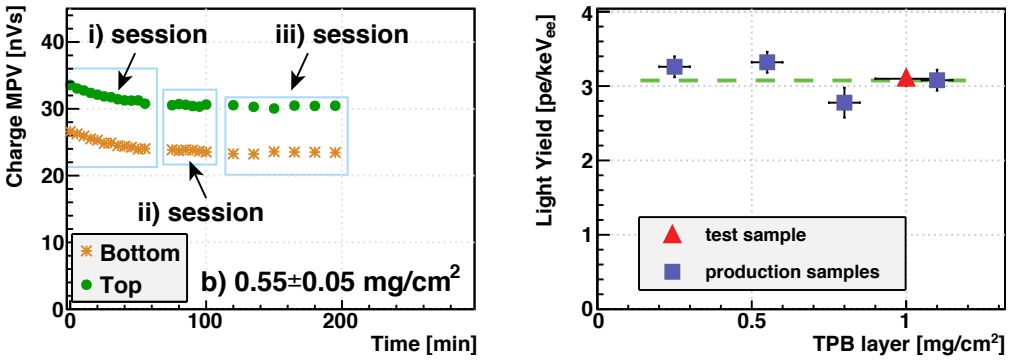

Figure 5.13: Left: Example of the drift of the $\alpha-$peak with time caused by the gain drift of the PMTs for the reflector **b** ($\rho_{TPB} = 0.55 \pm 0.05$ mg/cm^2). **Right:** Light yields for the $\alpha-$average pulse shapes of the different reflectors as a function of the TPB surface coating.

Meas.	Time after cooling	Reflector - a (0.25 ± 0.05 mg/cm^2)	Reflector - b (0.55 ± 0.05 mg/cm^2)	Reflector - c (0.80 ± 0.05 mg/cm^2)	Reflector - d (1.10 ± 0.05 mg/cm^2)
i	≈ 1 h	gains drifting	gains drifting	gains drifting	gains drifting
ii	≈ 2 h	gains drifting	gains stable	gains drifting	corrupted
iii	≈ 3 h	gains stable	gains stable	gains stable	gains stable

Table 5.2: Data summary of the data taking and PMT gain conditions for different reflectors.

for all reflector sets. The comparison of the different reflector thicknesses was done using only the last measurement sessions (iii) for each of the 4 reflectors. The *virtual channel* was calculated and the $\alpha-$particles were selected accordingly to the method explained in Section 5.4. The average pulses were calculated and fitted as explained in Section 5.5. The light yields of the detector were extrapolated to the maximal purity and listed in Tab. 5.3 toghether with the fit results. The summary of the extrapolated light yields is plotted in Fig. 5.13 (right) as a function of the TPB thickness (■). The light yield of the test samples used for the measurement of Section 5.5 has been included in the plot (▲). The green line represents the average of the 5 measurements ($LY_{\text{Cell}'07}$).

TPB	Fit Parameters						Light
Thickness	A	B	C	τ_1	τ_2	τ_3	Yield
[mg/cm^2]	[nVs]	[nVs]	[nVs]	[ns]	[ns]	[ns]	[p.e./keV$_{\text{ee}}$]
0.25 ± 0.05	59.3 ± 0.1	11.0 ± 0.1	4.2 ± 0.1	16.7 ± 0.1	1170 ± 12	57.8 ± 0.5	3.26 ± 0.14
0.55 ± 0.05	57.3 ± 0.1	13.7 ± 0.1	5.0 ± 0.1	17.6 ± 0.1	1236 ± 10	57.7 ± 0.5	3.31 ± 0.14
0.8 ± 0.05	47.4 ± 0.1	6.2 ± 0.1	3.2 ± 0.1	16.3 ± 0.1	872 ± 14	56.8 ± 0.5	2.78 ± 0.20
1.10 ± 0.05	48.8 ± 0.1	10.7 ± 0.1	4.7 ± 0.1	17.3 ± 0.1	979 ± 8	56.8 ± 0.3	3.08 ± 0.14

Table 5.3: Fit parameters and light yields for the different reflectors. Only the statistical uncertainty is reported.

No significant dependency of the light yield on the TPB thickness was found for the measured samples. The resulting data points were combined:

$$LY_{\text{Cell }'07} = 3.10 \pm 0.08 \text{ (stat)} \pm 0.66 \text{ (sys) p.e./keV}_{\text{ee}} \tag{5.19}$$

The measurement is affected by a large systematic error which depends on the effects of the source dimensions and on the effective energy which might be reduced by an eventual oxidation layer on the surface of the source.

Conclusions

In this chapter the measuring methods and the algorithms needed for particle identification in LAr were introduced. The Cell'07 detector, built using two cryogenic Hamamatsu R6237-01 mod PMTs, was characterized and calibrated with a ^{210}Pb radioactive source. The relative intensities of the three scintillation components were measured for different particle types and the results are shown in Tab. 5.4. These results were obtained extrapolating the slow component to the maximum decay time.

particle type	singlet (fast)	triplet (slow)	intermediate
α	72%	21%	7%
β/μ	24%	73%	3%

Table 5.4: Relative intensities of the three scintillation components for different particle types in LAr.

The light yield was measured for different WLS coating thicknesses. Evaporation of TPB on the Tetratex reflectors was performed using the large evaporator constructed for the coating of the reflectors of the ArDM experiment. No significant dependency of the light yield on the TPB thickness was found (range: from 0.25 to 1.1 mg/cm^2). The average light yield is $LY_{\mathrm{Cell'07}} = 3.10 \pm 0.08$ (stat) $\pm$ 0.66 (sys) p.e./keV$_{\mathrm{ee}}$

The systematic error for the absolute measurement of the light is large but cancels out for the comparison of the different reflectors samples. The $\alpha-$particles are not ideal candidates to perform an energy calibration due to source geometry effects and badly known quenching factors.

Chapter 6

Measurement of nuclear recoils in liquid argon

In this chapter I focus on the detection and the analysis of nuclear recoils in LAr using the R&D detector. New high gain cryogenic PMTs were employed to improve the signal-to-noise ratio and the resolution of single photons in the tail of the light distribution with respect to the Cell '07 detector. The procedure of LAr filling was also improved by the construction of an automatic LAr refilling system. The detector was used to measure argon nuclear recoils produced by neutrons.

6.1 Experimental setup - Cell '08

The Cell '08 detector, shown in Fig. 6.1, is similar to the Cell '07 described in Chapter 5. The PMTs were replaced with two Hamamatsu R6091-01 mod tubes. The R6091 PMT has 12 dynodes, a high gain (up to $5 \cdot 10^7$) and a remarkably small time spread ($t_s \sim 2.4$ ns). For this reason it is optimal for the measurement of τ_1. The photocathode is bialkali and has a Pt underlay. The PMT windows were coated with a TPB/Paraloid mixture dissolved in chloroform (mixing ratio 1:1). The active volume was reduced due to the

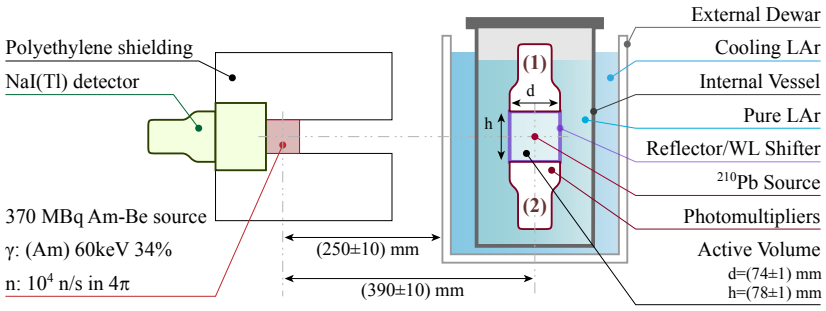

Figure 6.1: Schema of the Cell'08 detector and configuration of the AmBe radioactive source.

larger dimensions of the new PMTs (longer dynode chain).

A WLS coated reflector made of Tyvek[1] was covering the internal side walls of an aluminum cylinder (78 ± 1 mm height and 74 ± 1 mm diameter) which was inserted between the PMTs and delimited the active volume. TPB was evaporated on the reflector with a surface density of 1.0 ± 0.1 mg/cm^2. A blue LED ($\lambda_{peak} = 390$ nm) was installed in the inner vessel for gain calibration. The LED was coupled to a silicon optical fiber which transported the light into the active volume of the detector.

The signals of the PMTs were digitized and stored for off-line analysis as described in Section 4.1.1. The trigger rate was measured with a NIM scaler. An automatic liquid argon refilling system (see Ref. [95]) kept the cooling LAr level constant during the measurement.

Two radioactive sources were employed during these tests:

- an internal 50 Bq ^{210}Pb source to perform energy calibration with the $\alpha-$particles from ^{210}Po decay (Eq. 4.1);
- an external 370 MBq AmBe source ($\sim$ 30 kBq neutrons and $\sim$ 20 kBq high energy $\gamma-$rays) .

Neutrons, measured through the detection of argon nuclear recoil events, were studied using different external source configurations, neutron and photon absorbers. The energy of the argon nuclear recoils depends on the energy of the impinging neutron and it's scattering angle. For elastic collisions the energy of the recoiling argon nuclei E_{Ar} can be written as:

$$E_{\mathrm{Ar}} = \frac{2E_n}{(A_{\mathrm{Ar}}+1)^2}\left[1 + A_{\mathrm{Ar}} - \cos^2\theta - \cos\theta\sqrt{A_{\mathrm{Ar}}^2 + \cos^2\theta - 1}\right], \tag{6.1}$$

where E_n is the energy of the impinging neutron, A_{Ar} is the argon atomic mass and θ is the scattering angle.

6.1.1 AmBe source

The ^{241}Am isotope is an α and γ emitter with E_α=5.443 MeV, 5.486 MeV and E_γ=60 keV (0.36 γ per Am-decay). The $\alpha-$particles are eventually absorbed by beryllium in the $^9\mathrm{Be}+\alpha \rightarrow {}^{12}\mathrm{C}^* + n$ reaction, producing neutrons with an energy of 2 - 10 MeV (from Ref. [96], 6×10^{-5} n per Am-decay for this source) and prompt 4.4 MeV $\gamma-$rays (4×10^{-5} γ/Am-decay) from the nuclear level transition $^{12}\mathrm{C}^* \rightarrow {}^{12}\mathrm{C} + \gamma$. The neutron production yield is very low therefore the rate is reduced to $\approx 3 \cdot 10^4$ n/s.

The neutron source was inserted in a high density poly-ethylene[2] (HDPE) shielding block with two apertures, the first to collimate the neutrons, the second for a NaI(Tl) detector which could be used to tag the γ-rays from $^{12}\mathrm{C}^*$ decay. The distance of the source from the active LAr volume was 390 ± 10 mm. For this configuration the neutron flux in the active LAr volume was 30 - 50 n/s (estimated from the solid angle).

[1] DuPont, high-density polyethylene fiber membrane

[2] Poly-ethylene $(C_2H_4)_n$

6.1.2 Overview of the measurements

Data were collected during 3 different measurement sessions (**a**, **b** and **c**):

a) only using the internal Pb source (calibration of the detector);

b) with and without the external AmBe neutron source;

c) the internal source was removed and nuclear recoil measurements were performed only with the external AmBe source. The background of the detector was studied.

The measurements of the neutron recoil spectrum from the AmBe source were taken during the last two sessions (**b** and **c**). The setup was normally triggered with the logic **OR** of the signal of the PMTs using the lowest possible threshold with the exception of a measurement taken with an external trigger on the 4.4 MeV $\gamma-$rays from the $^{12}C^{*}$ decay. The relative intensities of the different components were also measured using the method described in Section 5.4.

Different values of threshold and ADC range for each PMT were chosen to compensate the gain difference of the two PMTs. In addition different trigger setting were used for the measurement of nuclear recoils and $\alpha-$particles.

6.1.3 Calibration of the PMTs

As the new PMTs have 12 dynodes the gain drift and fluctuation became larger. Particular emphasis was placed in the study of the drift of the gain of the PMTs in order to remove possible systematic effects in the light yield studies.

The calibration constants were measured frequently during the three different measurement sessions. The LED ($\lambda_{peak} =$ 390 nm) was pulsed with a short signal ($V_{peak} \approx 1.25$ V, FWHM= 20 ns and $t_{rise/fall} = 10$ ns) and the signal was acquired synchronously; the LED junction was kept polarized to $\approx$ 700 mV to allow the prompt emission of the photons from the LED. An LED pulse can generate more than a single photon simultaneously and the probability of detecting more than one photon per pulse is not negligible. The IPH of the PMT responses to the LED pulses was fitted with the following function :

$$\begin{aligned} f_{cal}(x) &= M_0\, e^{-\frac{1}{2}(\frac{x-\mu_0}{\sigma_0})^2} + M_1\, e^{-\frac{1}{2}(\frac{x-\mu_1}{\sigma_1})^2} + \\ &+ M_2\, e^{-\frac{1}{2}(\frac{x-2\mu_1}{\sqrt{2}\ \sigma_1})^2} + M_3\, e^{-\frac{1}{2}(\frac{x-3\mu_1}{\sqrt{3}\ \sigma_1})^2}, \end{aligned} \tag{6.2}$$

which is the sum of 4 gaussian function where:

- $\mu_0,\ \sigma_0$ are the pedestal mean value in unit of nVs and its standard deviation;
- $\mu_1,\ \sigma_1$ are the calibration constant k_{PMT} (the IPH value for one photoelectron) in unit of nVs and its standard deviation;
- M_0, M_1, M_2 and M_3 are respectively the height or the background, single double and triple photons peaks.

Two typical IPH distributions for the Cell'08 PMTs are shown in Fig. 6.2 (black dots). The datapoints were fitted with Eq. 6.2 (red) which takes into account the pedestal (events in which no photons are detected) and the possibility of having more than one single photon at the time. The dashed lines correspond to the contributions of the four individual distributions of Eq. 6.2. The Fig. 6.2 (left) corresponds to the PMT on the top of the LAr detector while Fig. 6.2(right) is the PMT on the bottom. The relative height of the single, double and triple photoelectron contribution is different for the upper and lower PMT because depends on the illumination. At a gain of $3 \cdot 10^7$ the PMTs showed an excellent single photon response and the measurement of the calibration constant did not require the use of an external signal amplifier. The calibration could also be measured using the single photons in the tail of the scintillation light distributions and was used to crosscheck the calibration performed with the LED pulses.

The calibration constants (k_{ch1} and k_{ch2}) has been determined as a function of time for the three different measurement sessions, the results are shown in Fig. 6.3. Gain instabilities were observed at the power-on of the detector and between different measurement sessions even if the voltage applied at the tube was the same in three cases ($V_{PMT} = -1600$ V). The maximum gain fluctuation during a measurement session was 30% (session b).

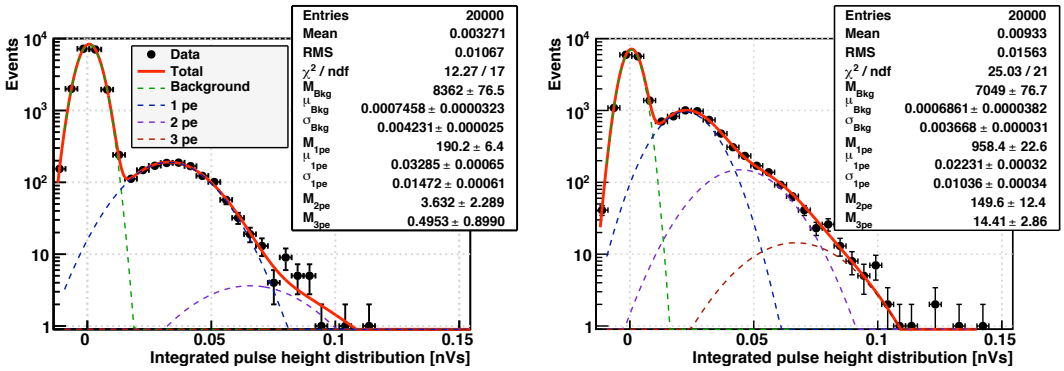

Figure 6.2: IPH distributions obtained with LED pulses for the two PMTs. The black dots are the experimental data while the red curve is the fit with Eq. 6.2. The dotted curves show the single contribution of pedestal (green), 1 p.e. (blue), 2 p.e. (violet) and 3 p.e. (red).

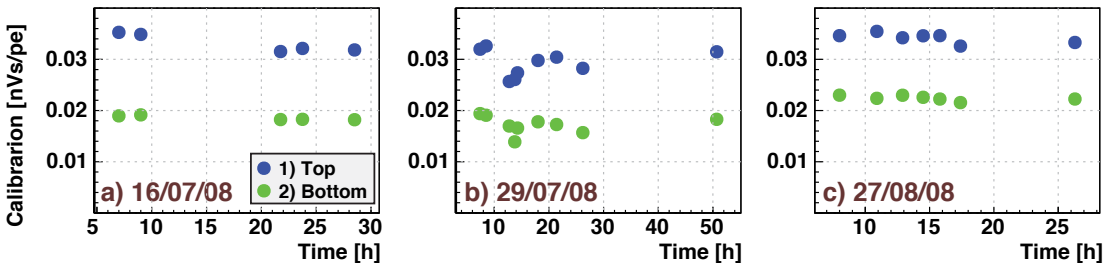

Figure 6.3: Calibration constants k_{ch1} and k_{ch2} as a function of time for the three different measurement periods.

6.1.4 Energy calibration with α-particles

The energy calibration of the setup was done with α-particles using the method described in Section 5.5. The measurements could be performed only in sessions **a** and **b** since in section **c** the internal source was removed. The light yield of the setup was obtained by fitting the IPH of the selected events with Eq. 5.14 while the information of the decay time and the population of the different states were obtained by the fit of the average pulse with a 3 exponential decay model.

This procedure was repeated for all the $\alpha-$particle data sets and the results of the fits as well as the extrapolated light yields are reported in Tab. 6.1. The six measurements were combined together to obtain a more precise value of the light yield:

$$\mathrm{LY}_{\mathrm{Cell'08}} = 3.08 \pm 0.06\ (\mathrm{stat}) \pm 0.66\ (\mathrm{syst})\ \mathrm{p.e./keV_{ee}} \tag{6.3}$$

which agrees perfectly with the value measured for the Cell'07 detector in Section 5.6 ($\mathrm{LY}_{\mathrm{Cell'07}} = 3.10 \pm 0.08$ (stat) p.e./keV$_{\mathrm{ee}}$). The level of agreement is remarkable considering that the PMTs and the reflector materials were changed and the active volume was reduced by 50%. As in Section 5.5 the effects of the source dimensions are the main source of uncertainty and are considered as a systematic error of the measurement.

	Fit Parameters						Light
Set	A	B	C	τ_1	τ_2	τ_3	Yield
	[nVs]	[nVs]	[nVs]	[ns]	[ns]	[ns]	[p.e./keV$_{\mathrm{ee}}$]
a1	92.8 ± 0.1	22.4 ± 0.1	10.1 ± 0.1	9.2 ± 0.1	1117 ± 8	57.7 ± 0.8	2.98 ± 0.20
a2	91.8 ± 0.1	19.7 ± 0.1	12.3 ± 0.1	9.4 ± 0.1	860 ± 7	47.8 ± 0.8	3.12 ± 0.14
b17	95.6 ± 0.1	24.3 ± 0.1	10.9 ± 0.1	9.2 ± 0.1	1115 ± 8	57.8 ± 0.5	3.16 ± 0.14
b19	96.4 ± 0.1	22.1 ± 0.1	10.3 ± 0.1	9.4 ± 0.1	1106 ± 8	57.7 ± 0.5	3.10 ± 0.14
b20	96.8 ± 0.1	22.3 ± 0.1	10.4 ± 0.1	9.4 ± 0.1	1113 ± 8	56.8 ± 0.5	3.10 ± 0.14
b31	92.2 ± 0.1	23.9 ± 0.1	11.0 ± 0.1	9.1 ± 0.1	1098 ± 5	56.8 ± 0.3	3.08 ± 0.14

Table 6.1: Results of the energy calibration of Cell'08 with $\alpha-$particles.

6.1.5 Decay time of the fast component

The Hamamatsu R6091-01 mod PMT has a very short time spread ($t_s \approx 2.4$ ns) and can therefore resolve the decay time of the singlet state (τ_1) more precisely. The average τ_1 measured in the Cell'08 with $\alpha-$particles is $\tau_1 = 9.28 \pm 0.13$ ns and is compatible with the values found in the literature (see Tab. 2.4).

6.2 Measuring technique

At first all the data sets were analyzed without performing any selection. Neutrons produce argon recoils whose pulse shapes are similar to the ones of $\alpha-$particles. For this reason the neutron signals (argon recoils with E_R up to 1000 keV) are expected in the tail of the $\alpha-$particle distribution.

The presence of a neutron absorber, such as the high density polyethylene (HDPE), in between the source and the detector is expected to reduce the neutron flux at the active volume. A 4 cm lead absorber (Pb) reduces instead the low and high energy photons flux. The peak of the 60 keV $\gamma-$rays from the Am decay (which is the dominant decay of the source) is used to perform an additional calibration.

A quantitative evaluation of the background, which includes the scintillation light of the internal ^{210}Pb source, was performed without the AmBe source (set **b23**). The AmBe source was then inserted in the HDPE shielding cylinder at a distance of about (390 ± 10) mm from the active volume (set **b26**). The neutron source was shielded first by a 6 cm and 11 cm thick HDPE cylinders placed in front of the AmBe source in the shielding aperture (sets **b27** and **b28** respectively). Data were also acquired using a 4 cm thick Pb absorber (set **b29**). The description of the different data sets for the measurement sessions **b** is listed in Tab. 6.2. No information on the trigger rate was available for this measuring session. For the statistical subtraction of the background a scaling factor was obtained counting the saturated $\alpha-$particles falling in the range where no signal from the Am source is expected (see Section 6.3.1).

The procedure was repeated for the session **c**. The description of the different data sets is listed in Tab. 6.3. The internal source was removed therefore the background consisted of the radio-contamination of the detector components and the environmental radioactivity. The background spectrum was measured in the set **c3**. The AmBe source was then inserted in the HDPE shielding cylinder at a distance of about (390 ± 10) mm from the active volume (**c4**). A 6 cm thick HDPE cylinders was placed in front of the AmBe source to absorbe the neutrons (**c5**) and substituted later with a 4 cm thick Pb photon absorber (**c6**). A last set was acquired moving the source about 20 cm closer to the LAr active volume (**c7**).

Set	Type	Events	Scaling	Description
b23	Background	40 k	1.0	only internal source
b26	AmBe source	80 k	0.77	
b27	AmBe source	80 k	0.57	source shielded by 6 cm of HDPE
b28	AmBe source	80 k	0.53	source shielded by 11 cm of HDPE
b29	AmBe source	80 k	0.56	source shielded by 4 cm of lead

Table 6.2: Description of sets of the first session of measurement with neutrons.

Set	Type	Events	Trigger Rate	Scaling	Description
c3	Background	40 k	190 ± 4 Hz	1.0	background
c4	AmBe source	20 k	510 ± 7 Hz	5.37	
c5	AmBe source	20 k	400 ± 6 Hz	4.21	source shielded by 6 cm of HDPE
c6	AmBe source	40 k	390 ± 6 Hz	2.05	source shielded by 4 cm of lead
c7	AmBe source	40 k	900 ± 9 Hz	4.74	source closer to the active volume

Table 6.3: Description of sets of the second session of measurement with neutrons.

6.3 Data analysis

The distributions of the component ratio (CR) as a function of the total light for session **b** are shown in Fig. 6.4. The tail of the distribution of the scintillation light from $\alpha-$particles together with the electron and muon bands are clearly visible for all the data sets and leaking in the ADC saturation region (red line).

The maximum neutron energy from the AmBe source is about 10 MeV and the nuclear recoil energies will therefore be below 1 MeV (calculated from Eq. 6.1). As explained in Section 2.3 the luminescence of nuclear recoils is be quenched by a factor $q_f = 0.27$ while purity quenching factor for nuclear recoils (defined in Eq. 5.17) is $q_p^{nr} = 0.934$ for $\tau_2 = 1.1$ μs. The light yield for nuclear recoils is then:

$$LY^{n.r.}_{\text{Cell'08}} = LY_{\text{Cell'08}} \cdot q_f \cdot q_p \simeq 0.8 \text{ p.e./keVnr} \tag{6.4}$$

using the $LY_{\text{Cell'08}}$ determined in Section 6.1.4. Given this result the neutrons are expected in the region of the IPH$\leq$ 800 p.e. and 0.5 <CR< 1.0 (dashed region).

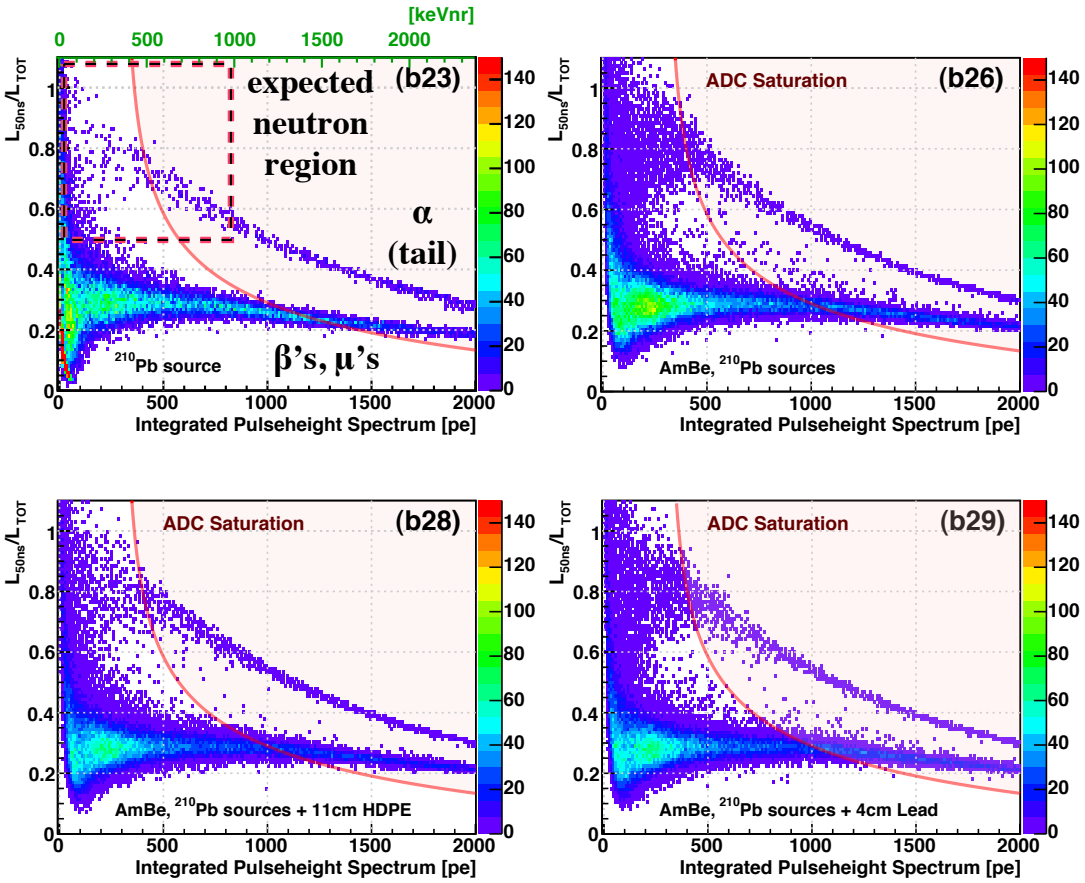

Figure 6.4: Distributions of the *Component Ratio* (CR) as a function as the integral of the detected scintillation light for the different data sets of session **b** (see text).

A strong evidence for neutron signals can be observed in the set **b26**. Events in the neutron region are reduced as expected for the sets **b27-28** since the source was shielded by 6 cm and 11 cm of HDPE respectively. In the set **b29** the $\gamma-$ray flux was strongly reduced by the 4 cm Pb absorber while the neutrons were weakly reduced. The excess of events around 200 p.e. was interpreted as the 60 keV $\gamma-$rays emission from the Am source. The measurement were repeated in session **c** after the removal of the internal ^{210}Pb source.

6.3.1 Observation of nuclear recoils in LAr

The different distributions were compared selecting the nuclear recoils in a narrower region (IPH $\leq$ 500 p.e. and 1.0 <CR< 0.6). In this way the effects of background and saturated events were reduced. The background, determined with the data sets **b23** and **c3**, was statistically subtracted. For session **b** the trigger rate was not measured. For this reason a scaling factor was determined by counting the saturated $\alpha-$particles falling in the range (0.3 < CR < 0.4) and (1500 p.e. < IPH < 1700 p.e.) where no signal from the Am source is expected.

For session **c** the distributions were scaled directly using the trigger rate which was measured with a standard NIM scaler (counter) and the number of events. The scaling factor p_j for each data-set was calculated as the ratio between the trigger rates r weighted on the number of events acquired N:

$$p_j = \frac{r_j}{N_j^{tot}} / \frac{r_{bkg}}{N_j^{bkg}}, \tag{6.5}$$

and are reported in Tab. 6.3. The IPH spectra of the different configurations are shown in Fig. 6.5 (left) and Fig. 6.5 (right) for session **b** and **c** respectively. In both cases the electron bands were leaking in the nuclear recoil region for IPH< 100 p.e. The most

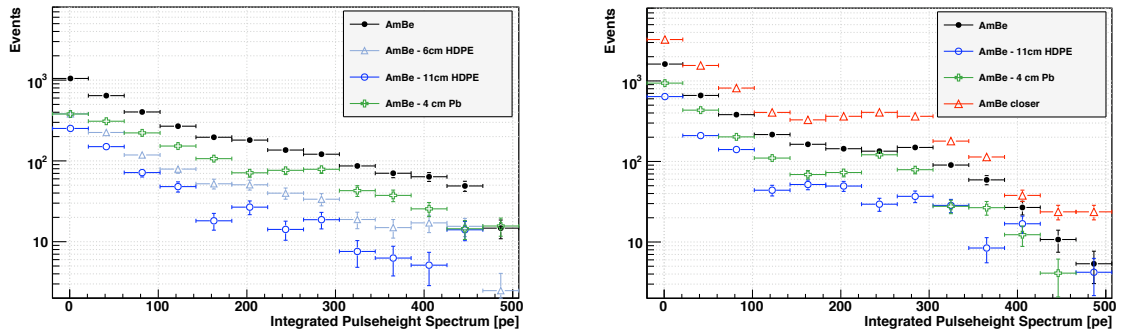

Figure 6.5: Nuclear recoil spectrum for the selected events of session **b** (left) and **c** (right). The black data points correspond to the measurmements with an AmBe source. Different radiation shields have been introduced to reduce the neutron or the $\gamma-$rays flux: 6 cm of HDPE (light blue), 11 cm of HDPE (blue) and 4 cm of lead (green). The source was moved about 20 cm closer to the active volume of the detector (red).

intense radiation from the AmBe source comes from the 60 keV $\gamma-$rays therefore a non negligible fraction of the leaking events were not nuclear recoils.

During session **b**, in case of the 6 and 11 cm thick HDPE absorber the neutron flux was reduced by 67% and 80% respectively. Also the 4 cm of lead reduced the measured nuclear recoils by about 42%. The absolute rate could not be calculated as no trigger rate information were available for this measurement.

Similar results were obtained during session **c**, the 11 cm thick HDPE absorber reduced the neutron flux was by 79% and the 4 cm of lead by 39%. Moving the source 20 cm closer to the detector the neutron recoil events increased by 140%.

	HDPE		Lead
Session	6 cm	11 cm	4 cm
b	−67%	−80%	−42%
c	n.m.	−79%	−39%

Table 6.4: Nuclear recoil rate reduction with different absorber.

6.3.2 Calibration with 60 keV $\gamma-$rays

An additional energy calibration was performed with the 60 keV $\gamma-$rays from the Am decay. The light yield LY can be calculated on the model of Eq. 5.18:

$$LY = \frac{L_\gamma}{q_p(\beta/\gamma) \cdot E_\gamma} \tag{6.6}$$

where E_γ is the energy of the $\gamma-$ray, L_γ is the $\gamma-$rays peak in the IPH and $q_p(\beta/\gamma)$ is the purity quenching factor. No nuclear quenching is taken in account.

The IPH was calculated for the data sets **b23** and **c7** rejecting all the non $\gamma-$like signals ($CR > 0.4$). The background (**b23** and **c3**) was statistically subtracted as done in Section 6.3.1. The 60 keV $\gamma-$rays peak, which is shown in Fig. 6.6, was fitted with a gaussian function plus a decaying exponential, which was used to model the background from the high energy $\gamma-$rays.

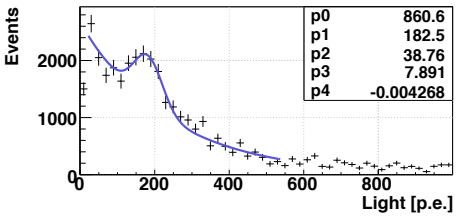

Figure 6.6: 60 keV $\gamma-$rays peak in the scintillation light spectrum of the AmBe source.

.

In the case of the data set **c7**, shown in Fig. 6.6, the IPH spectrum peaks at 182.5 ± 4.7 p.e. and the light yield is $LY = 4.0 \pm 0.2$ p.e./keV$_{ee}$. For the data set **b26** the IPH spectrum peaks at $179.9 \pm 4.$ p.e. and the light yield is $LY = 3.48 \pm 0.17$ p.e./keV$_{ee}$.

Conclusions

A two PMTs LAr detector (Cell '08) with an active volume of 0.33 ℓ has been built. The light yield (LY) was determined with 5.3 MeV $\alpha-$particles and 60 keV $\gamma-$rays to be 3.08 ± 0.06 (stat) ± 0.66 (syst) p.e./keV$_{ee}$ and 3.75 ± 0.3 (stat) p.e./keV$_{ee}$ respectively. Neutrons from a AmBe source could unambiguously be detected in the Cell '08 LAr detector.

Chapter 7

The light readout system of the ArDM experiment

In this chapter the design, the construction and the first test in GAr of light readout of the 1ton ArDM detector are described.

A light diffusion cell design, similar to the LAr detectors of Chapter 6, was adopted to obtain an uniform detection of the scintillation light. The wavelength shifting (WLS) reflectors are arranged cylindrically on the field shaper rings and the light detector (an array of 14×8" PMTs) is installed in the bottom. The PMTs are shielded with a metallic grid from the high potential of the drift-field electrode.

Tetratex was chosen as reflector material for the ArDM detector. Radio-purity and outgassing properties were checked. The WLS reflectors were produced evaporating TPB on Tetratex membranes with the evaporator chamber described in Section 5.1.1. Different PMT models were tested to chose the most suitable for the ArDM experiment. The data acquisition system (DAQ) was developed. The signals of the PMTs are digitized by 10 bit 1 GS/s ADCs and the data were store to disk for off-line analysis.

The prototype of the light readout was assembled at CERN and tested with GAr at room temperature. The prototype included the full reflector coverage and 8 PMTs with different coating. A movable ^{241}Am radioactive source was installed in the active volume of the detector. The gain curves of the PMTs and the light yield as function of the source position were measured. The prototype was then cooled down to 88 K. The stability of the PMT gains and the purity GAr were investigated.

7.1 Side reflectors

As demonstrated in Chapter 4, 5 and 6 the light conversion efficiency of evaporated TPB does not depend significantly on the reflector material above certain coating thicknesses, nevertheless the choice of the reflector material is critical from the purity point of view. The presence of the strong electric field near the light reflector demands a non electrically conductive material as substrate for the wavelength shifter.

Firstly our research was focussed on two materials: the ESR (Vikuiti Enhanced Specular Reflector foil) from 3M and the Tetratex membrane from *Donaldson Membranes*. 3M foil is a multilayer specular reflecting polymer film and is highly radio-pure. Its appearance is that of a polished metal although the material is non conducting. Tetratex is an aligned polytetrafluoroethylene (PTFE) fibrous cloth and is nearly a 100% diffuse Lambertian reflector.

The reflection coefficient of both material was measured with a Optronics OL750 spectro-radiometer in the cases of uncoated and coated material. The absolute value of the reflection coefficient was measured by comparing light collected from a sample to that produced by a calibrated NIST registered pressed PTFE sample. As can be seen from Fig. 7.1 the uncoated 3M foil has a specular reflection coefficient of almost 100% for wavelengths above 400 nm while Tetratex has better reflection properties over a wider wavelength range. These measurements and the results obtained in Section 4.3 favor the Tetratex membrane as the base of our reflectors. The thickness of the employed Tetratex is 254 μm. More details can be found in Ref. [79].

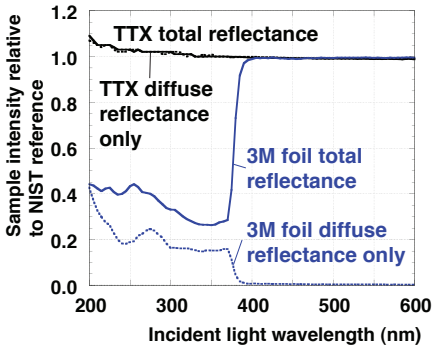

Figure 7.1: Comparison of total and diffuse reflection intensity for Tetratex and 3M foil substrates relative to the NIST reference sample (see text and Ref. [79]).

7.1.1 Vacuum properties and radio-purity of Tetratex

As all the fibrous material Tetratex membrane has an outgassing surface which is orders of magnitude bigger than the macroscopic surface of the membrane itself. The membrane could trap water from air causing long evacuation time of the detector and pollution of argon.The outgassing properties were checked in Ref. [79] with a dedicated sample of 48 g of 254 μm TTX (equivalent to 1/20 of the total amount required for the ArDM experiment reflectors). The sample was placed with in a large chamber which was evacuated. A series of measurements confirmed the good outgassing properties of Tetratex. The outgassing products were analyzed using a mass spectrometer and found to predominantly contain nitrogen and water.

In order to investigate the radio-purity of TTX, samples were sent to *Harwell Scientifics* for analysis by inductively coupled plasma mass spectroscopy (ICP-MS). The detection limits of the instrument are 0.3, 0.4 and 500 parts per billion (ppb) for U, Th and K

respectively. TTX radio-purity was found to be 1.0 ± 0.3 ppb, < 0.4 ppb and < 500 ppb for U, Th and K concentrations respectively.

7.1.2 Production and installation of the reflectors

Reproducible and reliable results were obtained with the large evaporator built for ArDM and described in Section 5.1.1. A surface density of 1 mg/cm^2 of TPB was evaporated on 15 120×25 cm^2 Tetratex reflector sheets. Each Tetratex reflector was mounted on a 3M ESR foil with the aim to optically isolate the central region of the detector from the non-active region adjacent to the dewar. The reflectors were installed on the first and last field shaper rings by means of teflon clips. Fig. 7.2 shows a partially installed light reflectors under UV light (254 nm) illumination. A slight overlap between contiguous reflectors produced a uniform surface around the active volume of the detector.

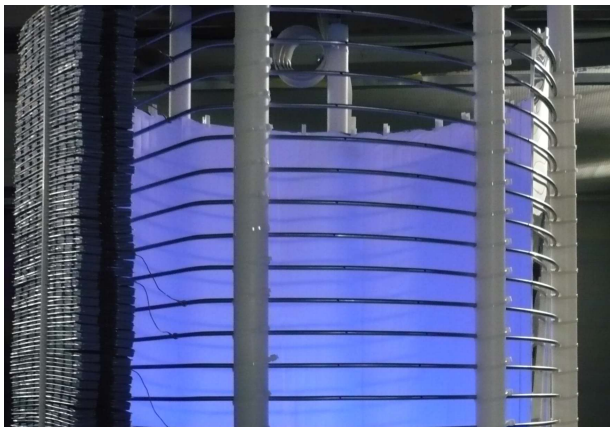

Figure 7.2: Reflectors installed in the ArDM experiment and illuminated by UV light (254 nm).

7.2 Light detector

The ArDM light readout detector consists of an array of 14 8" PMTs but for the preliminary tests only 8 PMT were installed. For the first test in gaseous and liquid argon different PMT types were installed (see Tab. 7.1). All the PMTs had a Pt underlay below the photocathode which allows the operation at cryogenic temperatures as the PMTs used for the LAr measurements described in Chapters 5 and 6. Half of the PMTs had a sandblasted glass windows. The dark count (DC) rate for the Hamamatsu PMTs[1] is about 4.7 kHz (measured at room temperature and maximum gain). Measurements in the laboratory (Ref. [80]) have shown that both the ETL-9357 and the Hamamatsu R5912's have quantum efficiencies (QE) of $\sim$20 % at cryogenic temperature ($\sim$ 88 K).

[1] test performed by Hamamatsu

Producer	Model	Dyn.	Max Gain	Q.ty	DC rate [Hz]
Hamamatsu	R5912-02 mod	14	$\approx 10^9$	5	$\sim 4.7\ 10^3$ (T=300 K)
Hamamatsu	R5912-01 mod	10	$\approx 10^7$	2	
ETL	ETL 9357-KFLB	12	$\approx 10^7$	1	

Table 7.1: Characteristics of photomultipliers tubes used in the first tests, the value in brackets correspond to the ArDM final light readout PMTs.

Despite of the differences, the three PMT types have similar volume ($\sim$ 3.7 ℓ) and weight (0.75 kg) therefore, when immersed in LAr, the buoyant force acting on each PMT is about 40 N (4 kg). The voltage divider is mounted on a 3 mm thick printed circuit board (PCB) which is soldered directly on the PMT leads and acts as mechanical support of the PMT itself. The combination of a PMT and PCB form a so called *PMT module*.

7.2.1 The 14-dynodes PMT modules

The R5912-02 mod has 14 multiplication stages and therefore can be operated at very high gain (up to 10^9). A custom voltage divider (VD) has been developed starting from the general purpose design suggested by Hamamatsu. Negative biasing has been chosen to avoid HV decoupling of the anode signal. The chosen scheme, shown in Fig. 7.3, allows single photon counting and a charge collection greater then 95% already at low supply voltages (from 1000 V). Ringing effects, typical at high gain, were avoided inserting damping resistors in series to the last 3 dynodes. To avoid the formation of ground loops a 50 Ω resistor has been placed between the ground of the HV and the one of signal.

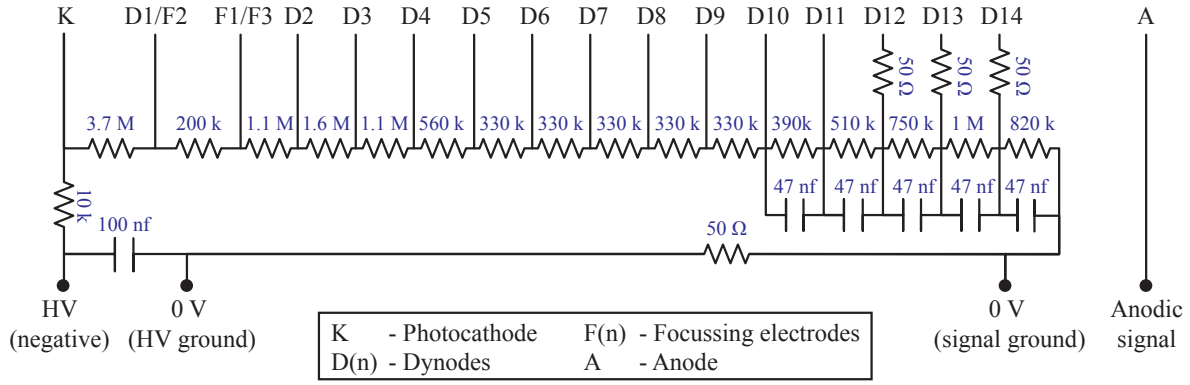

Figure 7.3: The electric schema of the cryogenic voltage divider of the 14 dynodes PMT modules.

7.2.2 The 10 and 12-dynodes PMT modules

The other three modules were equipped with different PMTs: the Hamamatsu R5912-01 mod (2 PMTs) and the ETL 9357-KFLB (1 PMT) which respectively have 10 and 12 dynodes. The R5912-01 mod is similar to the one described in Section 7.2.1 except for the maximum achievable gain (about 10^7). The voltage dividers of the 14-dynodes PMTs had to be adapted for both PMT types.

7.2.3 Coating of the PMT glass window

After all modules were tested in the laboratory a thin WLS coating was applied on the glass windows of 6 out of 8 PMTs to convert directly impinging VUV photons to a longer wavelength, matching the QE of the bialkali photocathode. The remaining two were left uncoated as a reference.

Evaporation produced the best results on the reflectors. For this reason it was decided to test this deposition method on the PMT glass window for 3 of the modules (1, 5 and 8 of Tab. 7.2). The direct VUV light is a small percentage of the light impinging on the PMTs therefore the coating should be very thin not to absorb or re-diffuse the shifted light. TPB surface density was therefore very small (0.05 mg/cm^2). Other 3 modules were coated by dipping the PMT windows in a solution of TPB and Paraloid[2] dissolved in chloroform (ratio TPB:Paraloid = 1:1) as done in Section 6.1. A detailed list of the installed PMTs is reported in Tab. 7.2. The different coating configurations can be seen in Fig. 7.4.

PMT	dyn.	window type	WLS
1	14	Sandblasted	evaporated TPB
2	14	Transparent	TPB-Paraloid
3	12	Sandblasted	no TPB
4	14	Transparent	TPB-Paraloid
5	14	Transparent	evaporated TPB
6	14	Transparent	no TPB
7	10	Sandblasted	TPB-Paraloid
8	12	Sandblasted	evaporated TPB

Table 7.2: Description of the different configuration of the installed PMTs.

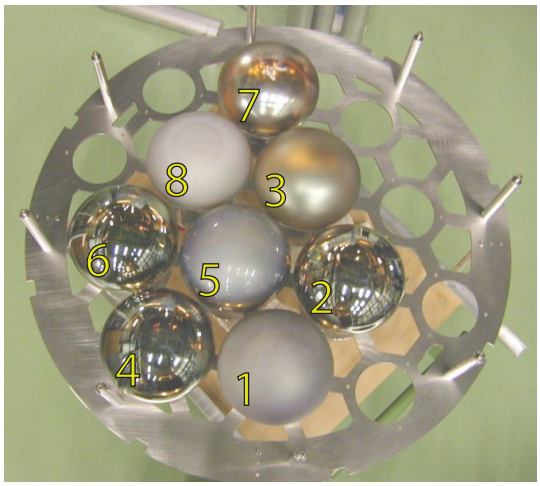

Figure 7.4: Appearance of the different PMT coating configurations (top view).

[2]Paraloid B72 is an acrylic resin.

7.2.4 PMT support structure

The PMT support structure must sustain the total buoyant force acting on the PMTs in LAr ($\sim$ 60 kg). In air the total weight of the PMT modules is only $\sim$ 10 kg. The main support was obtained by a 5 mm thick stainless steel disk. The disk was properly carved to minimize the amount of material in the in the detector without affecting the stiffness of the structure.

The PMT array has a hexagonal-cell (honeycomb) structure. The assembled light detector can seen in Fig. 7.5. The modules fixed to the PCB support rings mounted below the main structure. High density polyethylene (HDPE) collars were positioned between the PMT and the main support such that each PMT is kept in the horizontal position, at the right distance from the other PMTs.

Strong electric field near the photocathode can reduce the collection efficiency of the PMTs. For this reason an electric shield grid (E-Shield) was mounted 5 cm from the PMT surfaces. The E-Shield and the PMT support structure can be polarized accordingly to the PMT photocathode potential to further reduce the effects of non-zero electric field near the photocathodes.

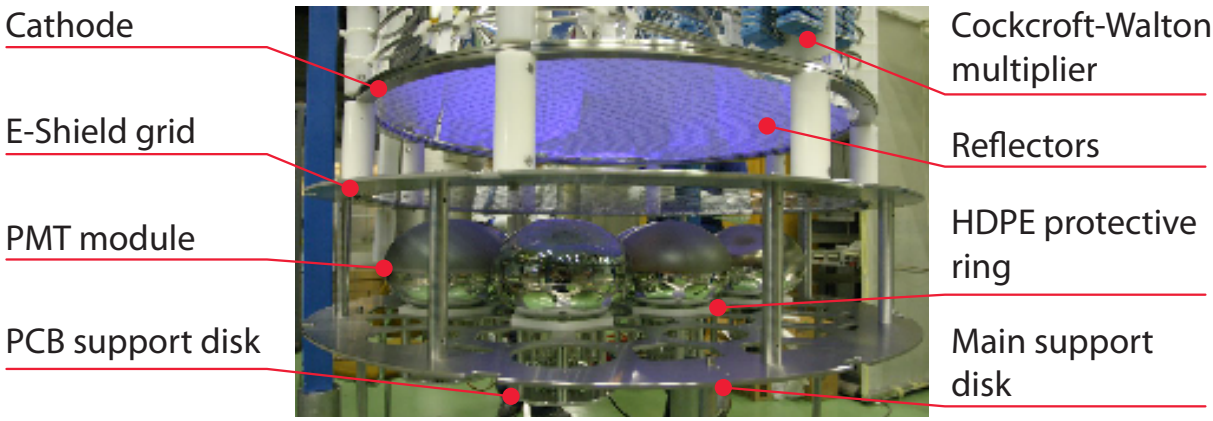

Figure 7.5: Test PMTs are assembled in the support structure.

7.2.5 Electrical connections

Special micro-coaxial cables, developed for the ATLAS LAr calorimeter (Ref. [97]), were employed for signal and high voltages. The inner conductor is a single wire of 200 μm diameter while the external diameter is 1.2 mm, with a braided outer conductor, made of 63 μm diameter wires. The cable has an impedance of 50 Ω.

On the flange side the cables were directly fitted in the flange and soldered on the BNC and SHV connectors while *Lemo 00* connectors were used for the connection on the PCB. The outer connector (shield) of each cable was kept isolated from the ground of the detector to reduce possible ground loops.

7.3 Data acquisition

The output signals of each of the photomultipliers is sent to an analog fan-in/fan-out (CAEN V925) which reproduces the input signal on all its output. This unit will be replaced by simple passive splitters for the final detector. The *threshold discriminator* (CAEN V814) provides the discrimination of the analog signals using user definable threshold values in the range between 4 and 200 mV (typical single photon pulse height is $V_{pe} \sim 15$ mV for a gain of $2 \cdot 10^7$).

The V814 generates a digital pulse when the signals from n or more photomultipliers were simultaneously over the defined threshold voltage. This signal (also called *Multiplicity* or *Majority*) is used to trigger the DAQ. The digitization is performed by four cPCI boards (Acqiris DC 282) each equipped with 4 fast sampling 10 bits ADC channels (up to 2 GS/sec) and 128 MB of memory. The DAQ can be triggered by internal or external trigger signals.

The PMT gain calibrations were obtained by pulsing a LED ($\lambda_{peak} = 390$ nm) with a Agilent arbitrary waveform generator (AWG) and the DAQ was triggered synchronously with the LED pulse (as explained in Section 4.2.2). The external trigger was used also for the measurement with external sources (i.e. ^{22}Na source, see Chapter 8) which required specific trigger patterns in combination with other detectors.

The trigger rates of the individual channels as well as the majority signal were measured with a digital scaler (CAEN V560). The data were stored on disk and analyzed off-line. The PMT supply voltages were generated by a CAEN SY2527 system which was controlled by the DAQ system. An schema of the trigger and of the DAQ is shown in Fig. 7.6.

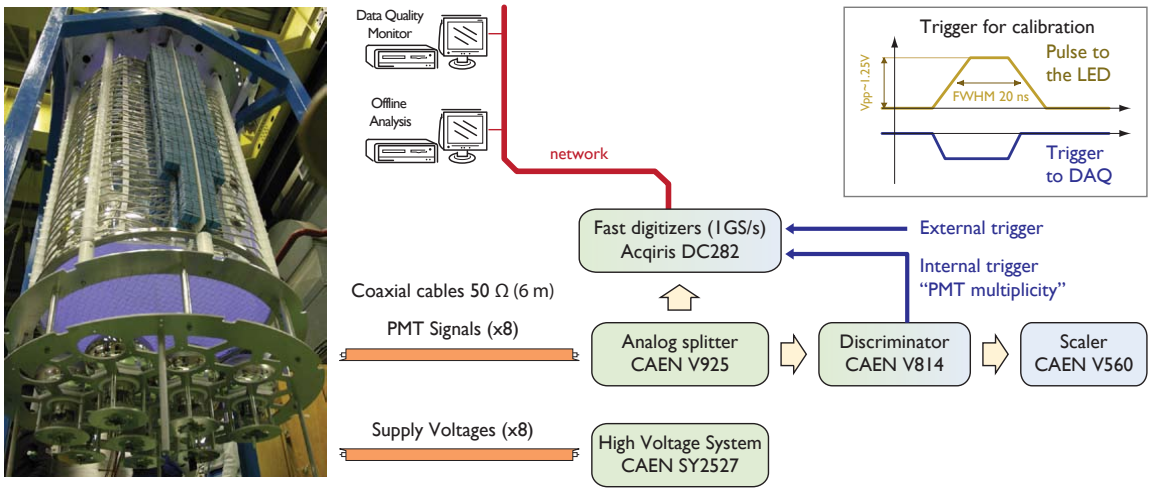

Figure 7.6: Schema of the DAQ system for the test of the light readout.

7.4 First test of the light readout with GAr

7.4.1 Movable ^{241}Am source for the measurement in GAr

A 40 kBq ^{241}Am source (5.4 MeV $\alpha-$particle and 60 keV $\gamma-$rays) was installed on a movable actuator positioned in the center of the top flange of the detector as shown in Fig. 7.7. The source could be moved in the active volume from +30 to −30 cm from the center of the detector. In November 2008 the source was lowered by 10 cm to allow measurement closer to the PMT surface. For each series of measurement 10 - 20 k events were acquired for 7 different source positions interleaved by 10 cm.

The Am emitter foil was protected by a thin layer of evaporated Pd (Palladium) reducing the energy of $\alpha-$particles by approximately 1 MeV. An optical fiber was tied to the side of the source and coupled to a blue/UV LED (λ_{peak} = 390 nm) on the other end. A second blue/UV LED was mounted shining on the top flange such to have diffused light in the detector. Both LEDs were used for calibration.

7.4.2 Measurement in GAr at room temperature

Before every measurement session the apparatus was evacuated down to about $5{\cdot}10^{-6}$ mbar. GAr (Ar 60) was flown in the detector at a rate of about 20 ℓ/m until an internal pres-

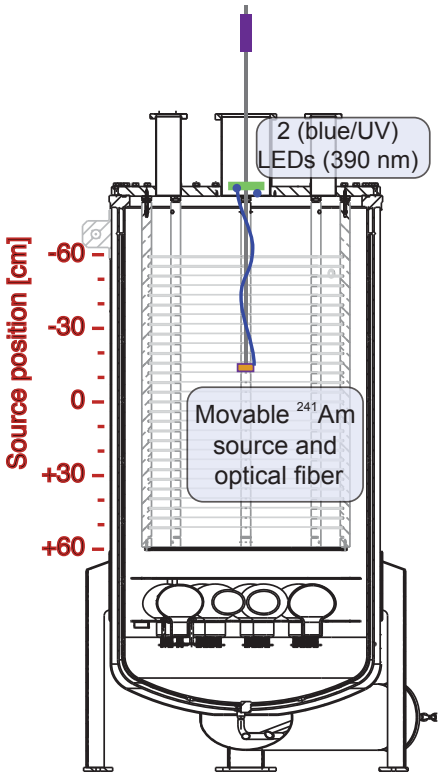

Figure 7.7: ^{241}Am source position in the ArDM detector.

sure of 1.1 bar was reached. The PMTs were turned on at voltage of about −1000 V which corresponded to a gain of about $2 \cdot 10^7$. Each PMT was studied individually and the $\alpha-$particles from the ^{241}Am source were selected and analyzed using the method described in Chapter 4.1.2.

7.4.2.1 Gain curve of the PMTs

The gain curves of the PMTs were measured to determine the optimal working point of the PMT modules prior to the GAr measurements. The calibration constants were measured at different voltages using the LED method (Section 4.2.2). At voltages above $\simeq -1150$ V sparking occurred on most of the VDs, for this reason the calibrations were performed in vacuum. The data were fitted with:

$$G = A \cdot V^{kn}, \tag{7.1}$$

from Ref. [92], where A and k are constants which depends on the dynode structure and n is the number of dynodes. The knowledge of the two parameters of Eq. 7.1 is necessary to equalize the gain of all the PMTs. The measured gain curves of the PMTs as a function of the supply voltage are shown in Fig. 7.8. The data points were fitted with Eq. 7.1.

For the test in GAr I chose the lowest voltages which allowed a precise calibration of the PMTs ($G > 10^7$), which are:

- −1000 V for the PMTs with 14 dynodes;
- −1120 V for the PMTs with 10 dynodes;
- −1300 V for the ETL PMT.

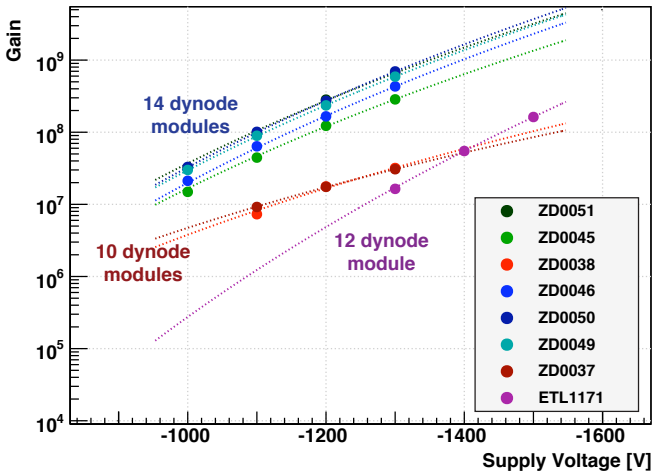

Figure 7.8: Calibration curve of the PMTs in GAr ($T = 300$ K) in the ArDM detector. The lines represent the fit of the data point with Eq. 7.1.

Lower voltages are desired to reduce the heat dissipation of the VDs in LAr (since $P = V^2/R$). The ETL module was never used in GAr as sparking occurred before a reasonable gain was obtained(10^7 or higher).

7.4.2.2 Light yield as a function of the source position

Light yield of $\alpha-$particles was measured as a function of the Am source position. The source was moved from -30 cm to $+30$ cm with 10 cm steps with respect to the detector center. At each position 20 k events were acquired. Seven series of measurement in GAr were performed. Module 7 and 8 (Hamamatsu 10 dynodes and ETL) were not used for this measurement because the occasional sparks in the VDs were producing an excessive amount of light therefore causing instabilities in the rest of the PMTs.

The DAQ was triggered requiring at least 4 PMTs with a signal over threshold (Majority 4). The threshold of the discriminator were $V_{th} = 5$ mV and 10 mV for the 10 and 14-dynodes PMTs respectively (about 1 p.e.). These settings corresponded to global trigger requirement of at least 4 p.e. detected in the fast component.

Each PMT was studied individually. The signal of the $\alpha-$particles from the ^{241}Am source was selected and analyzed using the method described in Chapter 4.1.2. The lifetime of the slow component was measured fitting the average pulse of selected events with a sum of 2 decaying exponential (Eq. 4.4) rejecting the intermediate region.

The purity was degrading rapidly after filling therefore the light yield was extrapolated at the maximum measured purity ($\tau_2 = 3.2$ μs). This effect was evaluated by observing the evolution of τ_2 which was decreasing with a rate of 200 - 400 ns/hour.

An example of the analysis is shown in Fig. 7.9 where the total collected light of the PMTs (extrapolated at $\tau_2 = 3.2$ μs) is plotted as a function of the source position. All the measurement series were characterized by the same behavior which can be explained without the necessity of a Monte Carlo.

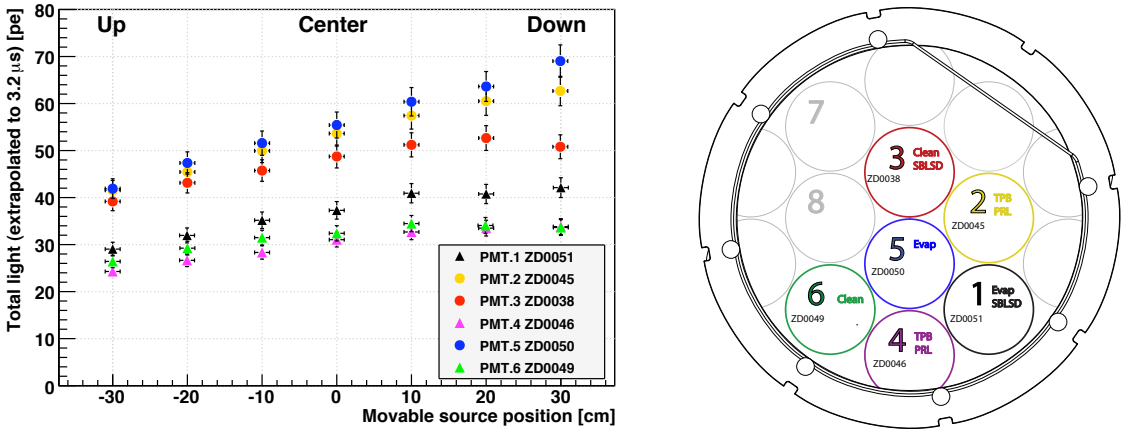

Figure 7.9: Left: Collected light as a function of source position (**S7**). PMT 7 and 8 were not used because of sparking of the VD (see text). **Right:** Position and configuration of the PMTs (top view).

PMTs 2, 3 and 5 (yellow, red and blue dots respectively) are in the center of the detector just below the ^{241}Am source and receive more light than the others. When the source is in position −30 cm the PMTs detect approximately the same amount of light most of which has been converted on the WLS reflector and is therefore diffuse. The contribution of the direct light starts to be significant when the source is moved toward the PMTs. The light detected by PMT 3 (red) has a turning point and starts to decrease when the source is in pos. +20 cm because the module is not coated with WLS and therefore not sensitive to the direct light. The light collected by the other two PMTs keeps increasing.

PMTs 1, 4 and 6 (black, violet and green respectively) are on the side and detect less light. The light collected when the source is in position −30 cm is small and rise slowly as the source is moved toward the PMTs. PMT 1 (black), which is coated by evaporated TPB, detects more light than the other two for every source position. The errors on the y-axis include the calibration error and the extrapolation uncertainty.

The shape of the distribution is in agreement with Monte Carlo studies (Ref. [98]) however the absolute value of detected photon is not yet explained by the simulation which at present does not include the non 128 nm component of the scintillation light in GAr. The light yield curves are all compatible within the errors. No deterioration of the light yield has been measured.

7.4.3 Measurement in cold GAr ($T = 88$ K); first cool down

Measurements in GAr at $T = 88$ K have been performed cooling down and filling the detector with pure GAr. The aim of the measurement was to study the response of the PMTs and the achievable purity at cryogenic temperature. No simulations have been performed for this configuration. Two PMTs (PMT 7 and 8) were unstable. Their VDs were sparking in GAr at supply voltages lower than −850 V. The light generated in the sparks caused instability on the other PMTs therefore they were switched off and excluded from the analysis.

The apparatus was evacuated down to 10^{-6} mbar. The side walls of the internal vessel were cooled by filling the dimple jacked with LAr. The temperature along the vertical direction of the detector was monitored by 9 temperature sensors[3]. The uppermost sensor (Sensor 0) was at the level of the last field shaper while the lowermost (Sensor 9) was at about 10 cm from the PMT surface.

For the following two days the temperature inside of the detector was slowly decreasing due to a small thermal contact between the side walls and the detector components (see Fig. 7.10). The setup was pumped for about 48 hrs until the pressure in the internal vessel reached a minimum value of about $5 \cdot 10^{-8}$ mbar.

At this point pure GAr was slowly flown in the detector at a rate of about 10 ℓ/m until an internal pressure of 0.4 bar was reached. The PMTs were then turned on at a gain of about $2 \cdot 10^7$. The cooling capacity was increased by the presence of GAr. The measurement session could start when the lower part of the setup reached a stable

[3]Pt1000 Platinum resistance temperature sensors.

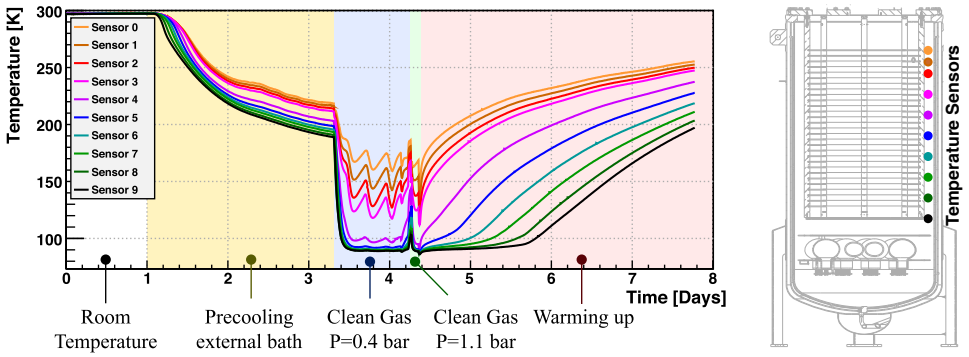

Figure 7.10: Temperature along the vertical position for the first cooldown of the detector (May 2008). Sensors are numbered from from top to bottom. The first sensor is at the level of the first field shaper (top) and the last one at the level of the cathode (bottom).

temperature of $T = 88$ K in less than 8 hrs. Pure GAr was added in the detector and more measurements were performed at a pressure of 1.1 bar.

The periodic oscillation of the temperature, which is well visible in the first 4 sensors, was caused by the automatic LAr refill system which was compensating the evaporation of the LAr in the external dimple jacket bath when the level was falling below a certain threshold.

During this first cool-down two series of measurement were acquired **S9** and **S10** respectively with a argon pressure of 0.4 and 1.1 bar. The measurement were performed about 10 hours after the PMTs were turned on. The gains of the PMTs were determined with the LED method (Section 6.1.3) before and after each measurement series. In addition the gain could be extracted from the single photons in the tail of the GAr scintillation distribution.

The purity conditions of the setup were good and the measured decay time of the slow component for $P = 0.4$ bar was $\tau_2 = 2.8 \pm 0.1$ μs. After filling the detector with more GAr up to a pressure of $P = 1.1$ bar the decay time of the slow component was again measured achieving $\tau_2 = 3.7 \pm 0.1$ μs. This value of τ_2 was higher than any value which could be found in the literature. The measurements were repeated several times with the same result.

As described in Section 2.3.5 the decay times of the scintillation light in gaseous and liquid argon depends strongly on the content of impurities. The cold wall (88 K) of the detector is in fact acting as a cold trap for impurities such as H_2O and O_2. The measurement done in GAr at $T = -20°C$ with the 5 ℓ detector (see Section 4.1) support this hypothesis.

Another possible explanation of this his effect might be found in the appearance of recombination light[4] as suggested in Ref. [99]. The recombination light has a longer production time and might affect the determination of the decay time of the slow compo-

[4]The contribution from the recombination to the scintillation light are negligible in GAr at STP.

nent for at higher GAr densities. This explanation can be verified by adding an external electric field which prohibits light from recombination by drifting apart the electron/ion pairs. A reduction of the decay time as a function of the applied field would result in the validity of the hypothesis.

7.4.4 Second cool-down

More series (**S12-18**) where acquired during the second cool-down of the ArDM detector at the pressure of 0.9 bar. The purity of argon and the long term stability of the PMT gain were studied for about 72 hrs acquiring data regularly with the source in the lower position. The voltage divider of PMT 3 was sparking for supply voltages below −850 V but the problem disappeared after 10 hrs and was regularly used for the measurements. The gains of the PMTs were stable and reached an asymptotic value after about 15 hours from the beginning of the PMT operations as can be seen in Fig. 7.11 (top).

As happened during the first cool-down the purity condition of the setup was very good and the decay time of the slow component appeared immediately long. Surprisingly the measured decay time of the slow component was $\tau_2 = 4.8 \pm 0.1$ μs. Moreover the decay time of the slow component didn't appear to deteriorate with time and was constant for more than 70 hours as shown in Fig. 7.11 (bottom). The data and the fit were checked for possible errors in the pedestal subtraction. Pile-up events were rejected by enforcing the cuts on the signal.

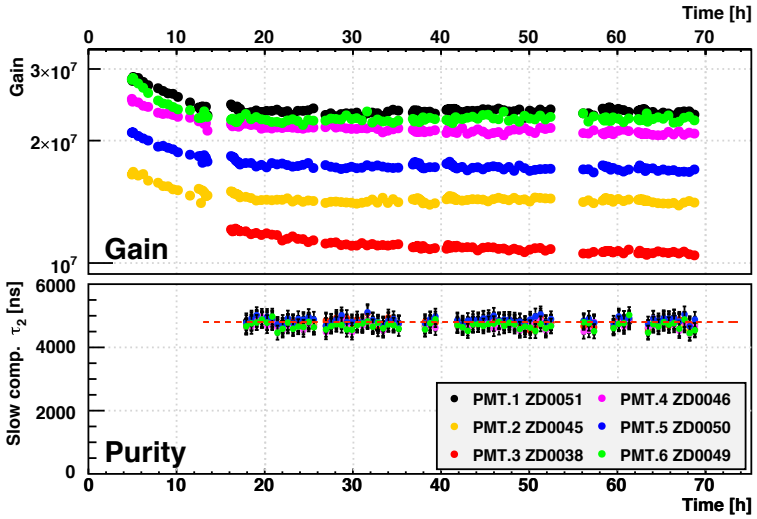

Figure 7.11: Decay time of the slow component and gain of the PMTs as a function of time for the second cool-down.

Conclusion

I designed and built the light readout system of the 1 ton ArDM experiment. The wavelength shifting reflector were produced using Tetratex as reflector material and the evaporation of WLS was performed with the methods described in Chapter 4 and 5. For the first test in GAr only 8 PMTs of different type and with different WLS coating were installed (no coating, evaporated TPB and TPB:Paraloid dissolved in chloroform).

The performance of the ArDM light readout was determined in GAr at room and cryogenic temperature (T = 300 K and 88 K). The results show the importance of having a WLS coating on the PMT despite the fact that the VUV photons impinging on their surface are only 10% of the total light detected. The difference between the two types is very small (15%) and both are good candidates for coating of the final PMT modules.

Purity of GAr deteriorates rapidly at T = 300 K while is stable for days when the detector walls are at cryogenic temperature (T = 88 K). During the second cool-down the decay of the slow component τ_2 was monitored for 72 hours. A constant value of $\tau_2 = 4.8 \pm 0.1$ μs was measured for $P_{GAr} = 0.9$ bar. This value can be justified by the fact that at 88 K the level of impurities is very low as O_2 and H_2O are frozen and trapped on the cold wall of the detector and this value could represent the real decay time of pure GAr. Another possible explanation involves the appearance of recombination effects which are normally negligible in GAr and becomes more important for higher gas densities as suggested in Ref. [99]. The validity of this hypothesis can be verified by applying an electric field which prohibits the recombination light by drifting apart the electron/ion pairs. The light yield of the detector does not show any aging effects.

Chapter 8

First measurements with a 1 ton LAr target

In this chapter I describe the first measurement with the full ArDM target, 1 ton of LAr. A good purity ($\sim$ 10 ppb) was achieved. The measured decay time of the slow component $\tau_2 = 1.54 \pm 0.01$ ns was constant for over 20 days. The light yield of the LRO was measured using external radioactive sources in different configurations.

The relative intensities of the scintillation components, measured for $\gamma-$like events, are compatible with values measured in Section 5.4. The LRO response to 511 keV $\gamma-$rays from the ^{22}Na source was measured and light distribution was compared with preliminary Monte-Carlo (MC) studies done using the GEANT4 [100] framework.

8.1 Experimental setup and measuring techniques

The apparatus, described in Chapter 7, was evacuated down to 10^{-6} mbar. The internal vessel was cooled by filling the dimple jacked with LAr while continuously pumping the detector for few days. This procedure ensures a reduced outgassing rate as the remaining impurities like water, CO_2 and O_2 have very low vapor pressure at this $T = 88$ K.

8.1.1 LAr filling

The detector was first cooled and filled with GAr similarly to what was done for the cold GAr measurement (Section 7.4.3). Cold gas was directly taken from the external argon supply dewar. The PMTs were turned on and the light yield for $\alpha-$particles was measured as a function of the Am source positions in order to reproduce the measurements done in the first two cool-downs of the detector.

After 3 days the PMTs were switched off and the LAr filling was started. The upper flange of the detector was thermally isolated (from outside) with bags filled with *perlite*[1] powder.

[1] Perlite is an amorphous volcanic glass

8.1.2 Trigger configurations

The IPH spectrum of the scintillation light was measured with different external radioactive sources which could be moved in the vertical direction along the side of the detector as shown in Fig. 8.1. The internal Am source on the movable actuator could not be used because the mean path of the $\alpha-$particles in LAr was too short to exit the housing. The scintillation light in fact was produced inside the lead shielding used to reduce the rate in GAr. The used radioactive source were:

- a 20 kBq ^{22}Na positron source emitting at the same time two collinear 511 keV $\gamma-$rays and a third 1.275 MeV $\gamma-$ray from the de-excitation of the daughter ^{22}Ne* atom;
- a 190 kBq ^{137}Cs 660 keV $\gamma-$ray source.

A trigger signal could be generated using the scintillation light produced by the ionizing particle, by an external NaI crystal in the case of the ^{22}Na source or by the combination of the two. The setup of the used trigger condition is visible is Fig. 8.2 where the colored arrows represent the $\gamma-$rays from the different sources (red for the back to back 511 keV, blue for the 1.275 MeV and green for the 660 keV). The used trigger configurations were the following:

a The data acquisition is triggered only from the scintillation light pulse (self-trigger). The thresholds of the discriminator and the PMT multiplicity were selected at the beginning of the runs;

b The ^{22}Na source is placed between the detector and a NaI crystal. We measure the 511 keV $\gamma-$rays distribution suppressing the 1.275 MeV contamination by requiring an energy of 1.78 MeV (511 keV + 1.275 MeV $\gamma-$rays) in the NaI crystal;

The evolution of the LAr purity was studied over all the acquired data independently from the trigger configuration. The relative intensities of the scintillation components was measured similarly as in Chapter 5.5. The setup was operated for about 20 days and more than 80 M of triggers were stored to disk without any background suppression. The measurement of the detector radioactive background on surface was not possible during this test because of the internal 40 kBq Am source.

8.1.3 Status of the Monte-Carlo simulation

At the present state the simulation software of the ArDM includes the complete geometry and all the physical processes such as the conversion of the VUV photons to blue, the optical effects and the quantum efficiency (QE) of the PMTs.

The conversion efficiency is known with a precision of 15% and the effects of the photon impinging angle were taken in account. The reflection coefficient of the reflector material was taken from (Ref. [79]) while the QE of the PMTs was measured from Hamamatsu (at

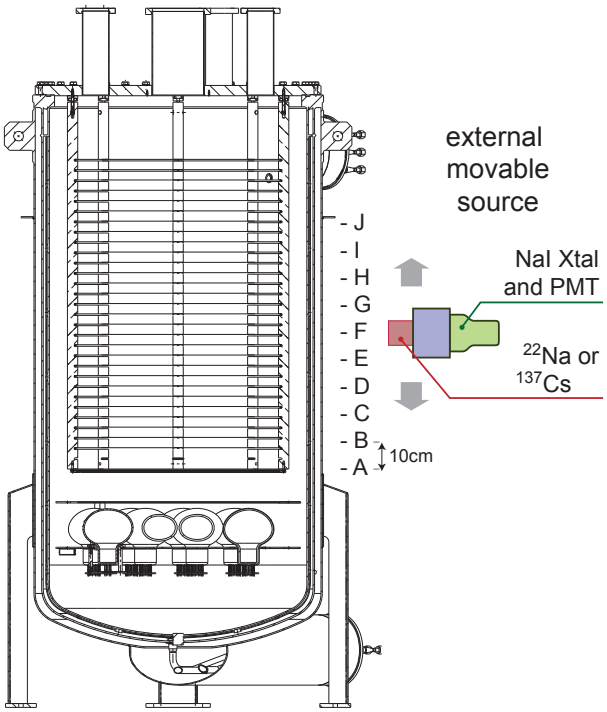

Figure 8.1: Sketch of the ArDM detector showing the different positions of the external sources.

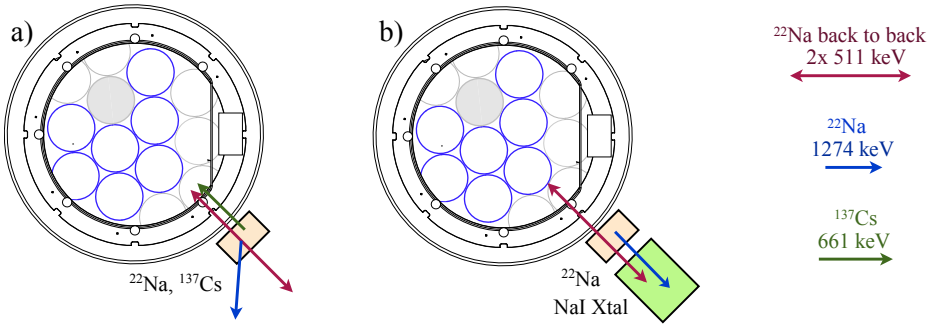

Figure 8.2: Different trigger configurations: **a)** internal trigger only; **b)** the external NaI crystal can be used with the ^{22}Na source to trigger on both the 511 and 1275 keV photons, thus eliminating the presence of the latter from the digitized samples.

room temperature). The different PMT coatings were not described. The TPB layer on the PMT glass windows was assumed to be evaporated for all the detectors.

The temporal distribution of the VUV photons (singlet, triplet and intermediate state decays) and digitization of the signal is not yet implemented. The output of the MC consists of the number of detected photo electrons detected by each PMTs. The energy deposited in the active volume of the detector and the energy of the particle entering the active volume are of course known. The Monte-Carlo (MC) software has been described in earlier works (Ref. [83, 98]).

8.2 Relative intensities of the scintillation components

The relative intensities of the scintillation components were measured with the method described in Section 5.4. A data subsample composed only of events with 0 <CR< 0.4 (electrons, $\gamma-$rays or muons) was selected. The average pulse shape of the selected events is shown in Fig. 8.3 and has been fitted with Eq. 4.5 and the results are shown in Tab. 8.1.

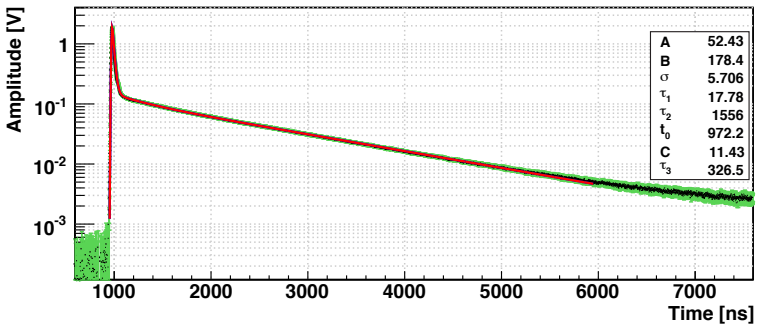

Figure 8.3: Average pulse shapes for e, γ and $\mu-$events. The distribution is fitted with Eq. 4.5 (3 exp. decays) and the result parameters are shown in the table below.

	Fit Parameters						Extrapolated
	Singlet	Triplet	Intermediate	Decay times			Triplet
Type	A [nVs]	B [nVs]	C [nVs]	τ_1 [ns]	τ_2 [ns]	τ_3 [ns]	B·(τ_2^{max}/τ_2) [nVs]
β	52.4 ± 0.2	178.4 ± 0.2	11.4 ± 0.2	17.8 ± 1.0	1556 ± 10	326 ± 10	183.4 ± 0.3

Table 8.1: Result parameters of fit of the average pulses above with Eq. 4.5 (3 exp. decays). The B parameter is then extrapolated to the maximum $\tau_2 = 1600 \pm 100$ ns (Ref. [44]).

This results are compatible with the one obtained with the Cell '07 detector. The light from the slow component is dominant (74.2%) and the prompt light represents only the 21.2% of the total scintillation light. The remaining 4.6% is composed by the intermediate component.

8.3 Measurement of τ_2

The light yield in LAr also depends on purity. The first step of my analysis was the study of the temporal evolution of the LAr purity from a measurement of the decay time of the triplet state (τ_2). As shown in the previous chapters, τ_2 does not depend on the ionizing particle. For this reason no specific particle selection needs to be performed and any set of measurement could be used for this purpose. Most of the data sets acquired

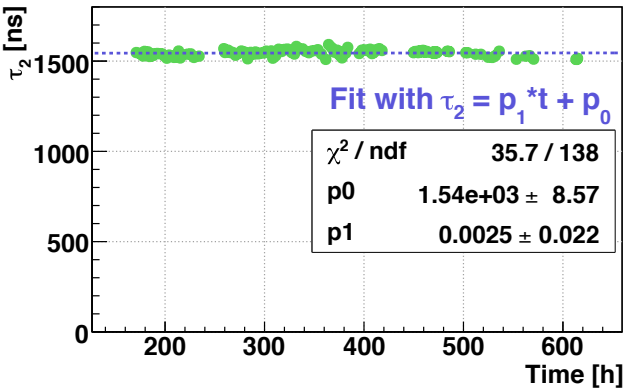

Figure 8.4: Temporal evolution of τ_2. No deterioration of the purity was measure in 600 hrs (25 days) of operation without recirculation through the purification cartridge.

during the LAr tests had a trigger threshold of about 10 pe detected on at least 2 PMTs (V_{th} = 50 mV, Majority 2).

For this analysis the decay time of the slow component was determined for the *virtual channel*. Two general cuts on the events were applied to remove events which contain saturation of the ADCs (PH > 0.89 V for each PMT independently) and those whose peak time was reconstructed outside of determined time interval (PT < 950 ns and PT > 1150 ns on the *virtual channel*).

The average pulses of the selected events were calculated and fitted with Eq. 4.5 (three-exponential decay model). The temporal evolution of τ_2 over 600 hrs of operation is shown in Fig. 8.4 and does not present any sign of purity deterioration. This fact proves that very good purity can be achieved for large volumes. The best value obtained by fitting the data point with a simple line give a $\tau_2 = p_0 = 1540 \pm 9$ ns while the slope parameter p_1 is compatible with 0.

8.4 Gain curve and stability

The gain curve of the PMTs was measured to determine the optimal working point of the modules in LAr. The calibration constants were measured at different voltages using the LED method (Section 4.2.2). The ETL PMT was unstable in LAr and was not used.

The data-points, shown in Fig. 8.5, were fitted (as before) with Eq. 7.1. The gains of the PMTs were adjusted to $2.5 \cdot 10^7$ (calibration constant = 0.2 nVs/p.e.) by changing the supply voltages and the drifts of the gain have been monitored for the duration of the tests (20 days). The temporal evolution (drift) of the calibration constants of the PMTs is shown in Fig. 8.5. The gain drift of the PMTs is lower than 20% in 20 days of measurement with constant thermodynamic conditions.

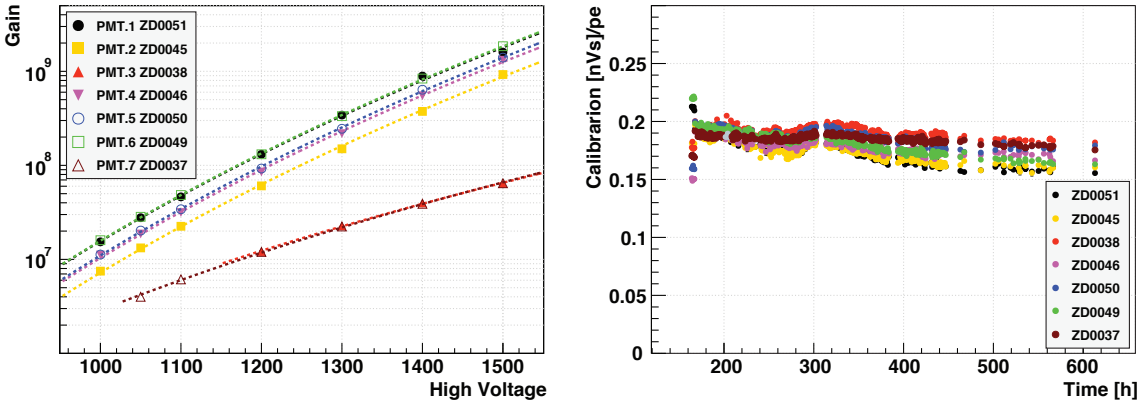

Figure 8.5: Left: Calibration curve of the PMTs in LAr ($T = 300$ K) in the ArDM detector. The lines represent the fit of the data point with Eq. 7.1. **Right:** Temporal evolution of the calibration constant of the PMTs for the duration of the tests.

8.5 Detector response to 511 keV $\gamma-$rays

The detector response to pure 511 keV $\gamma-$rays was measured using the trigger configuration **b** (described in Section 8.1). The DAQ was triggered requiring a deposited energy of 1.78 MeV in the NaI crystal to reduce the contamination from the 1.275 MeV $\gamma-$rays from ^{22}Na. The ^{22}Na source and the crystal were moved in 4 different positions (B, D, F and G in Fig. 8.1); 100k events were acquired per each position.

Data analysis was performed on the *virtual channel* combining all the PMT signals. Events with ADC saturation (PH> 0.89 V for each PMT independently) were rejected and the peak of the signal was required to be around in the trigger acceptance region 920 ns < PT < 1040 ns. The trigger configuration was very simple no other cuts were performed in the analysis.

Firstly the IPH was calculated with the integration algorithm defined in Eq. 4.6. The combination of the signal of different PMTs and the long integration time ($3 \cdot \tau_2 \simeq 4.7$ μs) introduce a spread $\sigma = 25$ p.e. in the IPH distribution, which is not sufficient to obtain a suitable resolution for low energy events. The spread of the integration algorithm was measured analyzing a dataset with a random trigger.

To reduce the integration error only the fast component of the light was taken in account and the total light was calculated by inverting the relation defined in Eq. 4.10:

$$p_{\text{fast}} = \frac{L_{\text{fast}}}{L_{tot}} \qquad \rightarrow \qquad L_{tot} = \frac{L_{\text{fast}}}{p_{\text{fast}}}, \tag{8.1}$$

where $p_{\text{fast}} = 0.212$ (measured in Section 8.2) while L_{fast} was calculated by integrating the signal 50 ns after the peak as described in Eq. 5.6. In this case the integration error is about 6 p.e. The light distribution for the 4 position are shown in Fig. 8.6 (magenta).

A MC simulation (see Section 8.1.3) was performed for those configuration. The digitization of the MC data was approximated by calculating the convolution of the light

distribution $f_{MC}(L)$ with a gaussian $g(L,\sigma)$ function normalized to 1. The time structure of the scintillation light was not considered as the interaction of 511 keV $\gamma-$rays does not involve the presence of nuclear recoils.

The coating of the PMTs (which has an effect of 10% on the total light yield) was assumed to be evaporated TPB for all the PMTs in the MC simulation. For this reason a parameter ε_r was introduced to scale the absolute value of the light of the MC. The light distribution of the digitized MC data is then described with the function $F_{MC}(L)$:

$$F_{MC}(L) = N \cdot f_{MC}(\varepsilon_t \cdot L) \otimes g(L,\sigma) = N \int_{-\infty}^{+\infty} f(\varepsilon_t L) \cdot \frac{1}{\sqrt{2\pi}\sigma} e^{-(L-x)^2/2\sigma^2} \mathrm{d}x, \qquad (8.2)$$

where σ represents the error of the integration evaluation, N is a normalization constant and ε_t is the scaling factor for the light simulated by the MC. For the reduced integration time $\sigma = 6$ ns. The IPH of the measured data was fitted with Eq. 8.2 leaving the parameters N and ε_t free and the result of the fit is shown in Fig. 8.6 (green line).

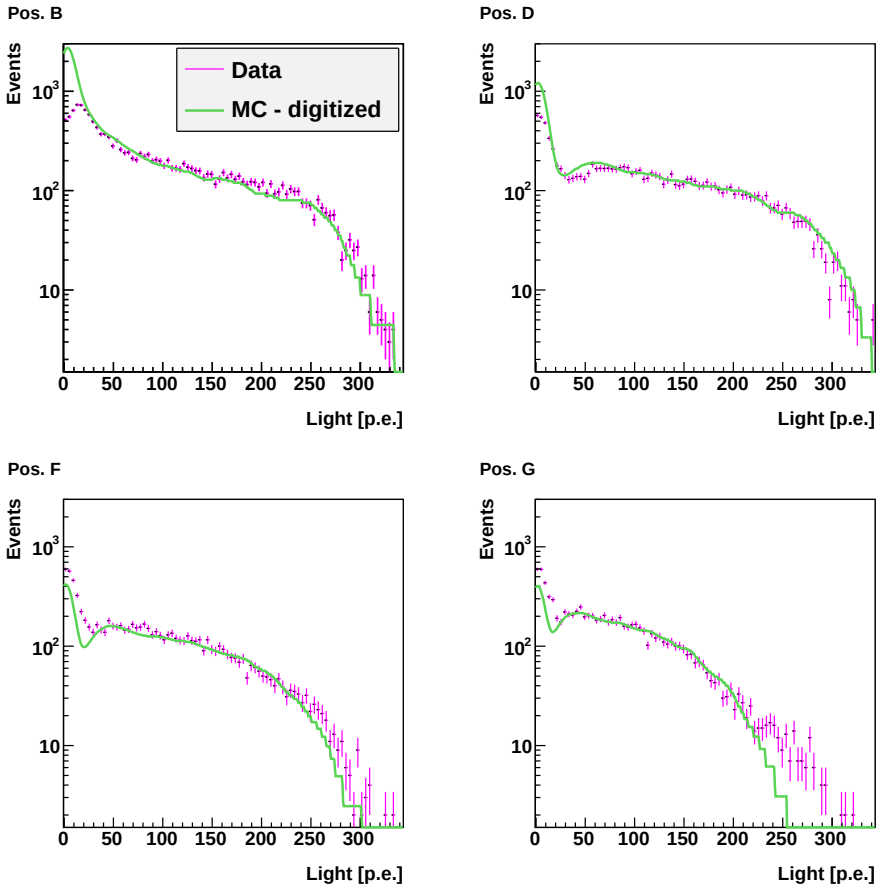

Figure 8.6: Detector response to 511 keV $\gamma-$rays for four different source positions (B, D, G and D). The MC simulation (green) is tuned on the data points (violet).

The MC light prediction (green line) agrees with the measured data. The cuts and the selection performed in the analysis and the partial coverage PMT coverage determine the disagreement < 20 p.e. The mismatch of the tail of the light distribution for position G for $L > 200$ p.e. for position G is caused by the pile-up of cosmic rays and natural background. The scaling parameters are similar and the average value is $\varepsilon_{tune} = 1.12 \pm 0.05$ for all the configurations.

8.5.1 Evaluation of the light yield from the tuned Monte-Carlo

The energy calibration of the detector can be evaluated from the MC by measuring the ratio between energy deposited in the active volume and detected light. The position distributions of the first interaction vertex of 511 keV $\gamma-$rays in the detector projection (zx-plane) are shown in Fig. 8.7. When the source is in pos.B or D, a good fraction of

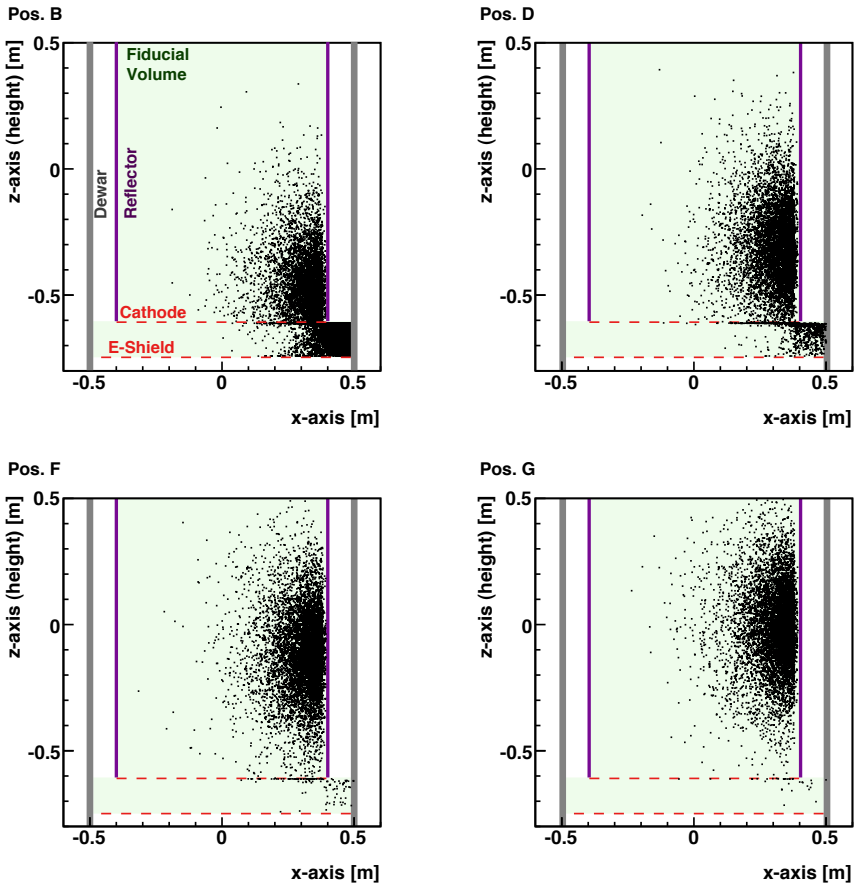

Figure 8.7: Projection of the position of the first interaction vertex in the detector on the xz-plane for different ^{22}Na source positions.

the events ($\approx$ 20%) has the vertex localized below the cathode. The scintillation light (UV) of those events is not efficiently converted and reflected by the WLS-coated side reflectors.

Those events are responsible of the peak at small light yield ($<$ 5 p.e) measured in the test in positions B and D. In the case of the ArDM experiment those events will be suppressed by adding a non coated reflector around the PMT support to shield this region and will be rejected by performing a selection cut on the fiducial volume of the detector.

The distribution of the collected light was plotted as a function of the energy deposited in the fiducial volume (E_{FV}) of the detector as is shown in Fig. 8.8. The events with a vertex below the cathode were rejected and the distributions were sliced on the x-axis. The average values (red crosses) were fitted with linear functions (blue lines); the slope

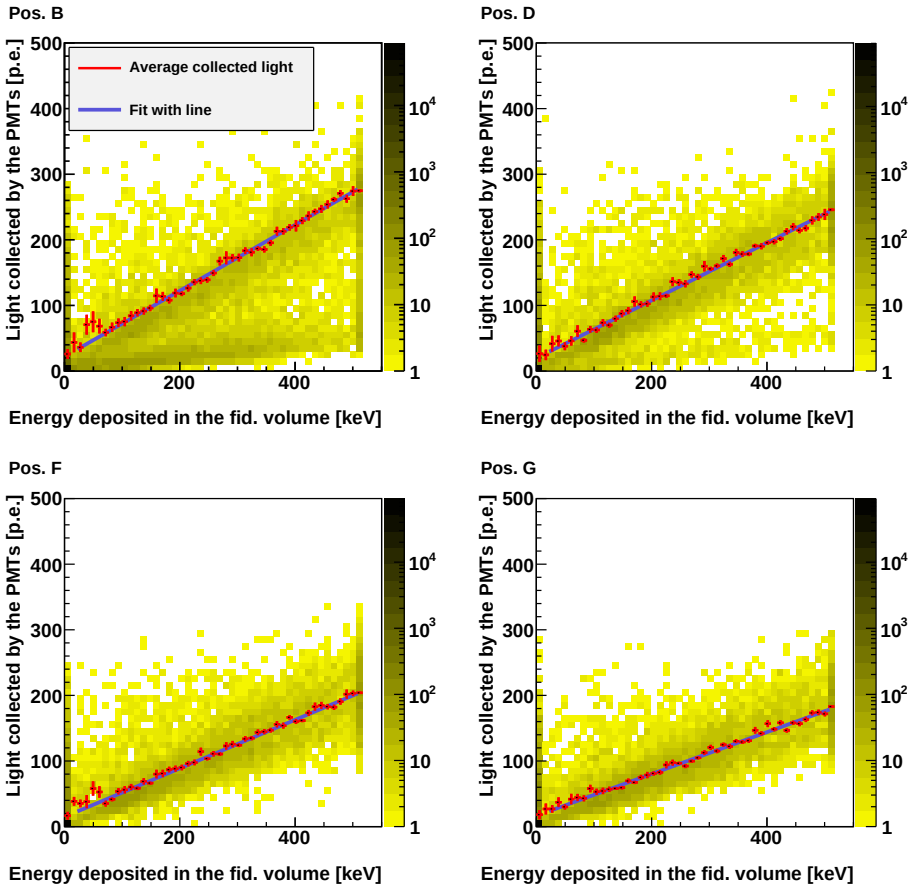

Figure 8.8: Distribution of the collected light as a function of the energy deposited in the fiducial volume of the detector from the MC tuned on the analyzed data in the case of partial light readout coverage (7 PMTs). The average values of the sliced x-axis (red crosses) were fitted with a linear function (blue line) with the slope representing the average light yield for a determined position.

of the curve represent the average light yield for each position. The same procedure was applied to evaluate the light yield for the full light readout case (14 PMTs). The result of the fits is shown in Tab. 8.2. The best value for the light yield with this partial detector is LY= 0.50 ± 0.05 p.e./keVee.

Position	distance from the cathode [cm]	Light Yield (partial - 7 PMTs) [p.e./keVee]	(full - 14 PMTs) [p.e./keVee]
B	10	0.50± 0.05	0.76± 0.05
D	30	0.44± 0.05	0.70± 0.06
F	50	0.37± 0.05	0.62± 0.06
G	60	0.32± 0.05	0.56± 0.05

Table 8.2: Average light yield for each position estimated from the tuned MC for the partial and full detector.

8.6 Detector response to ^{137}Cs and ^{22}Na sources

The detector response to ^{137}Cs and ^{22}Na sources was measured using by triggering directly on the detector (trigger configuration **a**). The trigger conditions were the same for all those data sets, the discriminator thresholds were $V_{\rm th} = 50$ mV for the PMTs and the trigger was generated if at least 2 PMTs were above threshold (Majority $M = 2$).

The effects of the trigger threshold V_{th} on the IPH distribution can be predicted using the information slope s of the prompt light distribution as function of the PH (see Section 5.3.5). The trigger thresholds expressed in p.e. is:

$$L_{\rm th} = \frac{s \cdot M \cdot V_{\rm th}}{p_{\rm fast}} \tag{8.3}$$

where M is the PMT multiplicity required by the trigger and $p_{\rm fast}$ is the prompt fraction of the scintillation light in LAr (measured in Section 8.2). For the datasets used in the following measurements $s = 0.135 \pm 0.005$ p.e./mV while $p_{\rm fast}$ in LAr depends on the interaction type there will be different light threshold for different projectiles as shown in Section 5.4. For the used trigger settings and $e/\gamma-$like interactions $L_{\rm th} \simeq 65$ p.e. The trigger rates were measured with a VME scaler.

Cuts were applied to remove events which contain saturation of the ADCs and those whose peak time was reconstructed outside of the trigger time interval as done in Section 8.3. The DAQ was self-triggered therefore, the acquired data samples include a non negligible fraction of background events. Nuclear recoils and $\alpha-$particle background events can be rejected cutting on the *Component Ratio* (CR) while the electron, γ and μ background can only be subtracted on a statistical base.

The detector background was measured with the same trigger condition used for the data and the IPH spectrum was calculated using the same cuts used for the data analysis.

The different trigger rate information was used for the ^{137}Cs and ^{22}Na data to calculate the fraction of background events (k_{Bkg} or background contamination) defined as:

$$k_{Bkg} = \frac{r_{Bkg}}{r_{Total}} \tag{8.4}$$

where r_{Bkg} is the backround rate (no external source) and r_{Total} is the total trigger rate (source + background). This number represents the fraction of background events in the data sample.

8.6.1 Comparison of the response to ^{137}Cs and ^{22}Na sources

The distributions of the scintillation light measured with the ^{137}Cs and ^{22}Na sources have different background contaminations and cannot be compared directly and must be scaled on with a factor $1/k_{Bkg}$. The different configuration, the total trigger rate, the number of acquired events and the background contamination are listed in Tab. 8.3. The detector response to ^{137}Cs and ^{22}Na sources and background, scaled on $1/k_{Bkg}$, are shown in Fig. 8.9a. The agreement in the high energy tail of the distribution after the scaling process is very good. For this reason the background could be subtracted from the two distributions, revealing the real shape of the detector response to the 2 sources as shown in Fig. 8.9b.

The strong low energy bias of the trigger settings is visible below 100 p.e.. The rightmost shoulder of the ^{22}Na spectrum (shown inFig. 8.9b) is shifted to about 700 p.e. with respect to spectrum shown in Fig. 8.6 (pos D). This indicates the presence of the 1.275 MeV $\gamma-$rays and agrees with the estimated light yields. The smearing effect of the integration algorithm does not allow to investigate the presence of the full absorption peaks and the lack of MC data does not allow to extract possible information for the light yield evaluation. Possible solutions to reduce the influence of this effect are under investigation.

8.6.2 Detector response to different ^{137}Cs source positions

A similar approach was used in the analysis of the data taken with different ^{137}Cs source positions. The unscaled background distribution and 4 distributions relative to different positions (B, D, F and H) scaled on $1/k_{Bkg}$ are shown in Fig. 8.10 (a). Also in this case the agreement of the different measurement in the tail of the distributions is good and the background was removed from the distribution as shown in Fig. 8.10b.

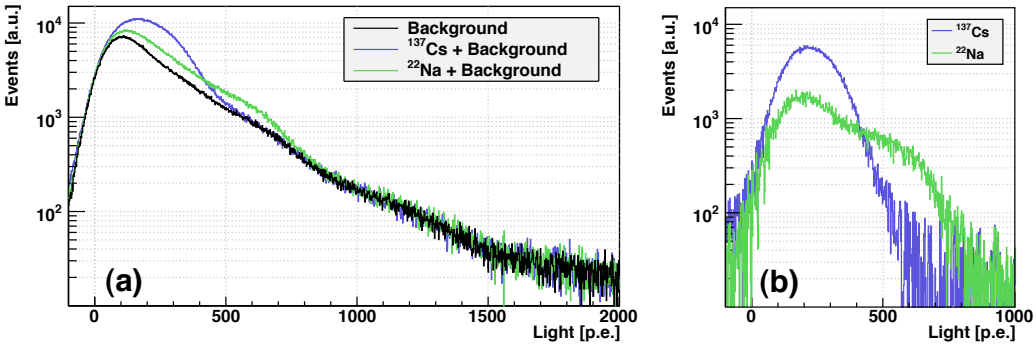

Figure 8.9: a) Detector response to ^{137}Cs (blue) and ^{22}Na (green) sources and background (black) scaled on $1/r_{Bkg}$. **b)** Detector response to ^{137}Cs (blue) and ^{22}Na (green) sources after background subtraction.

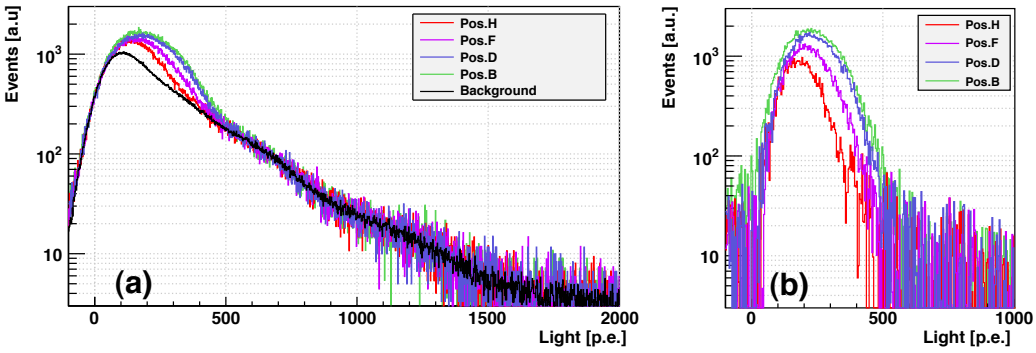

Figure 8.10: a) Detector responses to ^{137}Cs source in different positions scaled on $1/r_{Bkg}$. **b)** Detector response to ^{137}Cs source in different positions after background subtraction.

Source type	Position	Total Rate [kHz]	Events	k_{Bkg} Bkg. contam.
only background	–	4.35	1.5 M	1
^{22}Na	D	5.40	1.5 M	0.649
^{137}Cs	D	6.70	1.5 M	0.806
only background	–	4.48	200 k	1
^{137}Cs	B	7.65	200 k	0.586
^{137}Cs	D	7.30	200 k	0.614
^{137}Cs	F	6.40	200 k	0.7
^{137}Cs	H	5.70	200 k	0.786

Table 8.3: Different configuration, total trigger rate, number of acquired events and the background contamination

Conclusions

The light readout was tested in the ArDM detector with 1 ton of LAr. All Hamamatsu PMTs were working and could be set to a gain of $2.5 \cdot 10^7$ which was defined as the best running condition. The stability of the gain of the PMTs was also measured. The purity of the LAr was constant for the whole duration of the test ($\tau_2 = 1.54 \pm 0.01$ μs) without recirculating the LAr through the purification cartridge.

The light response to the $\gamma-$rays from the ^{22}Na sources was measured at different positions in the detector and the data were compared and fitted with the MC simulation leaving a scaling factor ε_t and a normalization constant as free parameters. The fitted scaling parameters are compatible and the average value is $\varepsilon_{tune} = 1.12 \pm 0.05$ for all configurations. The data agrees with the MC predictions for $L > 20$ p.e. while the disagreement at low energy, which correspond to about 50 keV$_{\mathrm{ee}}$, is determined by different factors.

Firstly the data were taken with partial PMT coverage while the MC simulation included all the PMTs. Moreover the MC did not include the different WLS coating layer which were used in the detector. In addition the reflectance description of the WLS-coated reflectors in the MC was not optimized. The mismatch of the tail of the light distribution for position G for $L > 200$ p.e. for position G is caused by pile-up of cosmic rays and natural background.

In the absence of photo-peaks the light yield was extracted from the measured Compton distributions compared to the MC. The light yield was obtained by fitting the slope of the light distribution as a function of deposited energy in the detector. The results for 7 PMTs and the extrapolation to the full light detector case (14 PMTs) are shown in Tab. 8.2.

Conclusions

The work of this thesis was focussed on research and developments needed to detect the 128 nm VUV light with high efficiency.

The scintillation light of 5.3 MeV $\alpha-$particles was used to study the effect of the impurities on the slow decaying scintillation component of GAr. The quenching of the triplet excimer state was attributed to the presence of water vapors. The longest measured decay time constant for the triplet state was $\tau_2 = (3207 \pm 14)$ ns. The relative intensities of the scintillation components were measured. The two exponential decays model agrees with the data except in the time distribution region between 50 - 150 ns. The slight excess of data was interpreted as an additional radiative process. For this reason a model with three exponential decays was also considered. For two components $p_{\text{fast}} = 84.1\%$ and $p_{\text{slow}} = 15.9\%$, while for three components $p_{\text{fast}} = 83\%$ the rest being divided between the fast and the intermediate components ($p_{\text{slow}} = 14.3\%$ and $p_{\text{int}} = 2.7\%$ respectively).

The properties of several reflector material candidates coated with different WLS methods were studied. The evaporation technique gave in GAr the best result in terms of light yield, reflector production and reliability. The WLS coating thickness was optimized with a dedicated setup. A saturation of the VUV conversion efficiency was measured with TPB evaporated on 3M ESR Vikuiti foils with surface densities above 1 mg/cm^2. In the case of a Tetratex membrane the VUV conversion efficiency saturation was reached already at 0.1 - 0.2 mg/cm^2.

A 1ℓ LAr detector was built (Cell'07) and calibrated with $\alpha-$particles from a ^{210}Pb source ($LY^{\alpha}_{\text{Cell}'07} = 3.10 \pm 0.08$ (stat) $\pm$ 0.66 (sys) p.e./keVee). Tetratex reflectors with different TPB surface thicknesses were tested. No dependence of the light yield on the TPB surface density was found in LAr in the range between 0.25 and 1.1 mg/cm^2.

The relative intensities of the scintillation components were measured for $\alpha-$particles, electron and muons. Two exponential decays are not sufficient to describe the scintillation light of LAr, therefore three exponential decays are used. For $\alpha-$particles 72% of the scintillation light is produced in the decay of the singlet state and 21% in the triplet state decay. The remaining 7% of the light is distributed in the intermediate region. For 1 MeV electrons and cosmic muons (minimum ionizing particles) the relative intensities of the singlet, triplet and intermediate components are 24%, 73% and 3%, respectively.

New high gain PMTs were installed in the detector (Cell'08) and argon nuclear recoils induced by neutron from an AmBe source were measured. The rejection capability for recoiling energy lower than 100 p.e. ($\sim$30 keVee) can be improved by including an integration algorithm with a smaller integration error or an event-by-event fit as proposed in Section 5.3.3.

The 1 ton ArDM light readout was commissioned. The DAQ, the WLS side reflector and the preliminary light detector (8 out of 14 PMTs) were built and tested in gaseous and liquid argon. The light yield as a function of the source position was measured in GAr at $T =$ 300 K and 88 K. The behavior of the light as a function of position could be explained by Monte-Carlo simulation but the absolute value of the detected light could not be reproduced correctly. The results show that evaporated TPB and TPB:Paraloid dissolved in chloroform are good coating candidates, as the difference between their light yields is small. The light yield did not show aging effects even when the WLS coated reflectors and PMTs were (accidentally) violently flushed with GAr (and LAr).

In the ArDM detector the purity of GAr deteriorated rapidly at $T = 300$ K while remaining stable at 88 K for days. During the second cool-down a constant value of $\tau_2 = 4.8 \pm 0.1$ μs was measured for $T = 88$ K and $P_{GAr} = 0.9$ bar. This light value might be caused by the appearance of recombination effects which are negligible in GAr and becomes more important for higher GAr densities [99].

The light readout was tested in the ArDM detector with 1 ton of LAr. All Hamamatsu PMTs were working and could be set to a gain of $2.5 \cdot 10^7$ which was defined as the best running condition. The voltage divider of the ETL PMT had reliability problem even in LAr. The impurities contamination level of LAr was studied through the analysis of the decay time of the slow component τ_2 which was constantly monitored for the whole duration of the test. The temporal evolution of τ_2 does not show any deterioration of the purity of LAr and the results are compatible with a constant value $\tau_2 = 1.54 \pm 0.01$ μs, obtained without recirculating the LAr thought the purification cartridge. This result is very important as it demonstrate the possibility of reaching a low impurity contamination level in a large volume.

The light responses to the $\gamma-$rays from the ^{22}Na and ^{137}Cs sources were measured at different positions in the detector. The measured light spectra agrees with Monte-Carlo simulation in the case of the ^{22}Na source. A light yield of 0.50 ± 0.05 p.e./keVee was achieved with the source in the lowest position and for 7 PMTs. The final light detector, made of 14 low background Hamamatsu R5912-02 mod PMTs, was installed in the ArDM detector in October 2009.

Bibliography

[1] D. Clowe *et al.* A direct empirical proof of the existence of dark matter. *Astrophysical Journal*, (648), 2006. arXiv:astro-ph/0608407v1, doi:10.1086/508162.

[2] B. Fuchs. NGC2613, 3198, 6503, 7184: Case studies against 'maximum' disks. 1998. arXiv:astro-ph/9812048v1.

[3] J. Bekenstein and M. Milgrom. Does the missing mass problem signal the breakdown of Newtonian gravity? *Astrophysical Journal*, 286:7–14, 1984. doi:10.1086/162570.

[4] C. Amsler *et al.* (Particle Data Group). Review of particle physics. *Physics Letters B*, 667, 2008. doi:10.1016/j.physletb.2008.07.018.

[5] Ki-Young Choi and Leszek Roszkowski. E-wimps. 2005. arXiv:hep-ph/0511003.

[6] Gianfranco Bertone, Dan Hooper, and Joseph Silk. Particle dark matter: evidence, candidates and constraints. *Physics Reports*, 405(5-6):279 – 390, 2005. doi:10.1016/j.physrep.2004.08.031.

[7] W. de Boer *et al.* EGRET excess of diffuse galactic gamma rays as tracer of dark matter. *Astron. Astrophys.*, 444:51, 2005. arXiv:astro-ph/0508617, doi:10.1051/0004-6361:20053726.

[8] [online]Available from: http://fermi.gsfc.nasa.gov/.

[9] MAGIC Collaboration: E. Aliu *et al.* Upper limits on the VHE gamma-ray emission from the Willman 1 satellite galaxy with the MAGIC telescope. *Astrophysical Journal*, 697:1299, 2009. doi:10.1088/0004-637X/697/2/1299.

[10] F. Aharonian *et al.* HESS observations of the galactic center region and their possible dark matter interpretation. *Phys. Rev. Lett.*, 97(22):221102, Nov 2006. doi:10.1103/PhysRevLett.97.221102.

[11] M. Boezio *et al.* PAMELA and indirect dark matter searches. *New J. Phys.*, 11:105023, 2009. doi:10.1088/1367-2630/11/10/105023.

[12] J.D. Zornoza *et al.* (ANTARES Collaboration). Dark matter search with the ANTARES neutrino telescope. *Nucl. Phys. Proc. Suppl.*, B173:79 – 82, 2007. doi:10.1016/j.nuclphysbps.2007.08.146.

[13] Francis Halzen. astroparticle physics with high energy neutrinos: from AMANDA to IceCube. *European Physical Journal C*, 46:669, 2006. doi:10.1140/epjc/s2006-02536-4.

[14] A. A. Abdo *et al.* Measurement of the cosmic ray $e^+ + e^-$ spectrum from 20 GeV to 1 TeV with the Fermi large area telescope. *Phys. Rev. Lett.*, 102:181101, 2009. arXiv:0905.0025, doi:10.1103/PhysRevLett.102.181101.

[15] O. Adriani *et al.* An anomalous positron abundance in cosmic rays with energies 1.5-100 GeV. *Nature*, 458:607–609, 2009. arXiv:0810.4995, doi:10.1038/nature07942.

[16] J. D. Lewin and P. F. Smith. Review of mathematics, numerical factors, and corrections for dark matter experiments based on elastic nuclear recoil. *Astroparticle Physics*, 6(1):87 – 112, 1996. doi:10.1016/S0927-6505(96)00047-3.

[17] G.J. Alner *et al.* The DRIFT-II dark matter detector: Design and commissioning. *Nucl. Instrum. Meth.*, A555(1-2):173 – 183, 2005. doi:10.1016/j.nima.2005.09.011.

[18] Z. Ahmed *et al.* Results from the final exposure of the CDMS-II experiment. 2009. arXiv:0912.3592.

[19] E. Armengaud *et al.* First results of the EDELWEISS-II WIMP search using Ge cryogenic detectors with interleaved electrodes. 2009. arXiv:0912.0805v1.

[20] P. Gorla *et al.* Cuoricino and CUORE detectors: Developing big arrays of large mass bolometers for rare events physics. *Nucl. Phys. Proc. Suppl.*, 150:214–218, 2006. doi:10.1016/j.nuclphysbps.2004.11.387.

[21] G. Angloher *et al.* Commissioning run of the CRESST-II dark matter search. *Astroparticle Physics*, 31(4):270 – 276, 2009. doi:10.1016/j.astropartphys.2009.02.007.

[22] R. Bernabei *et al.* Dark matter particles in the galactic halo: Results and implications from DAMA/NaI. *Int. J. Mod. Phys.*, D13:2127–2160, 2004. arXiv:astro-ph/0501412, doi:10.1142/S0218271804006619.

[23] V. N. Lebedenko *et al.* Result from the first science run of the ZEPLIN-III dark matter search experiment. *Phys. Rev.*, D80:052010, 2009. arXiv:0812.1150, doi:10.1103/PhysRevD.80.052010.

[24] J. Angle *et al.* Limits on spin-dependent WIMP-nucleon cross-sections from the XENON10 experiment. *Phys. Rev. Lett.*, 101:091301, 2008. arXiv:0805.2939, doi:10.1103/PhysRevLett.101.091301.

[25] E. Aprile *et al.* First dark matter results from the XENON 100 experiment. 2010. arXiv:1005.0380.

[26] A. Rubbia. ArDM: A ton-scale liquid argon experiment for direct detection of dark matter in the universe. *J. Phys. Conf. Ser.*, 39:129, 2006. doi:10.1088/1742-6596/39/1/028.

[27] P. Benetti *et al.* First results from a dark matter search with liquid argon at 87 K in the Gran Sasso underground laboratory. *Astroparticle Physics*, 28(6):495 – 507, 2008. doi:10.1016/j.astropartphys.2007.08.002.

[28] A. Hime. DEAP & CLEAN detectors for low energy particle astrophysics. *AIP Conf. Proc.*, 870:205–207, 2006. doi:10.1063/1.2402618.

[29] R. Bernabei *et al.* Possible implications of the channeling effect in NaI(Tl) crystals. *European Physical Journal C*, 53(2), Jan 2008. doi:10.1140/epjc/s10052-007-0479-0.

[30] R. Bernabei *et al.* First results from DAMA/LIBRA and the combined results with DAMA/NaI. *European Physical Journal C*, 55(3), Aug 2008. doi:10.1140/epjc/s10052-008-0662-y.

[31] The CDMS-II Collaboration. Dark matter search results from the CDMS-II experiment. *Science*, 327(5973):1619–1621, 2010. doi:10.1126/science.1186112.

[32] N. Ferrari *et al.* WARP: a double phase argon programme for dark matter detection. *J. Phys. Conf. Ser.*, 39:111–113, 2006. doi:10.1088/1742-6596/39/1/022.

[33] P. Benetti *et al.* The ICARUS R&D program and results. *Nucl. Instrum. Meth.*, A327(1):173 – 177, 1993. doi:10.1016/0168-9002(93)91437-R.

[34] P. Benetti *et al.* Measurement of the specific activity of ^{39}Ar in natural argon. *Nuclear Instruments and Methods in Physics Research Section A: Accelerators, Spectrometers, Detectors and Associated Equipment*, 574(1):83 – 88, 2007. doi:10.1016/j.nima.2007.01.106.

[35] M. J. Carvalho and G. Klein. Luminescence decay in condensed argon under high energy excitation. *Journal of Luminescence*, 18-19(Part 1):487 – 490, 1979. doi:10.1016/0022-2313(79)90167-4.

[36] Masayo Suzuki. Recombination luminescence from ionization tracks produced by alpha particles in high pressure argon, krypton and xenon gases. *Nuclear Instruments and Methods in Physics Research*, 215(1-2):345 – 356, 1983. doi:10.1016/0167-5087(83)91327-3.

[37] Robert S. Mulliken. Potential curves of diatomic rare-gas molecules and their ions, with particular reference to Xe_2^*. *The Journal of Chemical Physics*, 52(10):5170–5180, 1970. doi:10.1063/1.1672756.

[38] Marlo Martin. Exciton self-trapping in rare-gas crystals. *The Journal of Chemical Physics*, 54(8):3289–3299, 1971. doi:10.1063/1.1675342.

[39] A. Gedanken, J. Jortner, B. Raz, and A. Szöke. Electronic energy transfer phenomena in rare gases. *J. Chem. Phys.*, 57(8):3456–3469, 1972. doi:10.1063/1.1678779.

[40] G. S. Hurst, T. E. Stewart, and J. E. Parks. vacuum ultraviolet radiation and Jesse effects in the noble gases. *Phys. Rev.*, A2(5):1717–1720, Nov 1970. doi:10.1103/PhysRevA.2.1717.

[41] H. Langhoff. The origin of the third continua emitted by excited rare gases. *Optics Communications*, 68:31–34, September 1988. doi:10.1016/0030-4018(88)90008-9.

[42] W. Krötz *et al.* Third excimer continuum of argon excited by a heavy-ion beam. *Phys. Rev.*, A43(11):6089, 1991. doi:10.1103/PhysRevA.43.6089.

[43] C. Amsler *et al.* Luminescence quenching of the triplet excimer state by air traces in gaseous argon. *JINST*, 3:P02001, 2008. doi:10.1088/1748-0221/3/02/P02001.

[44] A. Hitachi *et al.* Effect of ionization density on the time dependence of luminescence from liquid argon and xenon. *Phys. Rev.*, B27(9):5279–5285, May 1983. doi:10.1103/PhysRevB.27.5279.

[45] J. W. Keto *et al.* Production mechanisms and radiative lifetimes of argon and xenon molecules emitting in the ultraviolet. *Phys. Rev. Lett.*, 33(23):1365, 1974. doi:10.1103/PhysRevLett.33.1365.

[46] P. Millet *et al.* Spectroscopic and kinetic analysis of the VUV emissions of argon and argon-xenon mixtures: I. Study of pure argon. *J. Phys. B: At. Mol. Phys.*, 15:2935–2944, 1982. doi:10.1088/0022-3700/15/17/024.

[47] T. Oka, K. V. S. Rama Rao, J. L. Redpath, and R. F. Firestone. Mechanism for decay and spontaneous radiative decay constants of the lowest-lying attractive excited states of Ne_2, Ar_2, and Kr_2. *The Journal of Chemical Physics*, 61(11):4740–4746, 1974. doi:10.1063/1.1681797.

[48] R. Acciarri *et al.* Effects of nitrogen and oxygen contaminations in liquid argon. *Nucl. Instrum. Meth.*, A607(1):169 – 172, 2009. Radiation Imaging Detectors 2008 - Proceedings of the 10th International Workshop on Radiation Imaging Detectors. doi:10.1016/j.nima.2009.03.142.

[49] M. Miyajima et al. Average energy expended per ion pair in liquid argon. *Phys. Rev.*, A9:1438–1443, 1974. doi:10.1103/PhysRevA.9.1438.

[50] R.L. Platzman. Total ionization in gases by high-energy particles: An appraisal of our understanding. *The International Journal of Applied Radiation and Isotopes*, 10(2-3):116 – 127, 1961. doi:10.1016/0020-708X(61)90108-9.

[51] K. Masuda, E. Shibamura, T. Doke, A. Hitachi, and J. Kikuchi. Relation between scintillation and ionization produced by relativistic heavy ions in liquid argon. *Phys. Rev.*, A39:4732–4734, 1989. doi:10.1103/PhysRevA.39.4732.

[52] E. Shibamura *et al.* Ionization and scintillation produced by relativistic Au, He and H ions in liquid argon. *Nuclear Instruments and Methods in Physics Research Section A: Accelerators, Spectrometers, Detectors and Associated Equipment*, 260(2-3):437 – 442, 1987. doi:10.1016/0168-9002(87)90113-6.

[53] A. Hitachi, T. Takahashi, T. Hamada, E. Shibamura, A. Nakamoto, N. Funayama, K. Masuda, and T. Doke. Scintillation response of liquid argon to fission fragments. *Phys. Rev.*, B23(9):4779–4781, May 1981. doi:10.1103/PhysRevB.23.4779.

[54] A. Hitachi, T. Takahashi, T. Hamada, E. Shibamura, N. Funayama, K. Masuda, J. Kikuchi, and T. Doke. LET dependence of the luminescence yield from liquid argon and xenon. *Nuclear Instruments and Methods in Physics Research*, 196(1):97 – 100, 1982. doi:10.1016/0029-554X(82)90622-X.

[55] E. Aprile, K. L. Giboni, P. Majewski, K. Ni, M. Yamashita, R. Hasty, A. Manzur, and D. N. McKinsey. Scintillation response of liquid xenon to low energy nuclear recoils. *Phys. Rev.*, D72(7):072006, Oct 2005. doi:10.1103/PhysRevD.72.072006.

[56] A. Hitachi and T. Doke. Luminescence quenching in liquid argon under charged-particle impact: Relative scintillation yield at different linear energy transfer. *Phys. Rev.*, B46(18), 1992. doi:10.1103/PhysRevB.46.11463.

[57] D.C. Lorents. The physics of electron beam excited rare gases at high densities. *Physica B+C*, 82(1):19 – 26, 1976. Proceedings of the Twelfth International Conference on Phenomena in Ionized Gases. doi:10.1016/0378-4363(76)90265-5.

[58] J.W. Keto, R.E. Gleason Jr., T.D. Bonifield, G.K. Walters, and F.K. Soley. Collisional mixing of the lowest bound molecular states in xenon and argon. *Chemical Physics Letters*, 42(1):125 – 128, 1976. doi:10.1016/0009-2614(76)80566-0.

[59] J. Lindhard. Integral equations governing radiation effects. *Mat. Fys. Medd. Dan. Vid. Selsk.*, 33(10), 1963. Available from: http://www.sdu.dk/media/bibpdf/Bind%2030-39%5CBind%5Cmfm-33-10.pdf.

[60] J. Lindhard *et al.* Range concepts and heavy ions ranges. *Mat. Fys. Medd. Dan. Vid. Selsk.*, 33(14), 1963. Available from: http://www.sdu.dk/media/bibpdf/Bind%2030-39%5CBind%5Cmfm-33-14.pdf.

[61] J. Lindhard *et al.* Approximation method in classical scattering by screened coulomb fields. *Mat. Fys. Medd. Dan. Vid. Selsk.*, 36(10), 1968.

[62] J. B. Birks and F. A. Black. Deterioration of Anthracene under $\alpha-$particle irradiation. *Proceedings of the Physical Society. Section A*, 64(5):511–512, 1951. doi:10.1088/0370-1298/64/5/112.

[63] S. Kubota, A. Nakamoto, T. Takahashi, S. Konno, T. Hamada, M. Miyajima, A. Hitachi, E. Shibamura, and T. Doke. Evidence of the existence of exciton states in liquid argon and exciton-enhanced ionization from xenon doping. *Phys. Rev. B*, 13(4):1649–1653, Feb 1976. doi:10.1103/PhysRevB.13.1649.

[64] D.-M. Mei, Z.-B. Yin, L.C. Stonehill, and A. Hime. A model of nuclear recoil scintillation efficiency in noble liquids. *Astroparticle Physics*, 30(1):12 – 17, 2008. doi:10.1016/j.astropartphys.2008.06.001.

[65] D. Gastler, E. Kearns, A. Hime, L. C. Stonehill, S. Seibert, J. Klein, W. H. Lippincott, D. N. McKinsey, and J. A. Nikkel. Measurement of scintillation efficiency for nuclear recoils in liquid argon. April 2010. arXiv:1004.0373.

[66] M.J. Berger, J.S. Coursey, M.A. Zucker, and J. Chang. Stopping-power and range tables for electrons, protons, and helium ions [online]. Available from: http://physics.nist.gov/PhysRefData/Star/Text/contents.html.

[67] T. Doke, Akira Hitachi, Jun Kikuchi, Kimiaki Masuda, and E. Shibamura. Scintillation yields by relativistic heavy ions and the relation between ionization and scintillation in liquid argon. *Nucl. Instrum. Meth.*, A235:136–141, 1985. doi:10.1016/0168-9002(85)90254-2.

[68] T. D. Strickler and E. T. Arakawa. Optical emission from argon excited by alpha particles: Quenching studies. *J. Chem. Phys.*, 41:1783, 1964. doi:10.1063/1.1726158.

[69] R. *et al.* Acciarri. Effects of nitrogen contamination in liquid argon. 2008. arXiv:0804.1217.

[70] R. Acciarri et al. Oxygen contamination in liquid Argon: combined effects on ionization electron charge and scintillation light. 2008. arXiv:0804.1222.

[71] W. H. Lippincott *et al.* Scintillation time dependence and pulse shape discrimination in liquid argon. *Phys. Rev.*, C78(3):035801, Sep 2008. doi:10.1103/PhysRevC.78.035801.

[72] J. D. Cockcroft and E. T. S. Walton. *Proc. Roy. Soc.*, A137(229):229, 1932.

[73] P. Jeanneret, J. Busto, J. L. Vuilleumier, A. Geiser, V. Zacek, H. Keppner, and R. de Oliveira. Performance of a new micromegas detector, with woven wire mesh, in cf4. *Nuclear Instruments and Methods in Physics Research Section A: Accelerators, Spectrometers, Detectors and Associated Equipment*, 500(1-3):133 – 143, 2003. NIMA Vol 500. doi:10.1016/S0168-9002(03)00333-4.

[74] F. Sauli. GEM: A new concept for electron amplification in gas detectors. *Nucl. Instrum. Meth.*, A386:531, 1997. doi:10.1016/S0168-9002(96)01172-2.

[75] V. Peskov *et al.* First attempts to combine capillary tubes with photocathodes. *Nucl. Instrum. Meth.*, A433:492, 1999. doi:10.1016/S0168-9002(99)00346-0.

[76] C. Shalem R. Chechik, A. Breskin and D. Mormann. Thick GEM-like hole multipliers: Properties and possible applications. *Nucl. Instrum. Meth.*, A535:303, 2004.

[77] Polina Otiuogova. *Development of a large electron multiplier (LEM) based charge readout system for the ArDM experiment.* PhD thesis, ETH Zürich, 2008.

[78] Filippo Resnati. *(in preparation).* PhD thesis, ETH Zürich, 2011.

[79] V. Boccone *et al.* Development of wavelength shifter coated reflectors for the ArDM argon dark matter detector. *JINST*, 4:P06001, 2009. doi:10.1088/1748-0221/4/06/P06001.

[80] A. Bueno et al. Characterization of large area photomultipliers and its application to dark matter search with noble liquid detectors. *JINST*, 3:P01006, 2008. arXiv:0711.3592, doi:10.1088/1748-0221/3/01/P01006.

[81] Starna Brand. *Reference Materials for Molecular Fluorescence Spectroscopy.* Available from: http://www.starna.co.uk/ukhome/d_ref/f_ref/flou_p4.html.

[82] H. Cabrera. *Optimierung des Wellenlängenschiebers für das ArDM-Experiment.* Master's thesis, Universität Zürich, 2006.

[83] L. Kaufmann. *Detector performance and background studies for the ArDM experiment.* PhD thesis, ETH Zürich, 2008.

[84] Rico Chandrasekharan. *Design of the light readout for the ArDM experiment.* PhD thesis, ETH Zürich, 2007.

[85] J. S. O'Connell and F. J. Schima. Muon induced radioactivity in underground detectors. *Phys. Rev.*, D38, 1988. doi:10.1103/PhysRevD.38.2277.

[86] H.H. Loosli. *Nachweis von ^{39}Ar in atmosphärischem Argon.* PhD thesis, Universität Bern, 1968.

[87] UK Dark Matter Collaboration,. Available from: http://hepwww.rl.ac.uk/ukdmc/ukdmc.html.

[88] George W. Wetherill. Spontaneous fission yields from uranium and thorium. *Phys. Rev.*, 92(4):907–912, Nov 1953. doi:10.1103/PhysRev.92.907.

[89] A. Büchler. *The beginning of a dark matter adventure*. Bachelor's thesis, Universität Zürich, 2005.

[90] International Atomic Energy Agency. Nuclear data section. Available from: http://www-nds.iaea.org/.

[91] T. Takahashi, S. Himi, M. Suzuki, J. Ruangen, and S. Kubota. Emission spectra from Ar-Xe, Ar-Kr, Ar-N_2, Ar-CH_4, Ar-CO_2 and Xe-N_2 gas scintillation proportional counters. *Nucl. Instrum. Meth.*, 205:591–596, February 1983. doi:10.1016/0167-5087(83)90028-5.

[92] Hamamatsu. *Photomultiplier Handbook*.

[93] A. M. Sànchez, P. R. Montero, and F. V. Tomè. FITBOR: a new program for the analysis of complex alpha spectra. *Nucl. Instrum. Meth.*, pages 593–596, February 1996. doi:10.1016/S0168-9002(96)80058-1.

[94] T. Siiskonen and R. Pöllänen. Simulation of alpha particle spectra from aerosol samples. *Applied Radiation and Isotopes*, 60(6), 2004. doi:10.1016/j.apradiso.2004.02.021.

[95] Andrea Dell'Antone. *Studio di un rivelatore ad argon liquido per la ricerca di materia oscura*. Master's thesis, Università degli studi di Genova, 2009.

[96] Sang-Tae Park. Neutron energy spectra of ^{252}Cf, Am-Be source and of the D(d,n)^{3}he reaction. *Journal of Radioanalytical and Nuclear Chemistry*, 256(1):163–166, 2003.

[97] W. Bonivento, E. Collet, P. Imbert, and C. deLaTaille. Radiation hard micro-coaxial cables for the ATLAS liquid argon calorimeters. *Nuclear Instruments and Methods in Physics Research Section A: Accelerators, Spectrometers, Detectors and Associated Equipment*, 451(2):492 – 505, 2000. doi:10.1016/S0168-9002(00)00324-7.

[98] Marìa del Carmen Carmona Benìtez. *Direct dark matter searches with noble liquid detectors: The ArDM experiment*. PhD thesis, Universidad de Granada, 2009.

[99] Masayo Suzuki, Jian-zhi Ruan(Gen), and Shinzou Kubota. Time dependence of the recombination luminescence from high-pressure argon, krypton and xenon excited by alpha particles. *Nucl. Instrum. Meth.*, 192(2-3):565 – 574, 1982. doi:10.1016/0029-554X(82)90874-6.

[100] S. Agostinelli *et al.* GEANT4 - a simulation toolkit. *Nucl. Instrum. Meth.*, A506(3):250 – 303, 2003. doi:10.1016/S0168-9002(03)01368-8.

Acknowledgments

Well, finally here. Following the Italian tradition (and contrary to UBS) I won't give names[2]. I'll make an exception to express my deep gratitude to Prof. Dr. Claude Amsler for the fantastic opportunity he gave me.

When I started - about 4 years ago - suddenly everything in the lab changed position with deep terror and surprise of the lab-master. Many thanks to him as he always gladly shared with me his deep experience. I would like to thank all the UniZH group (not forgetting the former members) for the support, the discussions, the fights, the beers, the coffee breaks, the suffered ArDM shifts, the sometime eccentric journal club papers and - last but not least - for the correction of my thesis. About this... 1 ton of thanks to those who spent their time reading and correcting my thesis not forgetting the *Zusammenfassung* translator(s). I'm in debt with you all. Then I need to thank the big guy I shared the office with, for the friendship and for the precious skills I acquired about mechanics, cars, motorbikes, french.

Thanks to the ETH colony at CERN for the precious help during the commissioning of the big LAr barrel. Thanks loads also to the Sheffield and Granada colleagues whose work was essential for the construction of the detector.

Special acknowledgment should be given to my family who always unconditionally supported me, even ignoring what Dark Matter is. As many of us know, being far from home is sometimes not easy. Luckily I have wonderful friends who never missed their support in the moments of need. Let me have one more. Thanks infinitely to who demonstrated me that sometimes $1 + 1 = 3$. This is incredibly beautiful.

[2]Italian Proverb: "*Tell the sin but not the sinner*"